Development of metal-complex based catalysts for electro- and photo-chemical CO$_2$ reduction

Lee Sze Koon

Doctor of Philosophy

Department of Structural Molecular Science

School of Physical Sciences

SOKENDAI (The Graduate University for

Advanced Studies)

Development of metal-complex based catalysts

for electro- and photo-chemical CO₂ reduction

電気／光化学的二酸化炭素還元に向けた金属錯体触媒の開発

Lee Sze Koon

SOKENDAI (The Graduate University for Advanced Studies)

School of Physical Sciences

Department of Structural Molecular Science

Contents

General Introduction

1. Background and challenges for CO_2 reduction

Worldwide energy consumption has constantly increased due to the rising population and growth of economy. Uncontrolled combustion of oil, natural gas, and coal has resulted in the rapid depletion of limited fossil fuels resources, and release of greenhouse gas such as CO_2 into the atmosphere which causes global warming.[1-2]

To solve these problems, the development of a catalytic system that can convert CO_2 into renewable fuels and commodity chemicals has raised much attention. Although ideal system is a direct conversion of CO_2 into liquid fuel, the reduction of CO_2 into simple C_1 building blocks such as carbon monoxide (CO) and formic acid (HCOOH) is also economically desirable. CO can be used as a resource to synthesis methanol (CO + $2 H_2 \rightarrow CH_3OH + H_2O$), while HCOOH represents a promising reversible hydrogen carrier and other applications.[3-4]

Generally, one electron reduction of CO_2 to $CO_2^{\bullet-}$ is challenging because it requires high electrochemical potential (Table 1, eq. 1), which is attributed to the large reorganization energy between the linear CO_2 molecule and the bent $CO_2^{\bullet-}$ radical anion. As an alternative, proton-coupled multi-electron CO_2 reduction processes are more favorable as thermodynamically more stable molecules are produced (Table 1, eq. 3–7). Therefore, a single catalyst that can accommodate several redox equivalents is required in order to facilitate multi-electron transfer reaction. In addition, the catalyst should be selective towards CO_2 reduction rather than the competing proton reduction reaction (Table 1, eq. 8).[5-6]

Table 1: Standard redox potentials for CO_2 reduction and H_2 evolution reaction in pH 7 aqueous solution vs. NHE, 25°C, 1 atm gas pressure.

Reactions	E^0 (V)	
$CO_2 + e^- \rightarrow CO_2^{\bullet-} + H_2O$	$E^0 = -1.90$ V	(1)
$2\ CO_2 + 2\ e^- \rightarrow CO + CO_3^{2-}$	$E^0 = -0.64$ V	(2)
$CO_2 + 2\ H^+ + 2\ e^- \rightarrow CO + H_2O$	$E^0 = -0.53$ V	(3)
$CO_2 + 2\ H^+ + 2\ e^- \rightarrow HCOOH$	$E^0 = -0.61$ V	(4)
$CO_2 + 4\ H^+ + 4\ e^- \rightarrow HCHO + H_2O$	$E^0 = -0.48$ V	(5)
$CO_2 + 6\ H^+ + 6\ e^- \rightarrow CH_3OH + H_2O$	$E^0 = -0.38$ V	(6)
$CO_2 + 8\ H^+ + 8\ e^- \rightarrow CH_4 + 2\ H_2O$	$E^0 = -0.24$ V	(7)
$2\ H^+ + 2\ e^- \rightarrow H_2$	$E^0 = -0.41$ V	(8)

2. Nature's example in CO₂ reduction

In nature, plants perform photosynthesis to convert solar energy into chemically accessible energy source. Photosystem II initiates photosynthesis by catalyzing light-driven water oxidation (2 $H_2O \rightarrow O_2$ + 4 H^+ + 4 e^-) at oxygen evolving center (Mn_4Ca cluster).[7] The emerged electrons and protons are converted to bio-reductants such as NADPH and ATP. These bio-reductants are consumed in the Calvin cycle to fix atmospheric CO_2 into carbohydrate, which is the natural carbon-based fuel.

Of particular interest, selective CO_2 reduction into CO is carried out by carbon monoxide dehydrogenase cluster C (CODH), which can be found in some anaerobic bacteria, such as *M. thermoacetica* and *C. hydrogenoformans*. The CODH consists of Ni and Fe active centers bridged by a Fe_3S_4 cluster, forming a distorted cubane-like $NiFe_4S_4$ cluster (Figure 1).[8] In CODH, CO_2 reduction reaction is initiated by the electron transfer from the neighboring ferredoxin moieties, generating the catalytically active low-valent Ni center that bind CO_2. The resulting CO_2 adduct is stabilized by the adjacent protonated histidine and lysine residues, meanwhile, C–O bond cleavage is assisted by the slightly electrophilic Fe^{II} center *via* push–pull mechanism. The low-valent Ni center serves as a Lewis base to donate electrons to CO_2 ("push"), while the Fe^{II} center acts as a Lewis acid to facilitate the electron transfer from Ni to CO_2 ("pull").[9-10] Although CODH is not suitable for industrial application due to its extremely oxygen-sensitive properties, it has provided inspiration for the design of new catalysts for CO_2 reduction.[11]
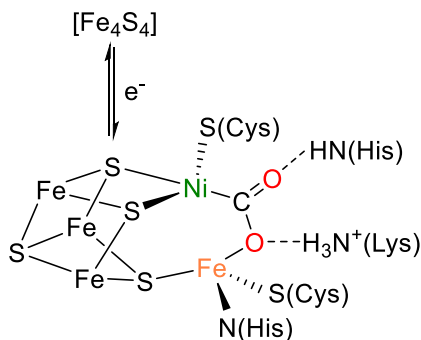

Figure 1: Proposed catalytic active site for CO_2 reduction of CODH.[9-11]

3. Artificial ways in CO$_2$ reduction

The goal of an artificial photosynthesis is to develop a catalytic system that can utilize sunlight to convert CO$_2$ into high-energy chemicals by mimicking the plants and photosynthetic organisms. One of the major challenges in artificial photosynthetic system is to perform all these biomimetic tasks simultaneously (e.g., absorption of light, water oxidation, and CO$_2$ reduction). An alternative strategy is to divide the overall process into its two half reactions, water oxidation and CO$_2$ reduction. This strategy allows detailed mechanistic study and optimization of the catalyst. Once each side is optimized, these half reactions are ready to be combined in a single catalytic system.[12-14]

In my work, I'm focusing in the development of metal complexes as catalysts for CO$_2$ reduction. In order to initiate the CO$_2$ reduction, the catalyst first needs to be reduced, and the reduced catalyst can then interact with CO$_2$ to promote the reaction. Generally, there are a couple of ways to supply electrons to the catalyst; electrochemical and photochemical methods.[15-19] The details about electro- and photochemical CO$_2$ reduction are discussed in the following sections.

3.1 Electrochemical CO₂ reduction

In an electrochemical system, a catalyst accepts electrons directly from a working electrode and form an active species that reduce CO_2 into various products within the reaction-diffusion layer. (Figure 2).[15] Since the amount of the active catalyst located in the reaction-diffusion layer is very small, larger surface area of the working electrode is often associated with the enhancement of electrochemical CO_2 reduction rate.[16] The applied potential is another key factor dictating the efficiency of electrochemical CO_2 reduction. The more negative the applied potential (higher overpotential), the greater the rate of catalytic reaction.

The materials of cathodic working electrode greatly influence the efficiency for CO_2 reduction. Pt cathode is not a good choice for the CO_2 reduction because it has exceptional activity for competing proton reduction reaction at very low-overpotential in protic solvents. Under such condition, the catalytic system suffers from low selectivity for CO_2 reduction over H_2 evolution. In contrast, glassy carbon electrode is a better option because it has a little large overpotential for the proton reduction, giving it an extensive negative potential window for the CO_2 reduction. Glassy carbon electrode is also easy to handle and non-toxic compared to Hg electrode.[16,17]
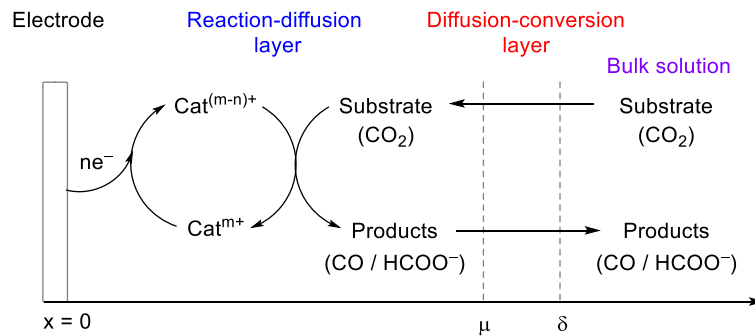

Figure 2: Electrochemical reaction in homogeneous catalysis, where x, μ, and δ corresponds to the distance from the electrode surface, thickness of reaction layer, and thickness of diffusion layer respectively.[15,16]

3.2 Photochemical CO₂ reduction

Photochemical CO_2 reduction can be carried out *via* dye-sensitized or non-sensitized catalysts. For the dye-sensitized CO_2 reduction, three components are required, which include photosensitizer (PS), sacrificial electron donor (SD), and a catalyst. PS is needed to extend the light absorption of the catalytic system, while SD is used as an electron source to regenerate PS. After absorbing a photon, quenching of the excited state of the PS may occur in two possible ways: reductive quenching or oxidative quenching for producing the reduced species of catalyst (Figure 3).[16,18-19] Ru polypyridyl complexes such as $[Ru(bpy)_3]^{2+}$ are frequently employed as PS to drive the photoreaction because they can harvest visible-light (λ_{max} = ~450–470 nm) and show relatively long excitation life-time (6 μs).[20-21] Ru PS is commonly reductively quenched by SD forming the one-electron reduced species, which then transfers the electron to a catalyst (Figure 4a). Metal complexes are commonly used as the catalyst, and the details are given in Section 5.[12-19]

For non-sensitized CO_2 reduction, only SD and catalyst are required. No additional PS unit is needed. The photocatalyst can harvest energy from light and catalyze CO_2 reduction by itself (Figure 4b). However, this category of photocatalysts is rare in literature, mainly limited to Re and Ir polypyridyl and metal porphyrin complexes.[22-26]

The most widely used SD in organic solvents are tertiary aliphatic amines such as triethylamine (TEA) and triethanolamine (TEOA). Coenzyme NAD(P)H models such as 1-benzyl-1,4-dihydronicotinamide (BNAH) and 1,3-dimethyl-2-phenyl-2,3-dihydro-1*H*-benzo[d]imidazole (BIH) are also used as SD (Figure 5).[16,19]
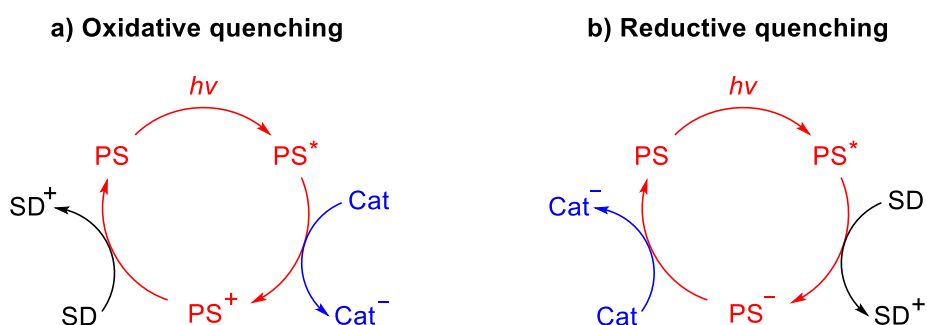

Figure 3: Mechanism for (a) oxidative quenching and (b) reductive quenching of photosensitizer (PS = photosensitizer; Cat = catalyst; SD = sacrificial electron donor).
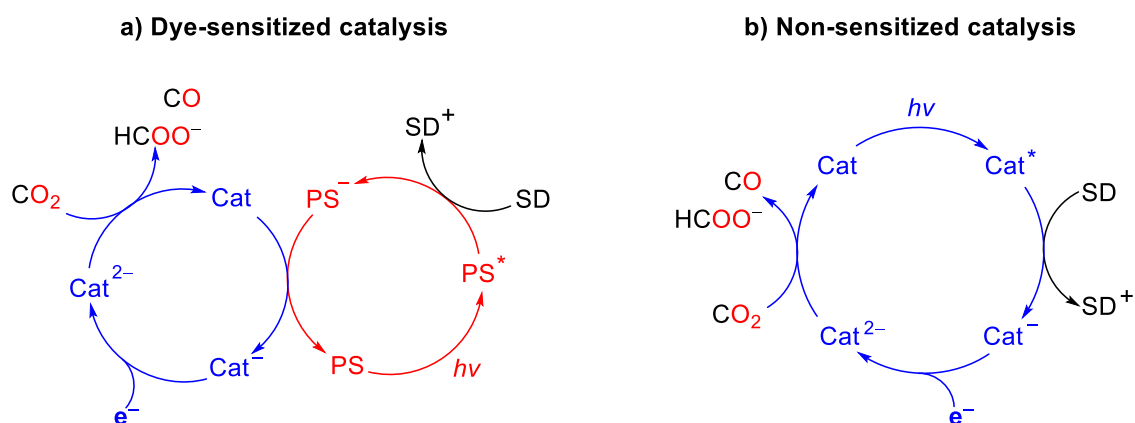
a) Dye-sensitized catalysis

b) Non-sensitized catalysis

Figure 4: Simplified reaction scheme for (a) dye-sensitized photochemical CO_2 reduction *via* reductive quenching pathway, and (b) non-sensitized photochemical CO_2 reduction. (PS = photosensitizer; Cat = catalyst; SD = sacrificial electron donor).[16]

TEA
E_{ox} = 0.96 V

TEOA
E_{ox} = 0.80 V

BNAH
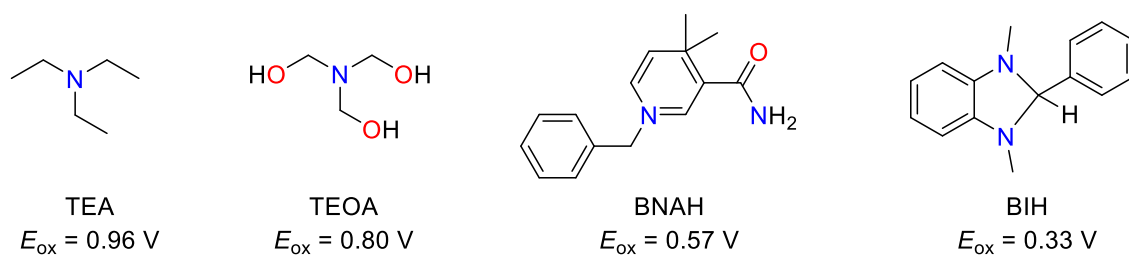E_{ox} = 0.57 V

BIH
E_{ox} = 0.33 V

Figure 5: Structures of commonly used sacrificial electron donors for photochemical CO_2 reduction and their oxidation potential. Redox potentials are given in V vs. SCE.[16,19]

4. Common factors concerning electro- and photochemical CO_2 reduction

4.1 Solvent effect

The solvent effect is one of the essential factors affecting the CO_2 reduction reaction. Solubility of CO_2, redox potential of catalyst, PS and the SD, and stability of reaction intermediates are all affected by the choice of solvent.[16] Most of the time, metal complexes with substitution-labile sites (where CO_2 would react) that is occupied by solvent molecules are utilized as catalysts. Therefore, solvents that weakly coordinate to the central metal ion are usually preferred (e.g., MeCN and DMF) so that these solvent ligands can be easily substituted by CO_2 during the catalytic cycle. It is note that, recently, DMF was found to be readily hydrolyzed to $HCOO^-$ in the presence of H_2O, which making it difficult to quantify $HCOO^-$ as a product of the CO_2 reduction. As an alternative, *N*,*N*-dimethylacetamide (DMA) has been proposed as a substitute for DMF due to their similar chemical properties, and higher stability of DMA towards hydrolysis.[27]

In principle, water is the ideal solvent for catalytic reaction because it is abundant, non-toxic, and able to dissolve many different kinds of molecules. However, CO_2 reduction in full aqueous solution has encountered several obstacles. For example, CO_2 has higher solubility in organic solvents (0.28 M in MeCN [28-29] and 0.23 M in DMF [29] at 20 $^\circ$C) than in aqueous medium (0.04 M in H_2O)[29-30]. High H_2O contents could decrease the quenching efficiency of the excited states of PS by sacrificial electron donor, which in turn suppressed the photocatalytic CO_2 reduction activity.[27] Moreover, metal catalyst and PS often suffer from poor stability in aqueous solution due to decomposition.[12,16,31]

4.2 Proton source

The addition of proton source or weak Brønsted acid (Table 1, eq. 3–4) (e.g., H_2O, methanol (MeOH), 2,2,2-trifluoroethanol (TFE), and phenol (PhOH)) often enhanced the catalytic CO_2 reduction.[32-33] In DMSO, the pK_a of H_2O, MeOH and TFE were estimated to be 31.4, 29.0, and 23.5 respectively.[34] It has been proposed that proton source could facilitate the cleavage of one of the two C–O bonds of CO_2 through push-pull mechanism (Figure 6a),[35] and also stabilizing the CO_2 adduct through H-bonding (Figure 6b).[36] However, the use of stronger acids for increasing the CO_2 reduction activity may not be a good strategy because the catalysts may reduce the acidic proton into hydrogen as a side reaction. The addition of Lewis acids was also reported to improve the catalytic reaction *via* "bimetallic effect" that assisting the C–O bond cleavage (Figure 6c).[37-39]
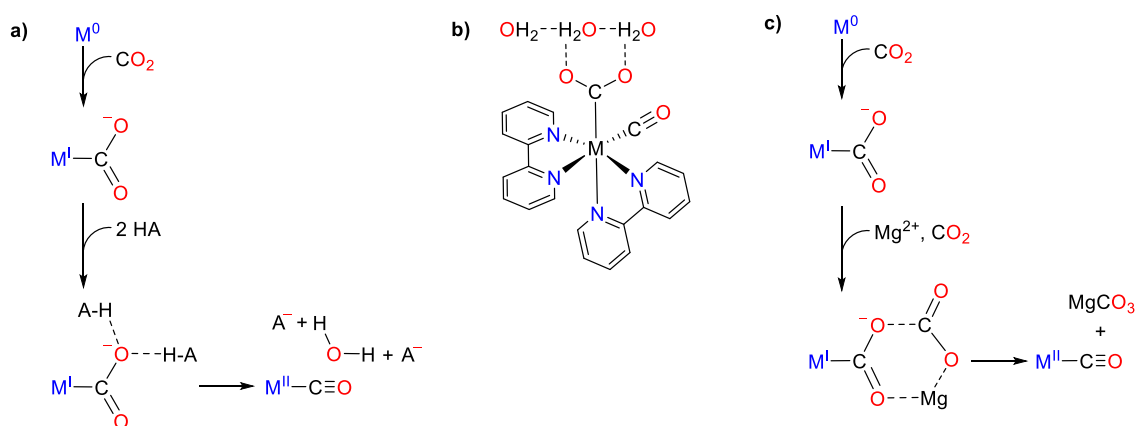

Figure 6: Effects of proton source in the cleavage of C–O bond (a),[35] in stabilizing the CO_2 adduct (b),[36] and as a role of Lewis acid in the cleavage of C–O bond (c).[37-39]

4.3 Coordination modes of CO_2 to metal centers

The CO_2 reduction activity of a metal complex is governed by their ability to bind the substrate (CO_2). The differences in CO_2 coordination modes often account for varied products formation (CO or $HCOO^-$). The electro- and photochemical CO_2 reduction begins with the generation of low valent metal complex with an open metal site (Section 3.1 and 3.2), followed by the interaction with CO_2 *via* two major modes: η^1-C binding mode or insertion into a metal-hydride bond (M–H bond) (Figure 7).[3,17]

Since the electron density of CO_2 is highly delocalized with a slightly positive and negative charges on carbon and oxygen respectively, CO_2 coordinates to the vacant site of an electron-rich low valent metal center through the electrophilic carbon atom with η^1-C coordination mode, and forms a CO_2 adduct (Figure 7a).[3,17] The metal-bound CO_2 adopts a bent geometry and the C–O bond is favorably cleaved in the presence of proton source (e.g., H_2O, MeOH, TFE, and PhOH) and gives CO as a product. Some representative examples following this pathway include Pd PPP pincer, Fe porphyrin, Co and Ni cyclam, as well as Ru and Re polypyridyl complexes.[5,6,15-18]

On the other hand, for metal-hydride species, the metal center shows slightly positive charge and negative charge locates at the hydride ligand. Therefore, when CO_2 is inserted into a M–H bond, one of the oxygen atoms should interact with the electrophilic metal center and the carbon atom with the nucleophilic hydride ligand, forming a metal formate intermediate (Figure 7b).[3,17] The metal formate intermediate can then release $HCOO^-$ as product. In electro- and photochemical systems, protonation of a low valent metal complex would afford metal-hydride. Ideal proton source is water because highly acidic proton source may promote further protonation of metal-hydride species that results in the competitive H_2 evolution reaction. Previously, metal-hydride of Ru, Rh and Ir polypyridine, Rh diphosphine, Ir PXP pincer (X = C and N), and Fe_4 carbonyl cluster have been identified as the active species for the catalytic production of $HCOO^-$.[3,5,17]

Until now, there is still no clear explanation as to why some metal complex activates CO_2 *via* η^1-C binding mode but not through the metal-hydride species, and *vice-versa*. While the above-mentioned examples showed that the CO_2 coordination modes are largely affected by the combination of metal ions, ligand systems, and proton sources. Upon reduction, the low valent metal complex may exhibit different binding affinity towards CO_2 (Figure 7a) and proton (Figure 7b). The former leads to CO_2 adduct and the latter to a metal-hydride. The CO_2 adduct favors CO production, while the metal-hydride may then react competitively with CO_2 and proton to yield $HCOO^-$ and H_2 respectively.[15]
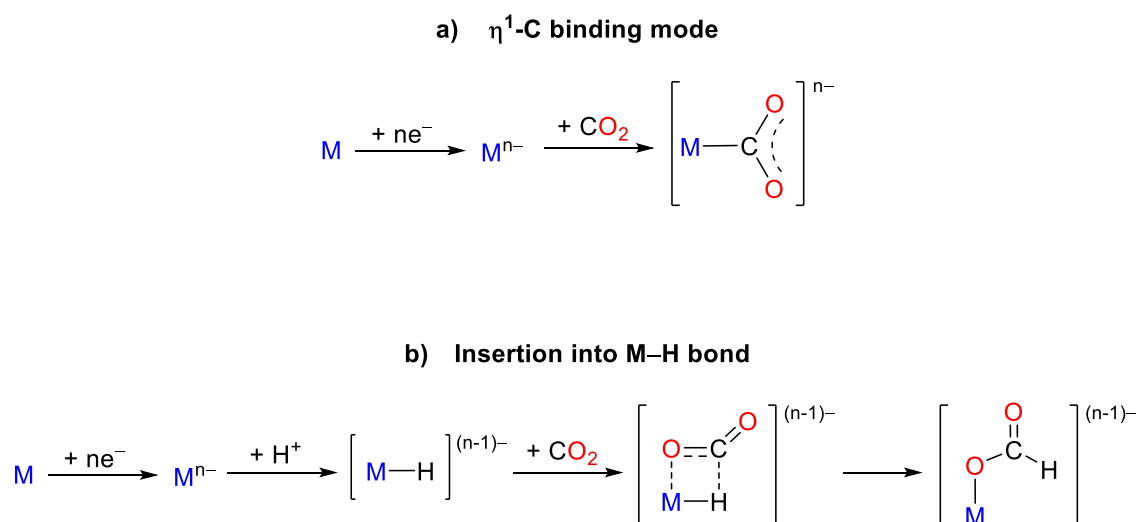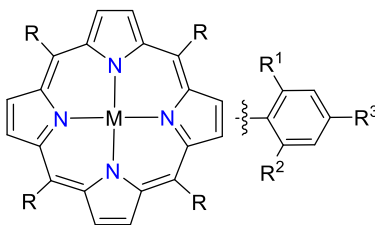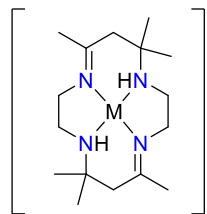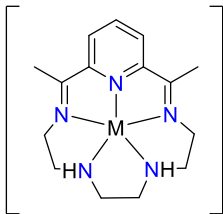
a) η^1-C binding mode

b) Insertion into M–H bond
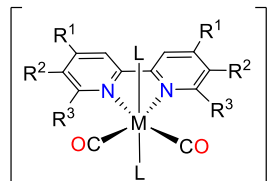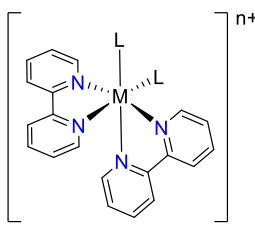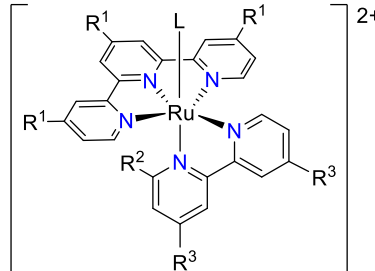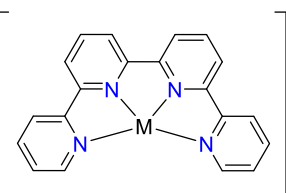
Figure 7: Common two modes of CO_2 binding to the metal center during CO_2 reduction.[3,17]

5. Molecular metal-based catalysts for CO_2 reduction

Regarding the catalysts for CO_2 reduction, the current trend in research focuses primarily on two types of compounds: solid materials and molecular catalysts. While appreciating the former approach,[40-45] molecular catalysts display several advantages. Molecular catalysts allow fine-tuning of their catalytic center by precise ligand design as 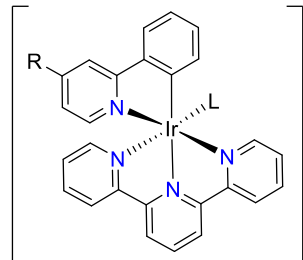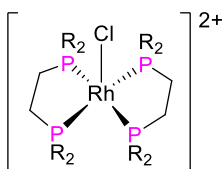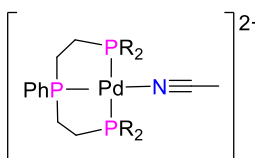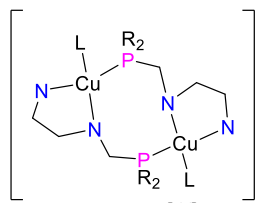to improve the selectivity and efficiency towards CO_2 reduction. For instance, the modification of Fe porphyrin with pendant OH functionalities significantly enhances the turn overnumber of catalysis.[32] The introduction of positively charged trimethylanilinium groups in the Fe porphyrin results in the CO_2 reduction at a low-overpotential.[22] Homogeneous molecular catalysts enable detailed mechanistic studies using various spectroscopic methods, and they can be fabricated as heterogeneous catalysts that are suitable for industrial uses.[5-6,12-13,15-19,69,71-72,74]

To date, various molecular catalysts for electro- and photochemical CO_2 reduction have been investigated using transition metal complexes with various kinds of ligands, for instance macrocyclic ligands, polypyridyl ligands, and phosphine ligands as shown in Table 2.[22-26,32,46-66] Initial works by Tanaka *et al*. demonstrated that $[Ru(bpy)_2(CO)_2]^{2+}$ and its derivatives were efficient catalysts for electro- and photochemical CO_2 reduction.[67-68] An attractive characteristic of Ru complexes was tunable products selectivity (i.e., CO and $HCOO^-$) by the reaction conditions.[58,69] Hence, Ru complexes have been widely explored and more will be discussed in Section 5.1. Lehn *et al*. firstly reported that $Re(bpy)(CO)_3(X)$ (X = Cl or Br) complexes could function as non-sensitized photocatalyst for CO_2 reduction.[24] Since then, a variety of Re complexes have been developed for electro- and photochemical CO_2 reduction.[16,18,19] Unlike Ru complexes, $Re(bpy)(CO)_3(X)$ and its derivatives mainly produce CO.[16,24,50] Savéant *et al*. have shown that Fe porphyrins could catalyze selective electrochemical CO_2 reduction to CO.[15,29,32-33,37-38] Fe porphyrins were also studied for photochemical CO_2 reduction in the presence and absence of PS.[22-23,70] In these complexes, ligands can provide a rigid support for the metal center, provide additional sites for electron storage, and stabilizing the low valent metal center and catalytic intermediate (CO_2 adduct).[5-6,17,71-72] Recently, there is a considerable interest in the use of cheap and abundant first-row transition metals (e.g., Mn, Fe, Co, Ni, Cu) as a substitute for noble metal-based catalysts in CO_2 reduction studies.[5-6,17,71-72] Among these first-row metals, Ni is particular intriguing due to its presence in the active center of natural catalyst for CO_2 reduction CODH,[8-11] which shall be elucidated in Section 5.2.

Table 2: Molecular metal-based catalysts for electro- and photochemical CO_2 reduction.

Macrocyclic ligands

R^1, R^2, R^3 = H; M = Co,[23] Fe[23,37]

R^1, R^2 = H, R^3 = NMe_3^+; M = Fe[22,70]

R^1, R^2 = OH, R^3 = H; M = Fe,[22,32] Cu[46]

M = Ni, Co[47-48]

M = Fe, Co[49]

Polypyridine ligands

R^1, R^2, R^3 = H; M = Re,[24,50] Os,[51] Ru,[52] Mn[53]

R^1, R^3 = H, R^2 = COOH; M = Mn[54]

R^1, R^2 = H, R^3 = Mesityl; M = Ru,[52,55] Mn[56]

M = Os,[57] Ru,[58] Rh[57]

R^1, R^2, R^3 = H[59-60]

R^1 = tBu, R^2 = H, R^3 = CH_3[61]

R^1 = tBu, R^2 = CH_3, R^3 = H[61]

M = Fe,[62] Co,[62] Cu[63]

R = H[25]

R = CH_3[26]

Phosphine ligands

R = Ph[64]

R = C_2H_5 / C_6H_{11} / Ph[65]

R = Ph[66]

5.1 Ru polypyridyl complexes for electro- and photochemical CO_2 reduction

Ru polypyridyl complexes with labile coordination sites, such as $[Ru(NNN)(NN)(L)]^{n+}$, $[Ru(NN)_2(L)_2]^{n+}$, and $[Ru(NN)(L)_4]^{n+}$ derivatives (where NNN: tridentate polypyridine ligand; NN: bidentate polypyridine ligand; L: monodentate labile ligand) are known to exhibit promising activity for CO_2 reduction by taking advantage of their multiple accessible redox states.[52,55,58-61] In these systems, polypyridine ligands play an essential role as an "electron reservoir" in addition to Ru ions as a CO_2-interaction site (Figure 8).

Tanaka and co-workers first reported the electrocatalytic CO_2 reduction by $[Ru(bpy)_2(CO)_2]^{2+}$ to yield CO and $HCOO^-$.[58,67] Meyer *et al*. later demonstrated that $[Ru(tpy)(bpy)(MeCN)]^{2+}$ could catalyze electrochemical CO_2 reduction as well. Two sequential one-electron reduction took place at the lowest π^* orbitals of tpy and bpy ligands to give the doubly-reduced $[Ru(tpy^-)(bpy^-)(MeCN)]^0$, which can bind CO_2 to form the CO_2 adduct, $[Ru(tpy)(bpy)(CO_2^{2-})]^0$ (Figure 8). Further ligand-based reduction and oxide transfer produce CO as final product.[60,73-74]

Multi-electron storage

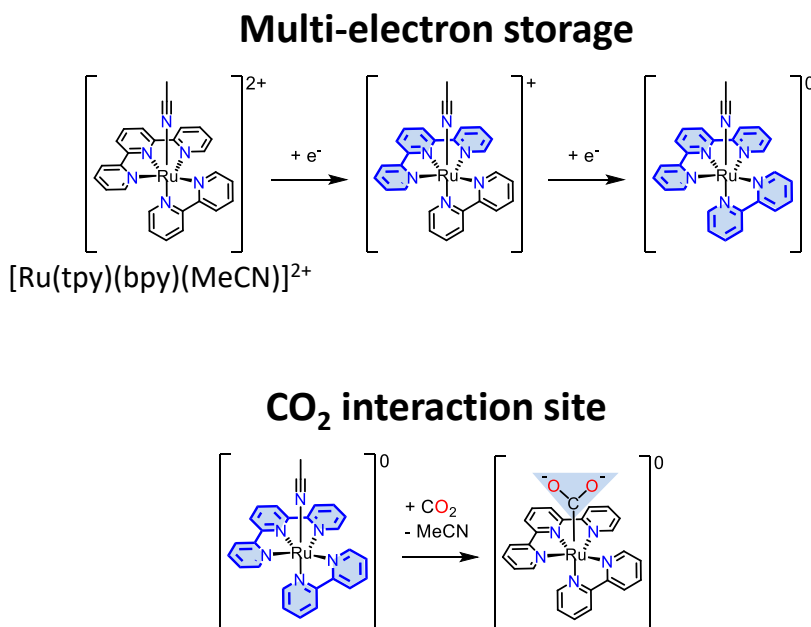$[Ru(tpy)(bpy)(MeCN)]^{2+}$

CO_2 interaction site

Figure 8: Proposed mechanism for CO_2 activation by $[Ru(tpy)(bpy)(MeCN)]^{2+}$. Reduced ligands are hightlighted in blue.[60,74]

Another interesting feature about Ru electrocatalysts is the ability to produce various reduction products, such as CO and $HCOO^-$. Tanaka and co-workers observed that $[Ru(bpy)_2(CO)_2]^{2+}$ can produce a mixture of CO and H_2 in slight acidic conditions (pH = 6), while $HCOO^-$ was the major product under slight basic conditions (pH = 9).[58,69] The pH dependent product selectivity was explained using acid-base equilibrium between CO_2 adducts. The carbonyl complex $[Ru(bpy)_2(CO)_2]^{2+}$ exists as the most stable species under acidic environment that favors CO production (blue path), while the carboxylic acid complex $[Ru(bpy)_2(CO)(COOH)]^+$ was the major species under basic condition that prefers $HCOO^-$ formation (red path) (Figure 9).[58] On the other hand, Meyer et al. proposed that the $HCOO^-$ production was due to the CO_2 insertion into a Ru–H bond, forming the $[Ru(bpy)_2(CO)(OC(O)H)]^0$ complex that released $HCOO^-$ upon reduction (Figure 10).[75] Until now, both the proposed mechanisms were often been quoted to describe the $HCOO^-$ production.
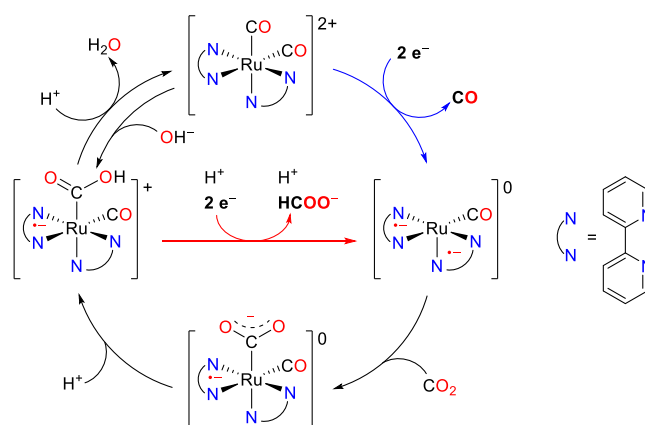

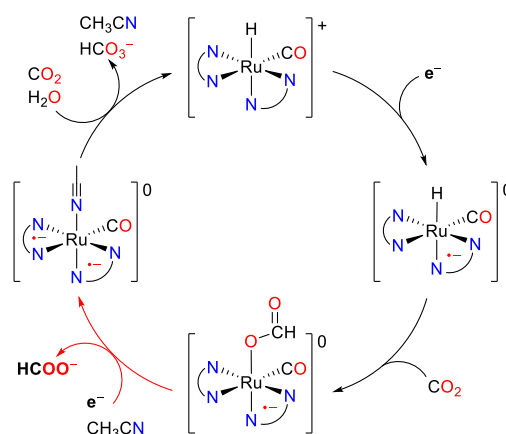Figure 9: Mechanism proposed by Tanaka et al. for CO and $HCOO^-$ production.[58,69]

Figure 10: Mechanism proposed by Meyer et al. for $HCOO^-$ production.[75]

Visible-light driven photochemical CO_2 reduction have been widely investigated using $[Ru(NN)_3]^{2+}$ complexes as a PS, and $[Ru(NN)_2(L)_2]^{n+}$ and $[Ru(NN)(L)_4]^{n+}$ complexes as a catalyst. In early 1985, Lehn *et al*. found that high concentration of $[Ru(bpy)_3]^{2+}$ could promote photochemical CO_2 reduction to $HCOO^-$.[76] They proposed that the real active catalyst in the system for $HCOO^-$ production was the decomposed species, $[Ru(bpy)_2(S)_2]^{2+}$ (S = monodentate solvent ligands) (Figure 11), while the remaining $[Ru(bpy)_3]^{2+}$ acts as the PS. This was later supported by Tanaka *et al*. where the mixture of $[Ru(bpy)_2(CO)_2]^{2+}$ and $[Ru(bpy)_3]^{2+}$ in CO_2-saturated DMF/TEOA (4:1, v/v) selectively produced $HCOO^-$.[68] These $[Ru(NN)_2(L)_2]^{n+}$ and $[Ru(NN)(L)_4]^{n+}$ complexes required an additional PS to perform CO_2 reduction (dye-sensitized catalysts) because they hardly absorb visible-light, which is different from $[Re(NN)(L)_4]^{n+}$ complexes (non-sensitized catalysts).[24]

SD = sacrificial electron donor; S = solvent
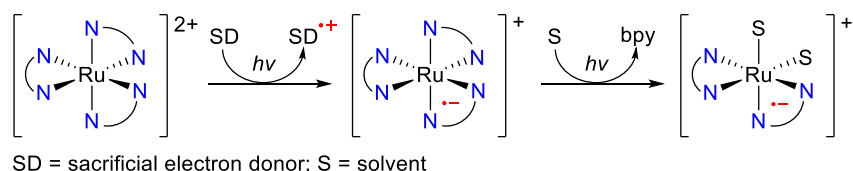
Figure 11: Proposed mechanism for the photo-induced decomposition of $[Ru(bpy)_3]^{2+}$.[76]

During electrolysis or photolysis, $[Ru(bpy)(L)_4]^{n+}$ and $[Ru(bpy)_2(L)_2]^{n+}$ -type complexes often formed black insoluble polymeric species, $[Ru(bpy)(CO)_2]_n$, which in turn decrease the efficiency of catalytic reaction (Figure 12).[68,77-78] In addition, high energy is required to access the active two-electron reduced Ru species (Figure 8 & 9 & 10). In order to overcome these drawbacks, ligand modification of Ru polypyridyl complexes have been studied to control the redox properties and catalytic activity for CO_2 reduction.[19,52,55,61,78-79]

Figure 12: Proposed mechanism for the formation of Ru polymer, $[Ru(bpy)(CO)_2]_n$.[16]

5.2 Ni complexes for electro- and photochemical CO_2 reduction

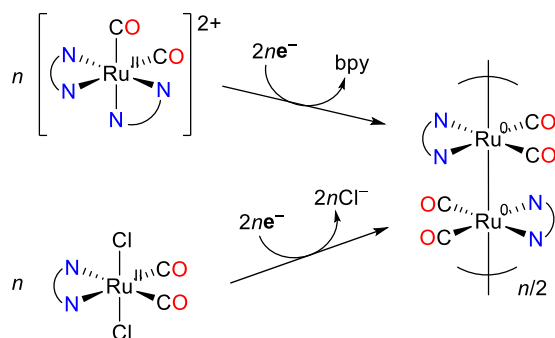Earth-abundant Ni metal complexes have been explored for CO_2 reduction reactions because of its low cost, relatively low toxicity, as well as its presence in the active-site of natural catalysts (e.g., CODH, coenzyme F_{430}, NiFe hydrogenases, etc).[8-11]

In 1980, Eisenberg *et al.* first reported that $[Ni^{II}(cyclam)]^{2+}$ -type complexes (cyclam = 1,4,8,11-tetraazacyclotetradecane) (Table 2) could catalyze electrochemical CO_2 reduction to CO.[47] The catalytically active species was thought to be the one-electron reduced $[Ni^{I}(cyclam)]^{+}$ species. The evidence from crystal structures and mechanistic studies indicated the NH protons in the macrocycle ligand were essential in stabilizing the CO_2 adduct *via* H-bonding (Figure 13).[80-82] In addition, Ni polypyridyl complexes, such as $[Ni(bpy)_3]^{2+}$, $[Ni(tpy)_2]^{2+}$, and $[Ni(qtpy)(MeCN)_2]^{2+}$ were shown to catalyze electrochemical CO_2 reduction to CO. Both Ni- and polypyridyl ligand-based reduction were involved in promoting the CO_2 reduction.[83-85] Furthermore, dinuclear and trinuclear Ni complexes supported by phosphine ligands have also been studied for electrochemical CO_2 reduction. These multinuclear Ni complexes produced CO selectively under aprotic condition and yield $HCOO^-$ exclusively in the presence of H^+ donor.[86-87]
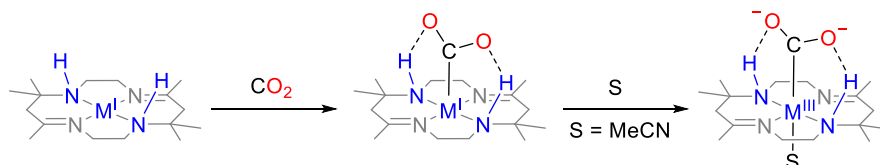

Figure 13: Formation of CO_2 adduct assisted by NH protons of macrocyclic ligands.[80-82]

The initial example of Ni photocatalyst for CO_2 reduction was demonstrated by using $[Ni^{II}(cyclam)]^{2+}$ as catalyst, $[Ru(bpy)_3]^{2+}$ as PS, and ascorbic acid as SD in aqueous solution, which produced mixture of CO and H_2 (TON_{CO} = 0.052–0.1).[81] Recently, Ni^{II} *N*-heterocyclic carbene isoquinoline complexes were shown to catalyze photochemical CO_2 reduction to CO (TOF = 3.9 s^{-1}, quantum yield = 0.01 %) in the presence of $Ir(ppy)_3$ (ppy = 2-phenylpyridine) PS and TEA as SD under visible-light irradiation.[88] Kojima *et al.* demonstrated that a Ni^{II} complex bearing S_2N_2 -type tetradentate ligand could promote selective photochemical CO_2 reduction to CO (TOF = ~19 h^{-1}, quantum yield = 1.42 %) in the presence of $[Ru(bpy)_3]^{2+}$ as PS and BIH as SD.[89] The chemical structure of above-mentioned Ni complexes are shown in Figure 14.

Previous studies show that the ability of the Ni catalysts to accumulate multiple electrons near the thermodynamic potential of CO_2 reduction is the key for the efficient electro- and photochemical CO_2 reduction. The utilization of redox-active ligand was suggested to be beneficial for Ni catalysts by providing an additional site for storing electrons. However, among the synthetic systems reported, none are as efficient as the nature's Ni-containing CODH system.[90] Ongoing research is necessary to rationally design a new generation of Ni catalysts with improve catalytic performance for CO_2 reduction.
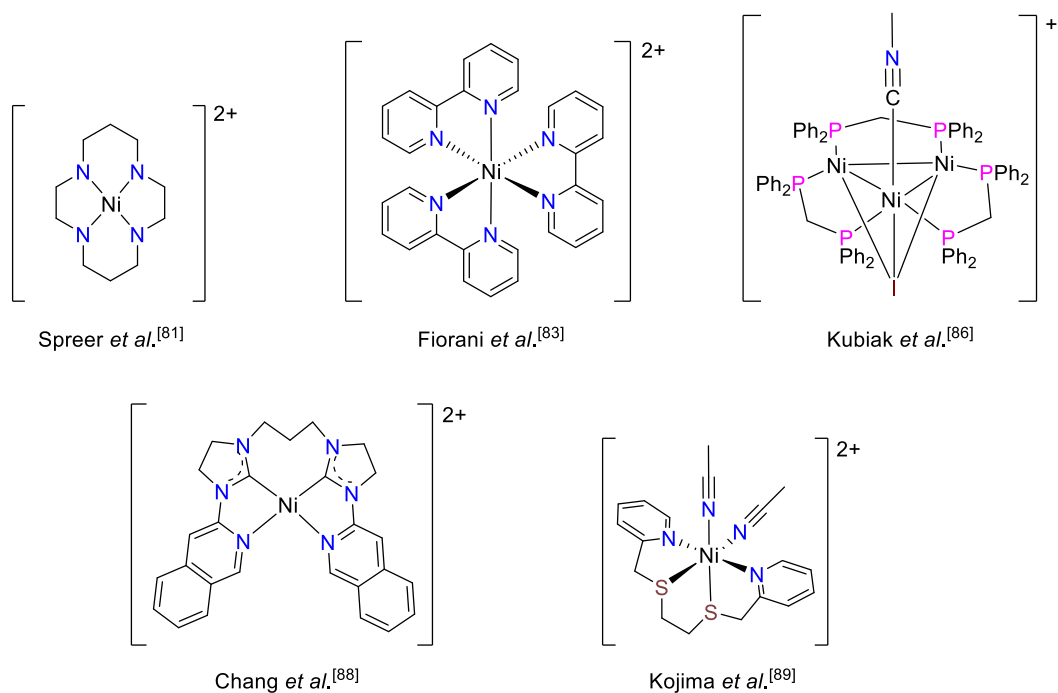

Figure 14: Examples of Ni complexes studied for electro- and photochemical CO_2 reduction.

6. Aim of this thesis

Even though numerous metal complexes have been reported to catalyze electro- and photochemical CO_2 reduction, they are still far from practical use. For application purposes, these metal complexes should show long-term stability, high turnover number, high turnover frequency, and low-overpotential (in the case of electrocatalyst).

In this study, I ought to improve the catalyst performance for CO_2 reduction by considering issues as mentioned above. First of all, the well-established Ru catalyst, $[Ru(tpy)(bpy)(MeCN)]^{2+}$ is known to bind and activate CO_2 after two-electron reduction. However, the necessity to achieve the doubly-reduced state led to an increase in the overpotential for electrochemical CO_2 reduction and limiting its application in photochemical CO_2 reduction. Since the carbon atom of CO_2 is slightly electrophilic, the installation of a strong electron donating phosphine ligand at the *trans* position to the substitution-labile site (where CO_2 will bind) is expected to activate the Ru complex at its one-electron reduced state to bind CO_2. Therefore, phosphine-substituted Ru polypyridyl complex should display improved electro- and photochemical CO_2 reduction activity. Second, as inspired from previous studies, I aim to develop a new generation of earth-abundant Ni-based catalysts for CO_2 reduction. These Ni complexes contain redox-active pentadentate N5 ligands that can provide rigid support for Ni ions and to function as an "electron reservoir", while Ni ions acts as CO_2-interaction site. These Ni complexes should show promising behavior for photochemical CO_2 reduction reaction.

7. Survey of this thesis

Chapter 1 describes the low-overpotential electrochemical CO_2 reduction by a phosphine-substituted Ru polypyridyl complex, **RuP**. The introduction of a phosphine ligand at the position *trans* to the labile ligand allow **RuP** to promote electrocatalytic CO_2 reduction to CO (TOF = 4.7 s^{-1}) at low-overpotential (η = 0.4 V). Detailed mechanistic investigations revealed that the σ- character of the phosphine ligand destabilizes the Ru–N(MeCN) bond, while π-back donating character of the phosphine ligand participates in stabilizing the Ru–C(CO_2) bond of CO_2 adduct. As a result, **RuP** can bind CO_2 at the one-electron reduced state and catalyze CO_2 reduction with a low-overpotential, which is superior to conventional Ru polypyridyl complexes that bind CO_2 at its two-electron reduced state.

Chapter 2 investigates the photocatalytic CO_2 reduction activity by **RuP**. Results from photolysis experiments corroborated that **RuP** can catalyze CO_2 reduction under visible-light irradiation without additional photosensitizer. To our knowledge, **RuP** is the first example of non-sensitized mononuclear Ru photocatalyst for CO_2 reduction. The key to success is the Ru polypyridyl scaffold that allows visible-light harvesting, ability to bind CO_2 at the one-electron reduced state, and a substitution-labile site for CO_2 binding. The selectivity of the product can be tuned depending on the acidity of the reaction media. Under slightly acidic condition, > 94 % of CO (TOF = 14.5 h^{-1}) was selectively produced, while > 99 % of HCOOH (TOF = 3.5 h^{-1}) was selectively formed under slightly basic environment.

Chapter 3 describes the syntheses, characterization, redox behavior, and photochemical CO_2 reduction activity of Ni complexes containing redox-active pentadentate N5 ligands. Under inert atmosphere, these Ni complexes exhibit two reversible redox waves within –2.0 V vs. ferrocene/ferrocenium that is attributed to the Ni-based and ligand-based reduction. Under CO_2, current enhancement was observed in the presence of proton source. Thus, these Ni complexes are promising for carry out CO_2 reduction reaction. Preliminary results showed that these Ni complexes can promote photocatalytic CO_2 reduction to produce CO under visible-light irradiation with the assistance of Ru photosensitizer. Future work is underway to optimize the reaction conditions and shed light into the mechanistic study.

References:

1) A. Goeppert, M. Czaun, J. P. Jones, G. K. Surya Prakash, G. A. Olah, *Chem. Soc. Rev.* 2014, **43**, 7995-8048.

2) M. Mikkelsen, M. Jørgensen, F. C. Krebs, *Energy Environ. Sci.* 2010, **3**, 43-81.

3) A. M. Appel, J. E. Bercaw, A. B. Bocarsly, H. Dobbek, D. L. DuBois, M. Dupuis, J. G. Ferry, E. Fujita, R. Hille, P. J. A. Kenis, C. A. Kerfeld, R. H. Morris, C. H. F. Peden, A. R. Portis, S. W. Ragsdale, T. B. Rauchfuss, J. N. H. Reek, L. C. Seefeldt, R. K. Thauer, G. L. Waldrop, *Chem. Rev.* 2013, **113**, 6621-6658.

4) J. J. Concepcion, R. L. House, J. M. Papanikolas, T. J. Meyer, *Proc. Natl. Acad. Sci. U.S.A.* 2012, **109**, 15560-15564.

5) E. E. Benson, C. P. Kubiak, A. J. Sathrum, J. M. Smieja, *Chem. Soc. Rev.* 2009, **38**, 89-99.

6) J. Schneider, H. Jia, J. T. Muckerman, E. Fujita, *Chem. Soc. Rev.* 2012, **41**, 2036-2051.

7) Y. Umena, K. Kawakami, J. Shen, N. Kamiya, *Nature* 2010, **473**, 55-60.

8) H. Dobbek, V. Svetlitchnyl, L. Gremer, R. Huber, O. Meyer, *Science* 2001, **293**, 1281-1285.

9) J. Jeoung, H. Dobbek, *Science*, 2007, **318**, 1461-1464.

10) J. Fesseler, J. Jeoung, Dobbek, *Angew. Chem., Int. Ed.* 2015, **29**, 8560-8564.

11) M. Can, F. A. Armstrong, S. W. Ragsdale, *Chem. Rev.* 2014, **114**, 4149-4174.

12) S. Berardi, S. Drouet, L. Francàs, C. Gimbert-Suriñach, M. Guttentag, C. Richmond, T. Stoll, A. Llobet, *Chem. Soc. Rev.* 2014, **43**, 7501-7519.

13) J. H. Alstrum-Acevedo, M. K. Brennaman, T. J. Meyer, *Inorg. Chem.* 2005, **44**, 6802-6827.

14) L. Favereau, A. Makhal, Y. Pellegrin, E. Blart, J. Petersson, E. Göransson, L. Hammarström, F. Odobel, *J. Am. Chem. Soc.* 2016, **138**, 3752-3760.

15) C. Costentin, M. Robert, J. M. Savéant, *Chem. Soc. Rev.* 2013, **42**, 2423–2436.

16) Y. Kuramochi, O. Ishitani, H. Ishida, *Coord. Chem. Rev.* 2017, DOI:10.1016/j.ccr.2017.11.023.

17) R. Francke, B. Schille. M. Roemelt, *Chem. Rev.* 2018, **118**, 4631-4701.

18) Y. Yamazaki, H. Takeda, O. Ishitani, *J. Photochem. Photobiol. C* 2015, **25**, 106-137.

19) Y. Tamaki, O. Ishitani, *ACS Catal.* 2017, **7**, 3394-3409.

20) D. M. Arias-Rotondo, J. K. McCusker, *Chem. Soc. Rev.* 2016, **45**, 5803-5820.

21) C. K. Prier, D. A. Rankic, D. W. C. MacMillan, *Chem. Rev.* 2013, **113**, 5322-5363.

22) H. Rao, L. C. Schmidt, J. Bonin, M. Robert, *Nature* 2017, **548**, 74-77.

23) T. Dhanasekaran, J. Grodkowski, P. Neta, P. Hambright, E. Fujita, *J. Phys. Chem. A* 1999, **103**, 7742-7748.

24) J. Hawecker, J.-M. Lehn, R. Ziessel, *J. Chem. Soc., Chem. Commun.* 1983, 536–538.

25) R. O. Reithmeier, S.Meister, B. Rieger, A. Siebel, M. Tschurl, U. Heiz, E. Herdtweck, *Dalton Trans.* 2014, **43**, 13259–13269.

26) S. Sato, T. Morikawa, T. Kajino, O. Ishitani, *Angew. Chem. Int. Ed.* 2013, **52**, 988–992.

27) Y. Kuramochi, M. Kamiya, H. Ishida, *Inorg. Chem.* 2014, **53**, 3326-3332.

28) J. Wang, *Analytical Electrochemistry*, 3rd ed.; John Wiley & Sons, Inc.: Hoboken, NJ, 2006.

29) I. Bhugun, D. Lexa, J. M. Savéant, *Anal. Chem.* 1994, **66**, 3994-3996.

30) D. R. Lide, *Handbook of Chemistry and Physics*, 81st ed.; CRC Press: Boca Raton, FL, 2000.

31) C. Kutal, M. A. Weber, G. Ferraudi, D. Geiger, *Organometallics*, 1985, **4**, 2161-2166.

32) C. Costentin, S. Drouet, M. Robert, J. M. Savéant, *Science* 2012, **338**, 90−94.

33) I. Bhugun, D. Lexa, J. M. Savéant, *J. Am. Chem. Soc.* 1996, **118**, 1769-1776.

34) W. N. Olmstead, Z. Margolin, F. G. Bordwell, *J. Org. Chem.* 1980, **45**, 3295-3299.

35) C. Costentin, S. Drouet, G. Passard, M. Robert, J. M. Savéant, *J. Am. Chem. Soc.* 2013, **135**, 9023-9031.

36) H. Tanaka, H. Nagao, S. Peng, K. Tanaka, *Organometallics*, 1992, **11**, 1450-1451.

37) M. Hammouche, D. Lexa, M. Momenteau, J. M. Savéant, *J. Am. Chem. Soc.* 1991, **113**, 8455-8466.

38) I. Bhugun, D. Lexa, J. M. Savéant, *J. Phys. Chem.* 1996, **100**, 19981-19985.

39) M. D. Sampson, C. P. Kubiak, *J. Am. Chem. Soc.* 2016, **138**, 1386-1393.

40) T. Inoue, A. Fujishima, S. Konishi, K. Honda, *Nature* 1979, **277**, 637-638.

41) T. Hisatomi, K. Domen, *Faraday Discuss.* 2017, **198**, 11-35.

42) N. S. Lewis, *Science* 2016, **351**, aad1920.

43) C. W. Li, J. Ciston, M. W. Kanan, *Nature* 2014, **508**, 504-507.

44) M. Schreier, L. Curvat, F. Giordano, L. Steier, A. Abate, S. M. Zakeeruddin, J. Luo, M. T. Mayer, M. Grätzel, *Nature Commun.* 2015, **6**, 7326.

45) T. R. Cook, D. K. Dogutan, S. Y. Reece, Y. Surendranath, T. S. Teets, D. G. Nocera, *Chem. Rev*. 2010, **110**, 6474-6502.

46) Z. Weng, J. Jiang, Y. Wu, Z. Wu, X. Guo, K. L. Materna, W. Liu, V. S. Batista, G. W. Brudbig, H. Wang, *J. Am. Chem. Soc.* 2016, **138**, 8076-8079.

47) B. J. Fisher, R. Eisenberg, *J. Am. Chem. Soc.* 1980, **102**, 7361-7363.

48) S. Matsuoka, K. Yamamoto, T. Ogata, M. Kusaba, N. Nakashima, E. Fujita, *J. Am. Chem. Soc.* 1993, **115**, 601-609.

49) L. Chen, Z. Guo, X. Wei, C. Gallenkamp, J. Bonin, E. Anxolabéhère-Mallart, K. Lau, T. Lau, M. Robert, *J. Am. Chem. Soc.* 2015, **137**, 10918-10921.

50) J. Hawecker, J.-M. Lehn, R. Ziessel, *J. Chem. Soc., Chem. Commun.* 1984, 328–330.

51) J. Chauvin, F. Lafolet, S. Chardon-Noblat, A. Deronzier, M. Jakonen, M. Haukka, *Chem. Eur. J.*, 2011, **17**, 4313–4322.

52) Y. Kuramochi, J. Itabashi, K. Fukaya, A. Enomoto, M. Yoshida, H. Ishida, *Chem. Sci.*, 2015, **6**, 3063–3074.

53) M. Bourrez, F. Molton, S. Chardon-Noblat, A. Deronzier, *Angew. Chem., Int. Ed.*, 2011, **50**, 9903–9906.

54) H. Fei, M. D. Sampson, Y. Lee, C. P. Kubiak, S. M. Cohen, *Inorg. Chem.*, 2015, **54**, 6821–6828.

55) C. W. Machan, M. D. Sampson, C. P. Kubiak, *J. Am. Chem. Soc.* 2015, **137**, 8564-8571.

56) M. D. Sampson, A. D. Nguyen, K. A. Grice, C. E. Moore, A. L. Rheingold, C. P. Kubiak, *J. Am. Chem. Soc.*, 2014, **136**, 5460–5471.

57) C. M. Bolinger, N. Story, B. P. Sullivan, T. J. Meyer, *Inorg. Chem.* 1988, **27**, 4582–4587.

58) H. Ishida, K. Tanaka, T. Tanaka, *Organometallics* 1987, **6**, 181–186.

59) H. Nagao, T. Mizukawa, K. Tanaka, *Inorg. Chem.* 1994, **33**, 3415–3420.

60) Z. Chen, C. Chen, D. R. Weinberg, P. Kang, J. J. Concepcion, D. P. Harrison, M. S. Brookhart, T. J. Meyer, *Chem. Commun.* 2011, **47**, 12607–12609.

61) B. A. Johnson, S. Maji, H. Agarwala, T. A. White, E. Mijangos, S. Ott, *Angew. Chem. Int. Ed.* 2015, **55**, 1825–1829.

62) Z. Guo, S. Cheng, C. Cometto, E. Anxolabéhère-Mallart, S. Ng, C. Ko, G. Liu, L. Chen, M. Robert, T. Lau, *J. Am. Chem. Soc.* 2016, **138**, 9413-9416.

63) Z. Guo, F. Yu, Y. Yang, C. Leung, S. Ng, C. Ko, C. Cometto, T. Lau, M. Robert, *ChemSusChem.* 2017, **20**, 4009-4013.

64) S. Slater, J. H. Wagenknecht, *J. Am. Chem. Soc.* 1984, **106**, 5367-5368.

65) D. L. DuBois, A. Miedaner, R. C. Haltiwanger, *J. Am. Chem. Soc.* 1991, **113**, 8753-8764.

66) R. J. Haines, R. E. Wittrig, C. P. Kubiak, *Inorg. Chem.* 1994, **33**, 4723-4728.

67) H. Ishida, H. Tanaka, K. Tanaka, T. Tanaka, *J. Chem. Soc., Chem. Commun.* 1987, 131-132.

68) H. Ishida, T. Terada, K. Tanaka, T. Tanaka, *Inorg. Chem.* 1990, **29**, 905-911.

69) K. Kobayashi, K. Tanaka, *Phys. Chem. Chem. Phys.* 2014, **16**, 2240-2250.

70) H. Rao, J. Bonin, M. Robert, *Chem. Commun.* 2017, **53**, 2830-2833.

71) H. Takeda, C. Cometto, O. Ishitani, M. Robert, *ACS Catal.* 2017, **7**, 70-88.

72) Noémie Elgrishi, M. B. Chambers, X. Wang, M. Fontecave, *Chem Soc. Rev.* 2017, **46**, 761-796.

73) Z. Chen, P. Kang, M. Zhang, T. J. Meyer, *Chem. Commun.* 2014, **50**, 335-337.

74) P. Kang, Z. Chen, M. Brookhart, T. J. Meyer, *Top. Catal.* 2015, **58**, 30-45.

75) J. R. Pugh, M. R. M. Bruce, B. P. Sullivan, T. J. Meyer, *Inorg. Chem.* 1991, **30**, 86-91.

76) J. Hawecker, J.-M. Lehn, R. Ziessel, *J. Chem. Soc. Chem. Commun.* 1985, 56-58.

77) J.-M. Lehn, R. Ziessel, *J. Organomet. Chem.* 1990, **382**, 157–173.

78) Y. Tamaki, T. Morimoto, K. Koike, O. Ishitani, *Proc. Natl. Acad. Sci. U. S. A.* 2012, **109**, 15673–15678.

79) T. Kajiwara, M. Fujii, M. Tsujimoto, K. Kobayashi, M. Higuchi, K. Tanaka, S. Kitagawa, *Angew. Chem. Int. Ed.* 2016, **55**, 2697-2700.

80) E. Fujita, D. J. Szalda, C. Creutz, N. Sutin, *J. Am. Chem. Soc.* 1988, **110**, 4870-4871.

81) J. L. Grant, K. Goswami, L. O. Spreer, J. W. Otvos, M. Calvin, *J. Chem. Soc. Dalton Trans.* 1987, 2105-2109.

82) J. Schnerider, H. Jia, K. Kobiro, D. E. Cabelli, J. T. Muckerman, E. Fujita, *Energy Environ. Sci.* 2012, **5**, 9502-9510.

83) S. Daniele, P. Ugo, G. Bontempelli and M. Fiorani, *J. Electroanal. Chem.* 1987, **219**, 259–271.

84) N. Elgrishi, M. B. Chambers, V. Artero, M. Fontecave, *Phys. Chem. Chem. Phys.* 2014, **16**, 13635-13644.

85) K. Lam, K. Wong, S. Yang, C. Che, *J. Chem. Soc. Dalton Trans.* 1995, 1103-1107.

86) K. S. Ratliff, R. E. Lentz, C. P. Kubiak, *Organometallics*, 1992, **11**, 1986-1988.

87) E. Simón-Manso, C. P. Kubiak, *Organometallics*, 2005, **24**, 96-102.

88) V. S. Thoi, N. Kornienko, C. G. Margarit, P. Yang, C. J. Chang, *J. Am. Chem. Soc.* 2013, **135**, 14413-14424.

89) D. Hong, Y. Tsukakoshi, H. Kotani, T. Ishizuka, T. Kojima, *J. Am. Chem. Soc*. 2017, **139**, 6538-6541.

90) J. Wang, W. Liu, D. Zhong, T. Lu, *Coord. Chem. Rev*. 2017, DOI:10.1016/j.ccr.2017.12.009.

Chapter 1

Low-overpotential CO_2 reduction by phosphine-substituted Ru(II) polypyridyl complex

Chem. Commun. 2018, **54**, 6915-6918.

Introduction

Catalytic CO_2 reduction into liquid fuels and commodity chemicals under benign condition has drawn tremendous attention, not only as a means to decrease the competition for limited fossil fuel reserves but also help to reduce the concentration of atmospheric CO_2.[1-6] There are a continuously increasing number of molecular catalysts to convert CO_2 into fuels, such as $HCOOH$[1-6] and deeply reduced products.[7-10] In addition, the reduction of CO_2 to carbon monoxide (CO)[11-12] is also favourable because a wide variety of fuels and commodity chemicals can be produced from CO via Fischer−Tropsch synthesis. Therefore, the development of a catalyst that can convert CO_2 to CO is an attractive research target and there have been numerous reports on transition metal complexes that can catalyse the reaction.[13-20]

Ru polypyridyl complexes with a monodentate ligand are known to exhibit promising CO_2 reduction activity by taking advantage of multiple accessible redox states.[15-16,21] In these systems, polypyridine ligands play an essential role as an electron reservoir in addition to Ru ions as a CO_2-interaction site.[22] A representative example of such catalysts is a Ru polypyridyl complex, $[Ru^{II}(tpy)(bpy)(MeCN)]^{2+}$ (**RuN**, where tpy = 2,2′:6′,2″-terpyridine; bpy = 2,2'-bipyridine, Fig. 1, left).[21] This complex undergoes ligand-based multielectron reduction reaction to give $[Ru^{II}(tpy^-)(bpy^-)(MeCN)]^0$, and forms a CO_2 adduct, $[Ru^{II}(tpy)(bpy)(CO_2{}^{2-})]^0$, via a ligand exchange reaction, which results in the catalytic conversion of CO_2.[15,21-22] However, the potentials required to access their active, two-electron reduced species causes the increase in overpotential (i.e., high energy is required to drive the catalytic reaction). In this connection, ligand modification of Ru polypyridyl complexes has extensively been studied to control over their redox properties and catalytic activity for CO_2 reduction.[21-29]

Phosphine ligands are an attractive class of molecules[30-34] because these ligands can control the electronic structures of the metal centres of their complexes due to the σ-donating and π-accepting abilities of the phosphine donor. DuBois *et al.,* investigated the catalytic activity of a series of Pd complexes, [Pd(PXP)(MeCN)](BF$_4$)$_2$ (PXP = tridentate ligands; P and X denote coordinating atoms, where X = C, N, O, S, P, and As), and found that the introduction of a phosphine donor at the *trans* position to a labile ligand is the key to obtain an active catalyst for CO_2 reduction.[35-37] Thus, the introduction of phosphine donor(s) to Ru-based polypyridyl complexes can be a powerful strategy to control their CO_2 reduction activity. However, there is no study on CO_2 reduction by Ru-based complexes containing a phosphine-substituted polypyridine ligand. In this chapter, I report electrochemical CO_2 reduction by a Ru complex with a mixed phosphine-pyridine ligand, *trans(P,MeCN)*-[Ru^{II}(tpy)(pqn)(MeCN)]$^{2+}$ (**RuP**, where pqn = 8-(diphenylphosphanyl)quinoline,[38-39] Fig. 1, right). Presented here are the catalytic activity of **RuP**, the electronic structures of catalytic intermediates, and a plausible catalytic mechanism. I also discussed the effect of the phosphine donor on the catalytic reaction in comparison with the relevant polypyridyl complex **RuN**.
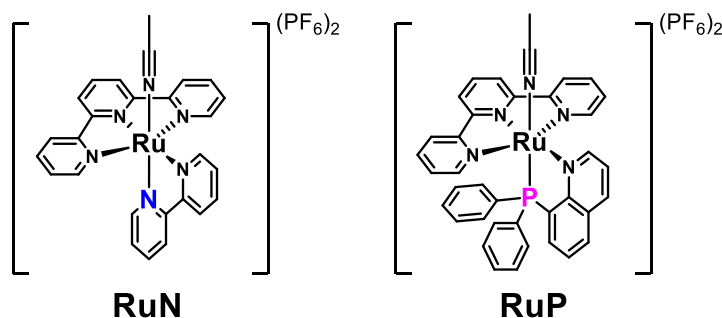

Figure 1: Chemical structures of **RuN** and **RuP**.

Results and discussions

Electrochemistry under Ar

RuP was synthesized and characterized following the procedure reported by our group.[40-41] In a cyclic voltammogram (CV) under an Ar atmosphere, **RuP** displayed one reversible oxidation wave in the positive potential region, attributed to a Ru(III)/Ru(II) redox couple at +0.95 V vs. ferrocene/ferrocenium (Fc/Fc$^+$, Figure 2a, black line). In the negative potential region, one reversible redox wave was observed, and the half-wave potential ($E_{1/2}$) of the wave was -1.72 V (Figure 2b, black line). As reported previously,[41] the wave consists of two reversible one-electron processes with similar redox potentials ($E°'_1 = -1.69$ V and $E°'_2 = -1.78$ V, estimated from a simulation of CV (Figure 3 & Table 1). The details of CV simulation is shown in the experimental section.

To assign the origin of the first reduction process, I calculated the molecular orbitals of **RuP** by density functional theory (DFT) calculations (see the experimental section). The LUMO of **RuP** is localized at the π* orbital of the tpy moiety, suggesting that the first reduction wave at -1.69 V originates from a tpy/tpy$^-$ redox couple (Figure 4). This observation is consistent with the electrochemical properties of the relevant Ru polypyridyl complexes.[21] The peak currents (i_p) corresponding to the redox couples at -1.69 and -1.78 V have linear relationships with the square root of the scan rate ($v^{1/2}$) and follow the Randles-Sevcik equation (Figure 5 & 6 & Table 2). This result indicates that **RuP** can facilitate rapid electron transfer reactions, as frequently observed for Ru polypyridyl complexes.[21-26]
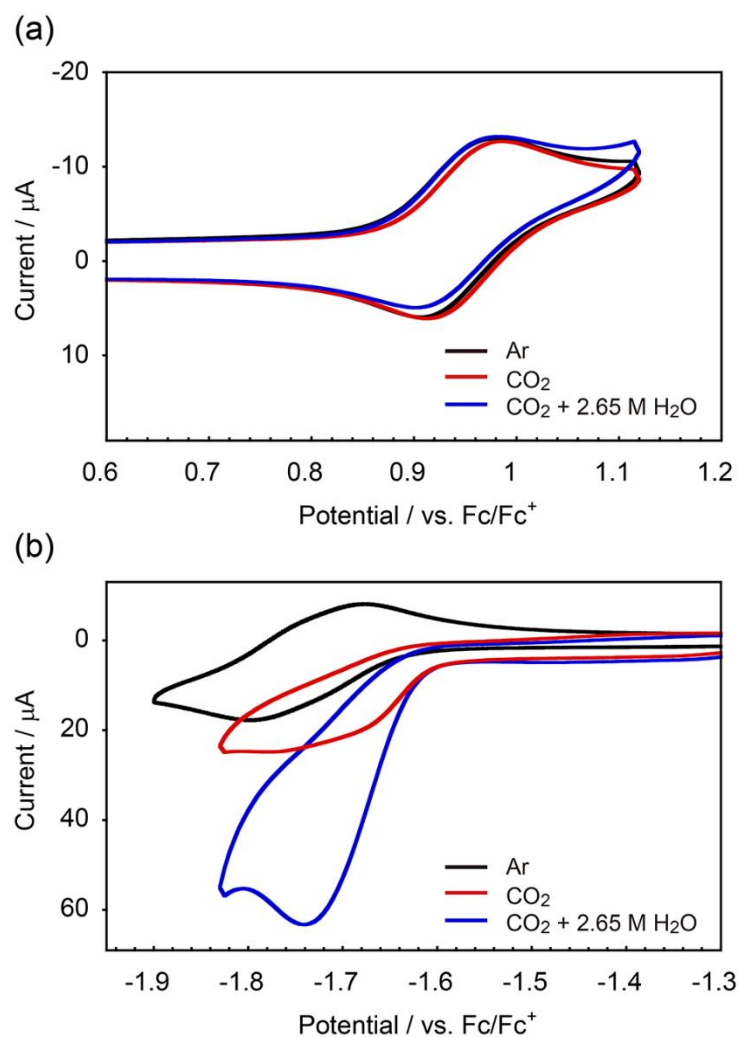
Figure 2: CVs of **RuP** (0.5 mM) in 0.1 M TEAP/MeCN under Ar (black line), CO_2 (0.28 M, red line), and CO_2 in the presence of 2.65 M H_2O (blue line). Working electrode, glassy carbon; counter electrode, Pt wire; reference electrode, Ag/Ag^+; scan rate, $0.1\ Vs^{-1}$. Potential sweeps were started from the open circuit potential (-0.27 V) for all measurements.
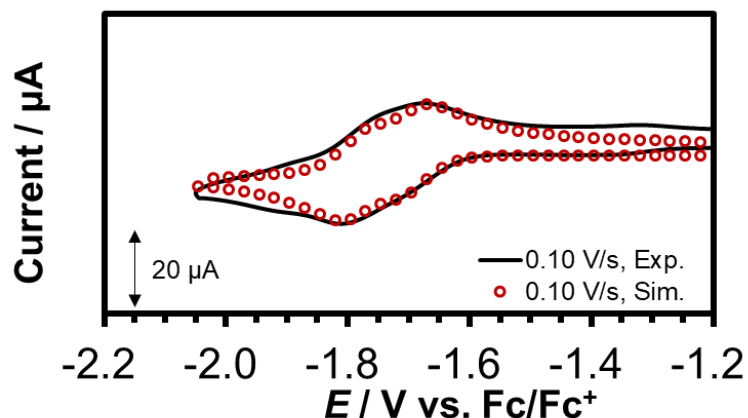
Figure 3: A CV of **RuP** in acetonitrile (black line, [complex] = 0.5 mM; 0.1 M TEAP; WE: GC, CE: Pt wire, RE: Ag/Ag$^+$, scan rate, 0.10 V/s) under Ar, and the simulated CV (red circle). Elchsoft DigiElch 7.FD software was used for simulation of CV to obtain redox potentials of **RuP** as reported previously.[41]

Table 1: Simulation parameters for the CV. Elchsoft DigiElch 7.0. software was used for simulation.

	RuP
Sweep rate [v] (V/s)	0.10
Resistance [R] (Ω)	200
Capacitance [CdI] (F)	7.0×10^{-6}
Temperature [T] (K)	293
Surface area [A] (cm^2)	0.07
Diffusion constant [D] (cm^2/s)	1.0×10^{-5}
Concentration [c] (mol/dm^3)	5.0×10^{-4}
$E^{\circ\prime}_1$ (V)	-1.69
k_{s1} (cm/s)	0.05
α_1	0.50
$E^{\circ\prime}_2$ (V)	-1.78
k_{s2} (cm/s)	0.05
α_2	0.50

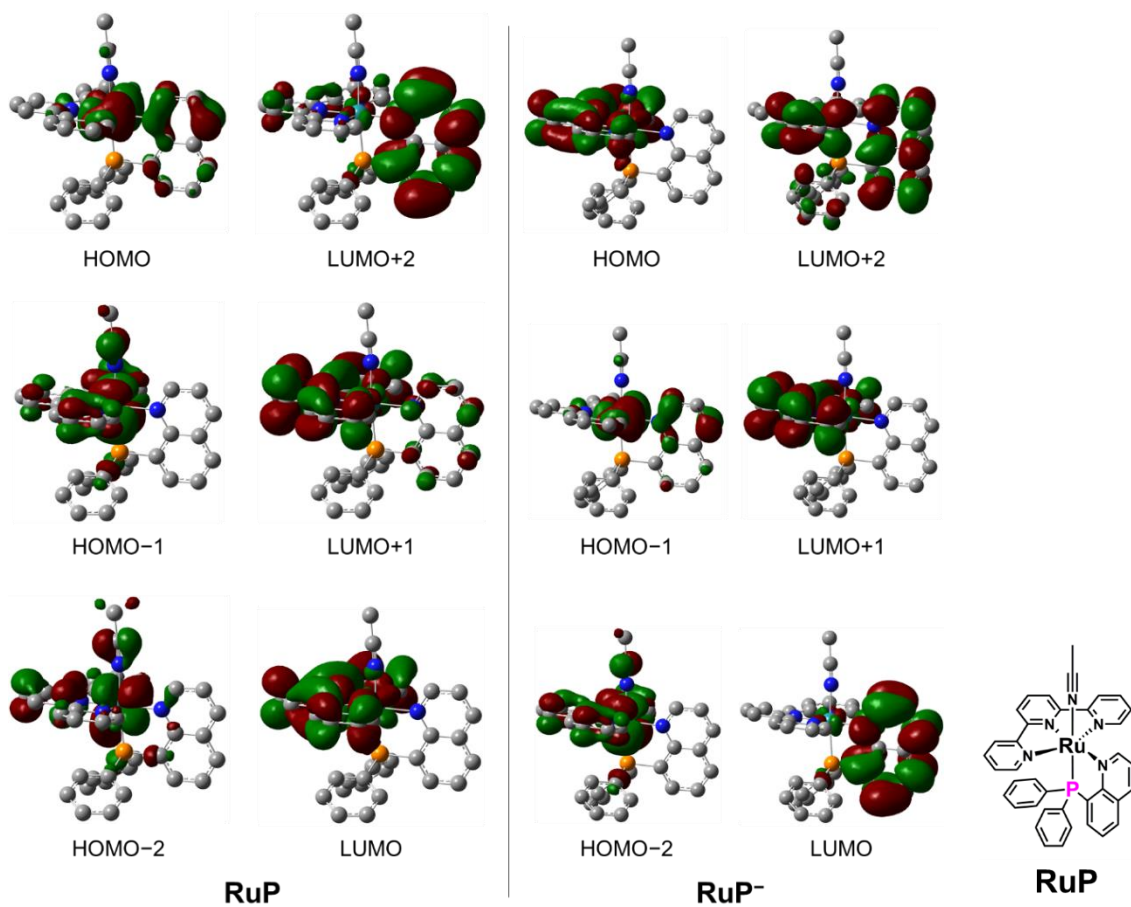$E^{\circ\prime}_1$ and $E^{\circ\prime}_2$ are referred to Fc/Fc$^+$.

Figure 4: Isodensity surface plots of selected frontier molecular orbitals of **RuP** and **RuP⁻** based on the optimized ground-state geometry. The geometric optimization and electronic structures for **RuP** and **RuP⁻** were calculated at the B3LYP/LanL2DZ level and UB3LYP/LanL2DZ level, respectively with the Gaussian 09 program package.
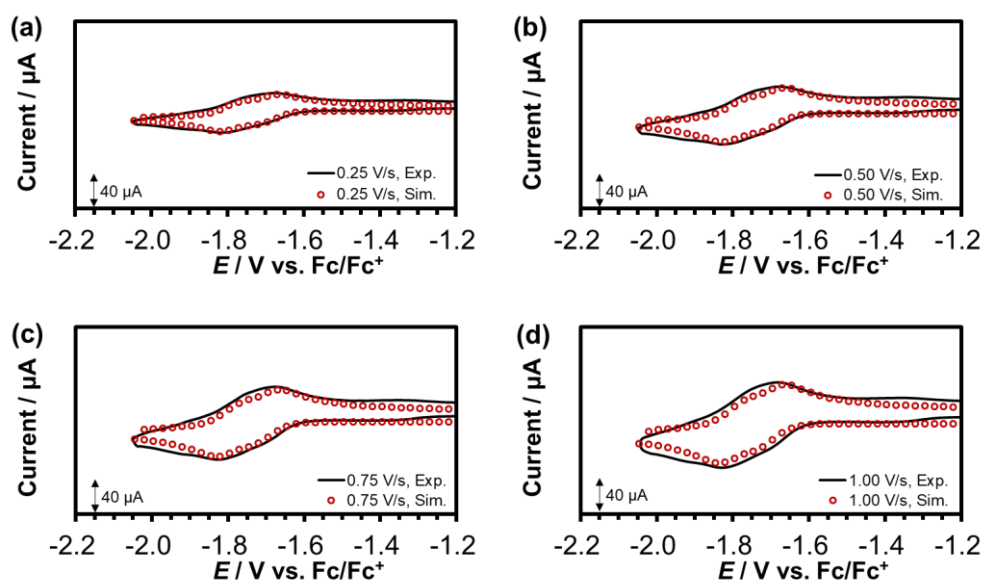
Figure 5: Experimental (black lines) and simulated CVs (red circles) of **RuP** (0.5 mM) in 0.1 M TEAP/MeCN under Ar at various scan rates, (a) = 0.25 V/s, (b) = 0.50 V/s, (c) = 0.75 V/s, (d) = 1.00 V/s. Working electrode, glassy carbon; counter electrode, Pt wire; reference electrode, Ag/Ag$^+$.
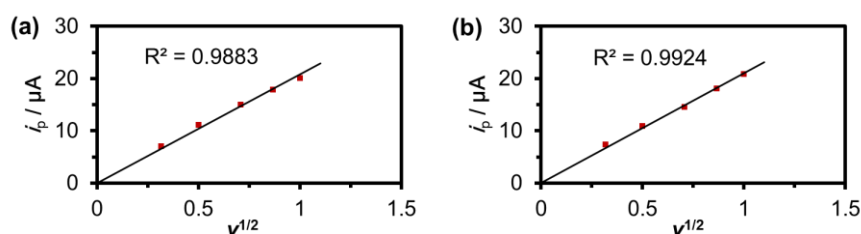

Figure 6: Variation of peak current (i_p) of **RuP** (0.5mM) at the (a) first redox wave and (b) second redox wave versus square root of scan rate. The i_p values were obtained from simulated CVs.

Table 2: Summary of the data used for the i_p vs. $v^{1/2}$ plot.

		First redox wave	Second redox wave
v (V/s)	$v^{1/2}$	i_p (µA)	i_p (µA)
0.10	0.316	7.00	7.41
0.25	0.500	11.13	10.95
0.50	0.707	15.06	14.60
0.75	0.866	17.89	18.05
1.00	1.00	20.13	20.90

Electrochemical CO_2 reduction

To examine the catalytic CO_2 reduction activity of **RuP**, CVs of **RuP** were measured under CO_2 using anhydrous acetonitrile as the solvent. **RuP** exhibited irreversible reduction waves at E_{pc} = −1.67 and −1.76 V (Figure 2b, red line). These reduction occurred at a more positive potential than those under Ar (Figure 7). I also performed controlled-potential electrolysis (CPE) at −1.70V, and almost negligible amount of CO (faradaic efficiency (FE) < 1.0 %) was detected.

Similar measurements were subsequently performed using acetonitrile containing 2.65 M H_2O as a weak Brønsted acid as the solvent. In this condition, current enhancement was observed near E_{pc} = −1.73 V (Figure 2b, blue line), and the intensity of the current was dependent on the concentrations of CO_2 and H_2O (Figure 8). In CPE conducted at −1.70 V, approximately 1.75 C of charge passed during 1 h of electrolysis (Figure 9 & Table 3, Entry 1), and the formation of CO (5.1 µmol, FE: 55.8%), HCOOH (0.6 µmol, FE: 6.6%), and a negligible amount of H_2 (0.04 µmol, FE: 0.5%) was confirmed. These results clearly indicate that **RuP** can promote electrochemical CO_2 reduction in the presence of H_2O.

I also calculated the overpotential of **RuP** for CO_2 reduction to be 0.4 V based on the potential at half of the catalytic current ($E_{cat/2}$ = −1.65 V).[25,42] The value is substantially lower than those of the relevant polypyridyl complexes including **RuN** (Table 4).[21-22] The turnover frequency (TOF) and the turnover number (TON) for CO production were determined to be 4.7 s^{-1} and 1.7 x 10^4, respectively (see the experimental section).

Details of the reactions of **RuP** under CO_2 were investigated under anhydrous conditions, where the catalytic reaction does not proceed (*vide supra*). When the concentration of CO_2 was increased, the first reduction peak gradually became irreversible, and the position of cathodic peak shifted to more positive potentials (Figure 7). This result indicates that CO_2 and the one-electron reduced state of **RuP** (**RuP⁻**) interact. The position of the first reduction peak remained unchanged in the case of **RuN** (Figure 10), which is known to show no interactions with CO_2 in its one-electron reduced state.[21]
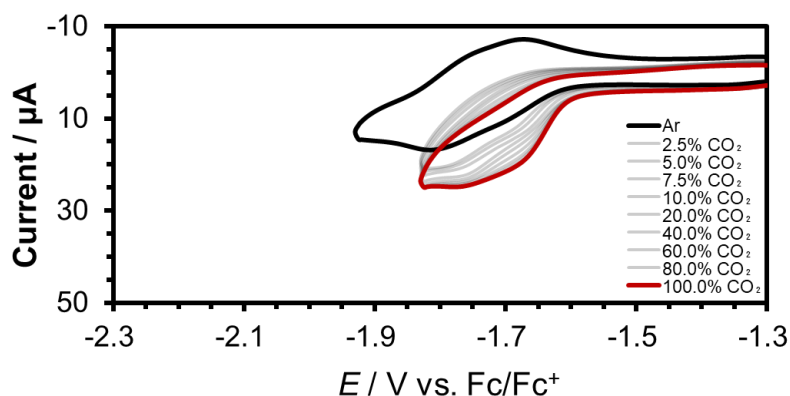
Figure 7: CVs of **RuP** (0.5 mM) in anhydrous 0.1 M TEAP/MeCN under various concentrations of CO_2 (CO_2/Ar, v/v%). Working electrode, glassy carbon; counter electrode, Pt wire; reference electrode, Ag/Ag$^+$; scan rate, 0.1 V/s.
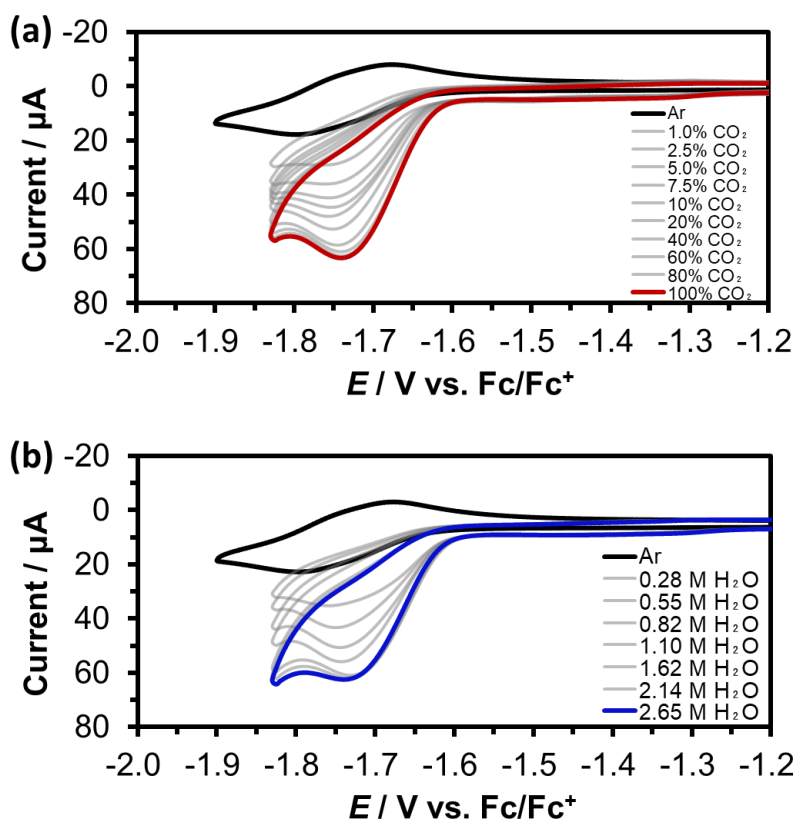

Figure 8: (**a**) CVs of **RuP** (0.5 mM) in 0.1 M TEAP/MeCN under various concentrations of CO_2 (CO_2/Ar, v/v%) in the presence of H_2O (2.65 M). (**b**) CVs of **RuP** (0.5 mM) in 0.1 M TEAP/MeCN at various concentrations of H_2O under CO_2 (0.28 M). Working electrode, glassy carbon; counter electrode, Pt wire; reference electrode, Ag/Ag$^+$; scan rate, 0.1 V/s.
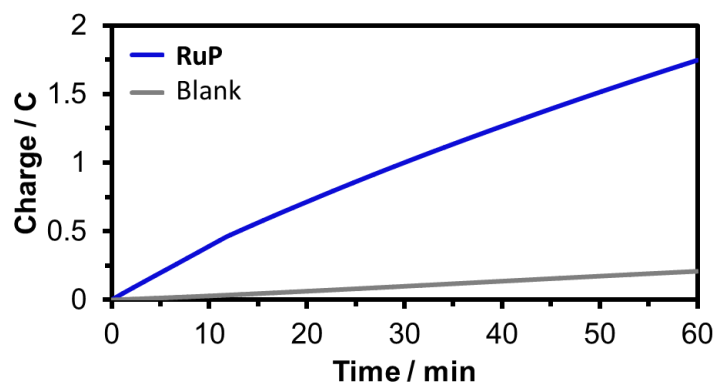
34

Figure 9: The result of controlled-potential electrolysis of **RuP** (0.5 mM) in 0.1 M TEAP/MeCN under CO_2 (0.28 M) at -1.7 V (vs. Fc/Fc$^+$) in the presence of H_2O (2.65 M) for 1 h. Working electrode, glassy carbon (1.2 cm^2); counter electrode, Pt wire; reference electrode, Ag/AgCl. Approximately 1.75 C has been transferred during 1 h of electrolysis.

Table 3: Summary of CPE experiments[a]

Entry	Catalyst	[H_2O], M	Charge, C	Faradaic Efficiency, %[b]		
				CO	HCOOH	H_2
1	**RuP**	2.65	1.75	55.8	6.6	0.5
2	-	2.65	0.15	-	-	-

[a] Conditions: 0.50 mM catalyst, applied voltage: -1.70 V (vs. Fc/Fc$^+$), duration: 1 h.

[b] Further reduced species of CO_2 such as formaldehyde and methanol have not been detected, and the fate of the rest of the charge is not clear at this stage.

Table 4: Overpotentials (η) and operating conditions of selected homogeneous CO_2 reduction electrocatalysts.

Entry Molecule	Solvent	Overpotentials, η (V)	TOF (s^{-1})	Ref.
[Ru(tpy)(pqn)(MeCN)]$^{2+}$ (**RuP**)	MeCN + 2.65 M H_2O	0.40[a,b]	4.7[f]	This work
[Ru(tpy)(bpy)(MeCN)]$^{2+}$ (**RuN**)	MeCN + 2.65 M H_2O	0.60[a,b]	5.1[e]	22
	MeCN	0.87	5.5[e], 38.4[f]	21, 43
[Ru(tpy)(Mebim-py)(MeCN)]$^{2+}$	MeCN	0.81	19[e], 31[f]	21, 43
[Ru(tpy)(bpy)(CO)]$^{2+}$	MeCN	0.50[a, c]	-	44
[Ru(*t*Bu$_3$tpy)(6-mbpy)(MeCN)]$^{2+}$	MeCN	0.47	1.1[e]	25
trans(Cl)-Ru(mesbpy)(CO)$_2$Cl$_2$	MeCN + 0.5 M phenol	0.75 [a,c]	1300[g]	45
[Mn(mesbpy)(CO)$_3$(MeCN)](OTf)	MeCN + 3.2 M MeOH	0.70	2000[g]	46
	MeCN + 120 mM Mg^{2+}	0.30−0.45[d]	20[g]	47
FeTDHPP	DMF + 2 M H_2O	0.41−0.56	3200[f]	43
Fe-*o*-TMA	DMF + 3 M phenol	0.22	100000[f]	48

[a]The overpotentials, η, were calculated using previously reported methods,[42] which is the difference between the standard potential of CO_2/CO couple in a specific solvent system with potential at half the catalytic current ($E_{cat/2}$) of catalyst (Eq. 1).

$$\eta = |E_{CO_2/CO} - E_{cat/2}| \text{ (Eq. 1)}$$

[b]Calculated based on the data shown in Figure 14.

[c]The values of $E_{cat/2}$ were estimated from the CVs reported in the references. For the standard potential of CO_2/CO couple, $E°_{CO_2/CO, MeCN} = -1.25$ V vs. Fc/Fc$^+$ or $E°_{CO_2/CO, DMF} = -1.30$ V vs. Fc/Fc$^+$ was used.[43]

[d]$E°_{CO_2}$ for $2CO_2 + Mg^{2+} \rightarrow CO + MgCO_3$ was estimated between −1.15 V to −1.30 V vs. Fc/Fc$^+$.[47]

[e]The value is calculated based on results of CV as reported in ref. 21.

[f]The value is calculated based on results of controlled potential electrolysis as reported in ref. 43.

[g]The value is calculated based on results of CV as reported in ref. 46.
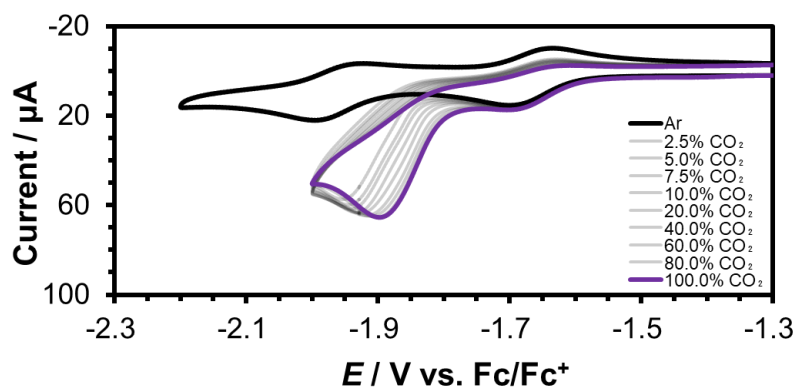
Figure 10: CVs of **RuN** (0.5 mM, open circuit = −0.27 V) in 0.1 M TEAP/MeCN under various concentrations of CO_2 (CO_2/Ar, v/v%) in the absence of H_2O. Working electrode, glassy carbon; counter electrode, Pt wire; reference electrode, Ag/Ag$^+$; scan rate, 0.1 V/s.

UV-Vis spectroelectrochemical measurement under Ar and CO$_2$

The reactions were also monitored by UV-vis spectro-electrochemical measurements. At the open circuit potential ($E = -0.27$ V), **RuP** exhibits an absorption band centred at 436 nm, which is attributed to a metal-to-ligand charge transfer (MLCT) transition (Figure 11). The UV-vis absorption spectra under Ar and CO$_2$ were almost identical at this potential, indicating that **RuP** does not interact with CO$_2$ before the electrochemical reaction proceeds.

By scanning the potential to the negative potential region, distinct spectral changes under Ar and CO$_2$ were observed. Under Ar, the MLCT band redshifted from 436 to 475 nm with isosbestic points (Figure 12) due to the reduction at tpy moiety.[49] Under CO$_2$, the MLCT band initially shifted from 436 to 460 nm (from open circuit potential to -1.60 V, Figure 13), followed by a blueshift to 440 nm (from -1.60 to -1.70 V). These results suggest that **RuP$^-$**, formed after one-electron reduction of **RuP**, rapidly reacts with CO$_2$ and that the generated CO$_2$-bound species is further reduced at around -1.65 V.
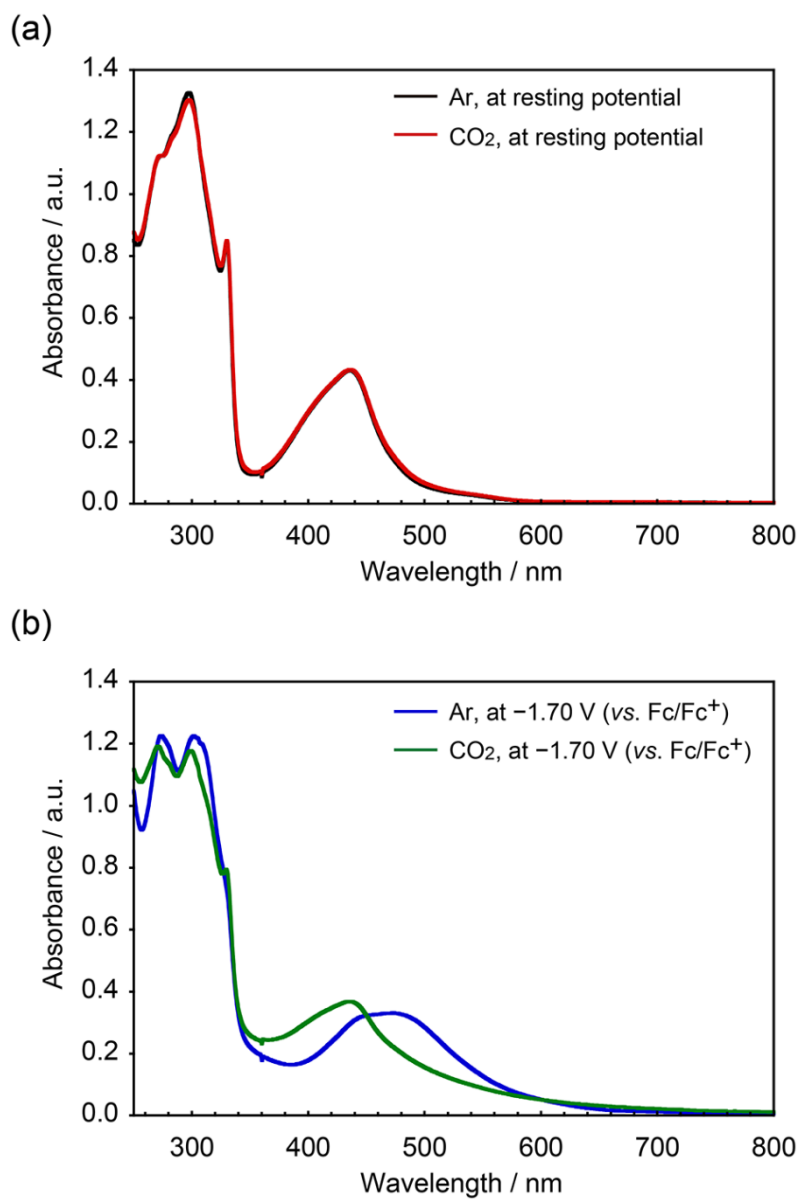
Figure 11: UV-Vis absorption spectra of **RuP** (0.5 mM) at open circuit potential in 0.1 M TEAP/MeCN under Ar and CO_2. (**b**) UV-Vis absorption spectra of **RuP** (0.5 mM) under open circuit potential and at -1.70 V vs. Fc/Fc$^+$ in 0.1 M TEAP/MeCN under Ar and CO_2.
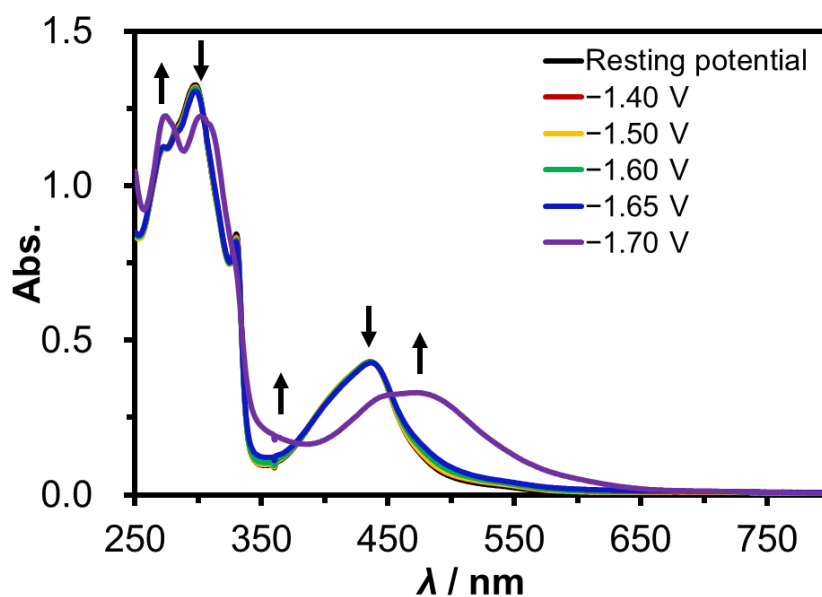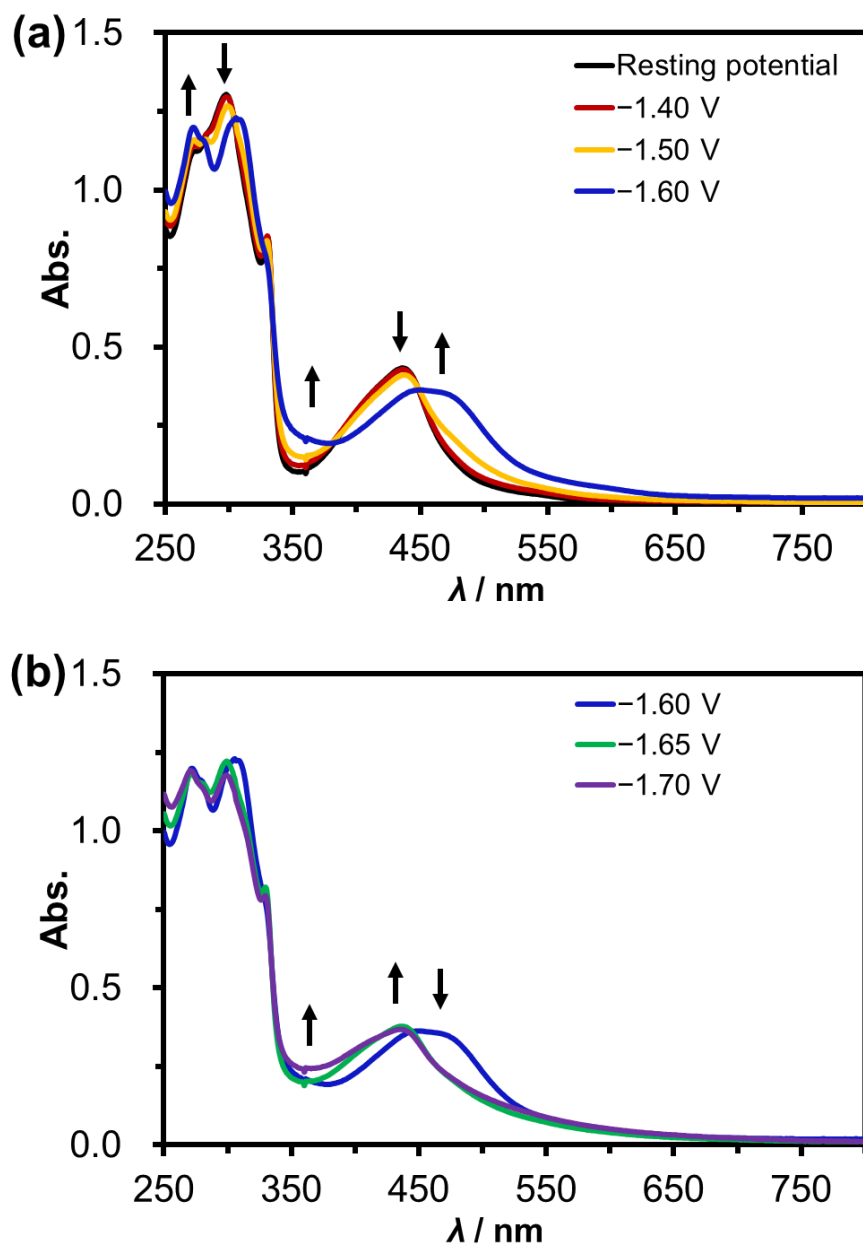
Figure 12: Experimental UV-Vis absorption spectra of **RuP** (0.5 mM) at various applied potentials in 0.1 M TEAP/MeCN under Ar using BASi Spectro-electrochemical Cell (open-circuit potential = −0.27 V). Working electrode, Pt mesh; counter electrode, Pt wire; reference electrode, Ag/Ag$^+$. Solutions were purged with Ar for 10 mins prior to measurements. Weak Ar flow was maintained throughout the measurement. Spectra were acquired after electrolysis at respective potentials for 8 mins.

Figure 13: Experimental UV-Vis absorption spectra of **RuP** (0.5 mM) at various applied potentials in 0.1 M TEAP/MeCN under CO_2. (a) Resting potential to -1.60 V and (b) -1.60 V to -1.70 V. Working electrode, Pt mesh; counter electrode, Pt wire; reference electrode, Ag/Ag$^+$. Spectra were acquired after electrolysis at respective potentials for 8 mins.

Proposed mechanism for CO₂ binding by RuP and RuN

The aforementioned reactivity of **RuP** with CO_2 under reductive conditions is completely different from that of **RuN**.[21-22] The **RuN** complex initially undergoes two one-electron reductions at the tpy and bpy ligands, and a two-electron reduced species, $[Ru^{II}(tpy^-)(bpy^-)(MeCN)]^0$ (**RuN^{2-}**), forms at near -1.85 V. **RuN^{2-}** undergoes an exchange between the MeCN ligand and a CO_2 molecule to generate the metallocarboxylate intermediate $[Ru^{II}(tpy)(bpy)(CO_2^{2-})]^0$ (**RuN$_{CO_2}^{2-}$**, Scheme 1, top, EEC mechanism, where E and C indicate electron transfer and chemical reactions, respectively). In other words, **RuN** cannot react with CO_2 before $2e^-$ reduction, and thus, the electrocatalytic CO_2 reduction can proceed only after the second reduction.[21-22] In contrast, one-electron reduced species of **RuP** (**RuP$^-$**) can react with CO_2 (EC mechanism, *vide supra*) and be further reduced to generate the catalytic active intermediate near -1.65 V, resulting in **RuP** mediating CO_2 reduction at a lower overpotential than **RuN** (Figure 14).
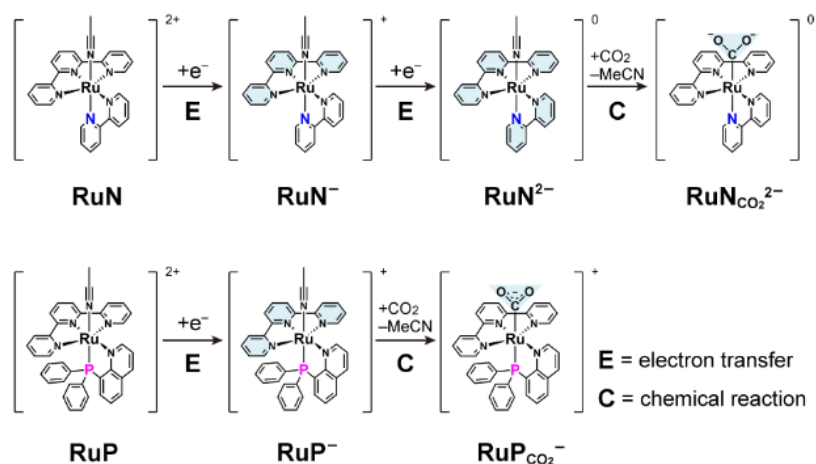
Scheme 1: Proposed mechanism for the formation of metallocarboxylate intermediate of **RuN** via EEC mechanism (top) and that for **RuP** via EC mechanism (bottom). **E** indicates electron transfer while **C** indicates chemical reaction. Reduced ligands are highlighted with pale blue.
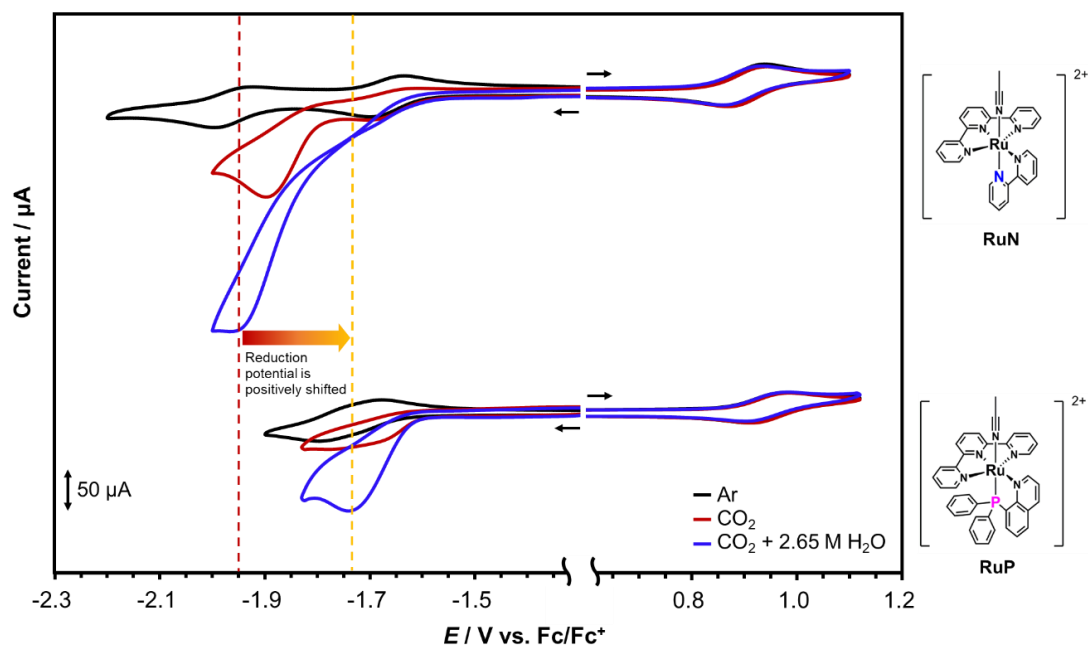
Figure 14: CVs of 0.5 mM of **RuN** (top) and **RuP** (bottom) in 0.1 M TEAP/MeCN under Ar (black line), CO_2 (0.28 M, red line), and CO_2 in the presence of 2.65 M H_2O (blue line). Working electrode, glassy carbon; counter electrode, Pt wire; reference electrode, Ag/Ag$^+$; scan rate, 0.1 V/s. Potential sweeps were started from the open circuit potential (−0.26 V for **RuN**, −0.27 V for **RuP**). Arrows represent the direction of potential sweeping. In the presence of H_2O, the current enhancement was observed at $E_{pc} = -1.95$ V for **RuN** and $E_{pc} = -1.73$ V for **RuP**, which attributed to the electrocatalytic CO_2 reduction.

Crystal structure analyses between RuP and RuN

This superior reactivity of **RuP** with CO_2 can be explained by considering the nature of the coordinating phosphine donor. First, the σ-donating character of the phosphine group can destabilize the bond between the Ru centre and the nitrogen atom of the MeCN ligand (*trans* influence). The previously reported crystal structures of **RuP** and **RuN** clearly demonstrate that the bond between the Ru centre and the nitrogen atom of the MeCN is significantly elongated upon the introduction of a phosphine donor at the position *trans* to the MeCN: 2.127(5) Å[40] for **RuP** and 2.030(1) Å[50] for **RuN** as shown below (Figure 15). Second, the π-accepting character of the phosphine group can stabilize the bond between the Ru centre and the carbon atom of CO_2.
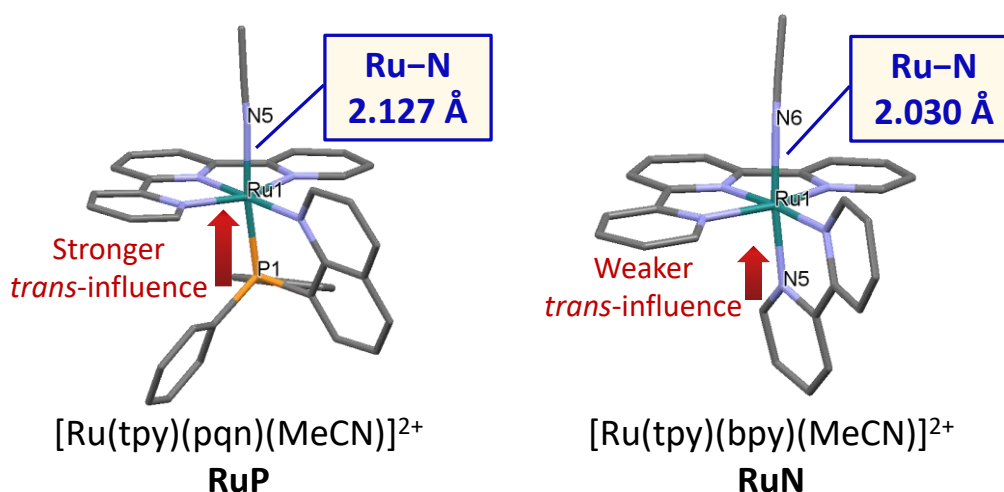

Figure 15: Comparison of crystal structures between **RuP** and **RuN**.

DFT calculations for the CO₂ adduct, RuP$_{CO_2}{}^-$

DFT calculations revealed that the HOMO of the CO_2 adduct formed after one-electron reduction of **RuP** (**RuP$_{CO_2}{}^-$**) is mainly located on the metal-bound CO_2, whereas the HOMO of **RuP⁻** is localized on the tpy ligand (Figure 16). These results indicate that the intramolecular electron transfer from the tpy moiety to the CO_2 proceeds upon the exchange of the MeCN ligand. In other words, the electronic structure of **RuP$_{CO_2}{}^-$** can be best described as $[Ru^{II}(tpy)(pqn)(CO_2{}^{\bullet-})]^+$ (Scheme 1, bottom). The HOMO of **RuP$_{CO_2}{}^-$** is also located on the phosphine donor of the pqn ligand, indicating that the phosphine donor of the pqn ligand contributes to the stabilization of the $Ru-C(CO_2{}^{\bullet-})$ bond of **RuP$_{CO_2}{}^-$** via π-back donation.

HOMO of **RuP⁻**   HOMO of **RuP$_{CO_2}{}^-$**   LUMO of **RuP$_{CO_2}{}^-$**
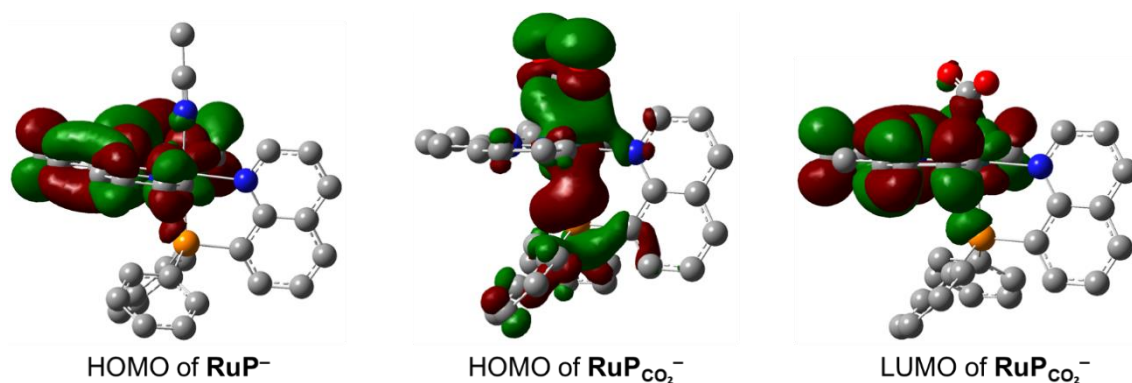
Figure 16: HOMO of the one-electron reduced species, **RuP⁻** (left) and HOMO–LUMO of one-electron reduced **RuP** with a CO_2 molecule bound to the Ru center, **RuP$_{CO_2}{}^-$** (middle & right) based on the optimized ground-state geometry. DFT calculations were performed using the UB3LYP functional and LanL2DZ basis set.

Effect of phosphine ligand for CO_2 binding

The effect of the phosphine donor was further confirmed by electrochemical measurements in a non-coordinating solvent, γ-butyrolactone. The CV of **RuP** under Ar exhibits irreversible reduction waves at $E_{pc} = -1.64$ and -1.81 V (Figure 17a). Upon addition of MeCN to the solution, these waves gradually disappeared, and one quasi-reversible wave was observed at $E_{1/2} = -1.75$ V (Figure 17b). In contrast, the CVs of **RuN** did not change upon the addition of MeCN (Figure 18). These observations suggest that the MeCN ligand easily dissociates from the Ru centre after the first one-electron reduction step in the case of **RuP**.

Moreover, under CO_2, the first reduction wave of **RuN** remained unchanged (Figure 19a), whereas the reduction wave of **RuP** was positively shifted to $E_{pc} = -1.55$ V (Figure 19b), supporting the idea that CO_2 can easily bind **RuP⁻**. These results are fully consistent with the consideration that phosphine donor of **RuP** contributes to the destabilization of the Ru-N(MeCN) bond via σ-donation and the stabilization of the Ru-C($CO_2^{\bullet-}$) bond via π-back donation.
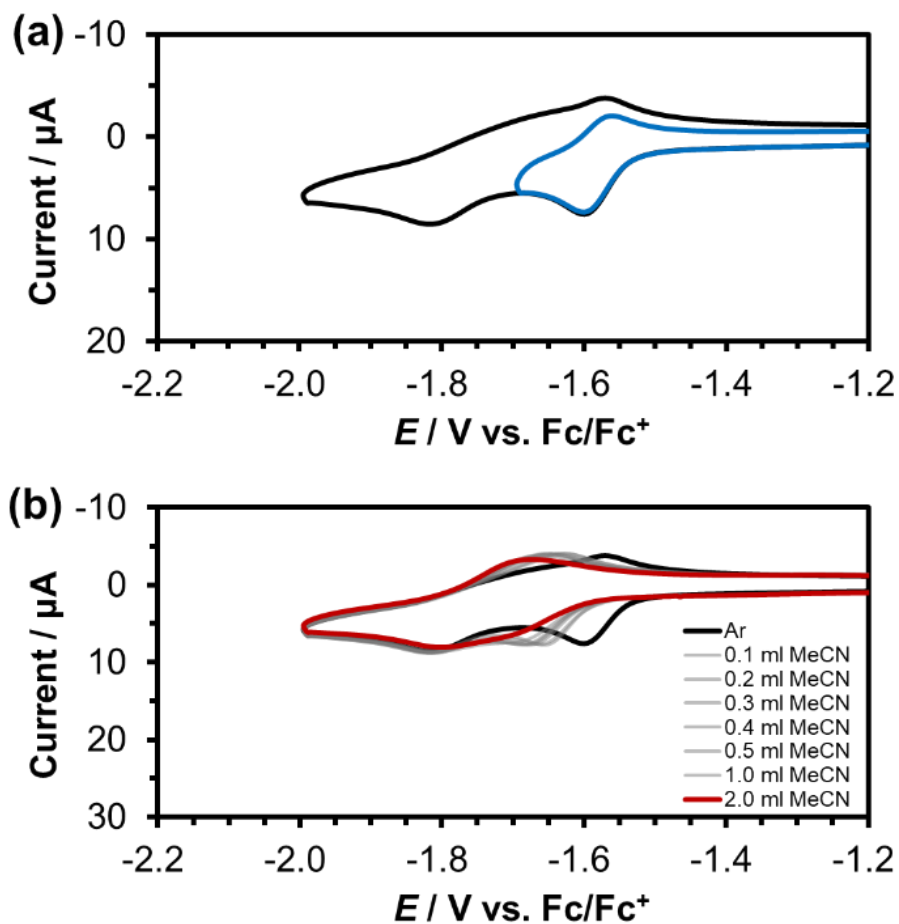
Figure 17: (a) CV of **RuP** (0.5 mM) in 0.1 M TEAP/γ-butyrolactone under Ar at different potential scan range. (b) CV of **RuP** (0.5 mM) in 0.1 M TEAP/γ-butyrolactone under Ar added with various amount of MeCN. Working electrode, glassy carbon; counter electrode, Pt wire; reference electrode, Ag/Ag$^+$; scan rate, 0.1 V/s.
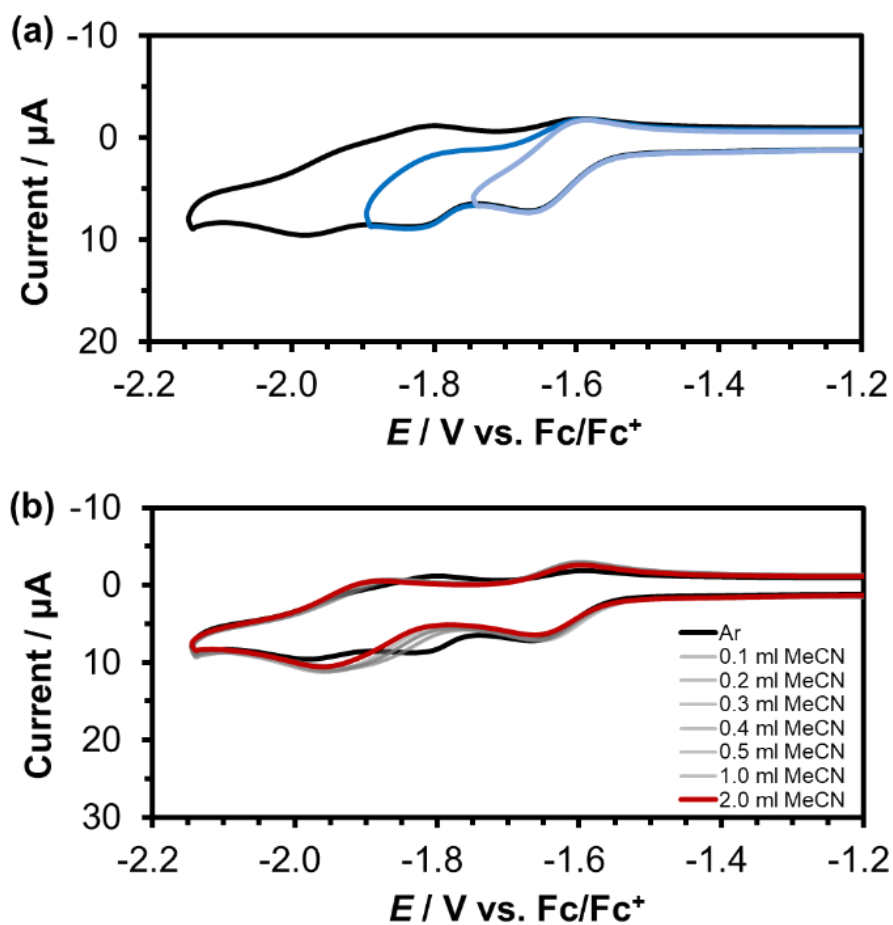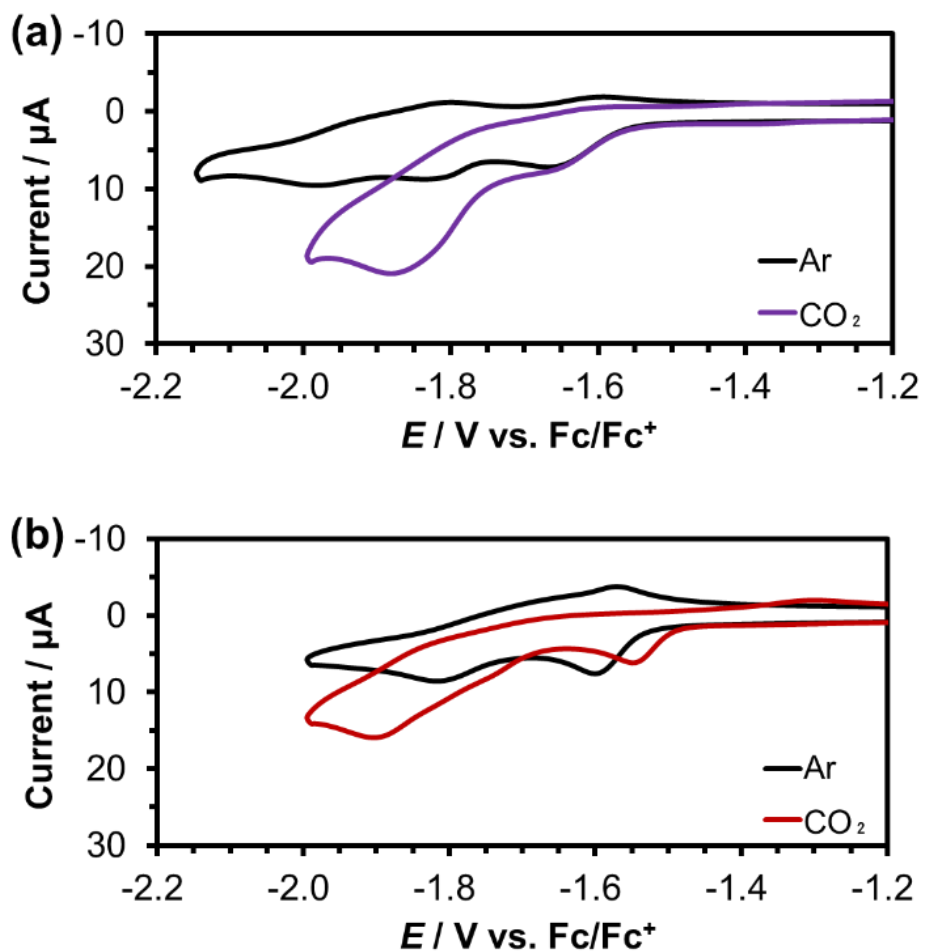
Figure 18: (a) CV of **RuN** (0.5 mM) in 0.1 M TEAP/γ-butyrolactone under Ar at different potential scan range. (b) CV of **RuN** (0.5 mM) in 0.1 M TEAP/γ-butyrolactone under Ar added with various amount of MeCN. Working electrode, glassy carbon; counter electrode, Pt wire; reference electrode, Ag/Ag$^+$; scan rate, 0.1 V/s.

Figure 19: (a) CVs of **RuN** (0.5mM) in 0.1 M TEAP/γ-butyrolactone under CO_2. (b) CVs of **RuP** (0.5 mM) in 0.1 M TEAP/γ-butyrolactone under CO_2. Working electrode, glassy carbon; counter electrode, Pt wire; reference electrode, Ag/Ag$^+$; scan rate, 0.1 V/s.

Proposed mechanism for electrocatalytic CO_2 reduction

Based on these results, I propose a plausible reaction mechanism of CO_2 reduction catalysed by **RuP** as depicted in Scheme 2. First, a one-electron reduction of **RuP** occurs at the tpy ligand, and the ligand exchange between the MeCN ligand and CO_2 then proceeds (EC mechanism); simultaneous intramolecular electron transfer from the tpy moiety to the coordinated CO_2 affords the key catalytic intermediate, $[Ru^{II}(tpy)(pqn)(CO_2^{\bullet-})]^+$ (**RuP$_{CO_2}$$^-$**). This charge redistribution enables a further one-electron accommodation on the tpy moiety of **RuP$_{CO_2}$$^-$** to generate $[Ru^{II}(tpy^-)(pqn)(CO_2^{\bullet-})]^0$ (**RuP$_{CO_2}$$^{2-}$**).[25] This consideration was supported by DFT calculations on **RuP$_{CO_2}$$^-$**, which indicated that the LUMO is mainly located on the tpy ligand (Figure 16). It should be noted that the further reduction of **RuP$_{CO_2}$$^{2-}$** cannot proceed under anhydrous conditions. However, in the presence of H_2O, a protonation reaction occurs to produce the hydroxycarbonyl intermediate, $[Ru^{II}(tpy^-)(pqn)(CO_2H)]^+$. Further protonation and dehydration of $[Ru^{II}(tpy^-)(pqn)(CO_2H)]^+$ afford the CO-coordinated species, $[Ru^{II}(tpy)(pqn)(CO)]^{2+}$.[16,23] The obtained $[Ru^{II}(tpy)(pqn)(CO)]^{2+}$ is easily reduced at a given potential,[44] the subsequent ligand exchange between the coordinated CO and CO_2 regenerates **RuP$_{CO_2}$$^-$**, and CO is obtained as the major product of the catalytic reaction.
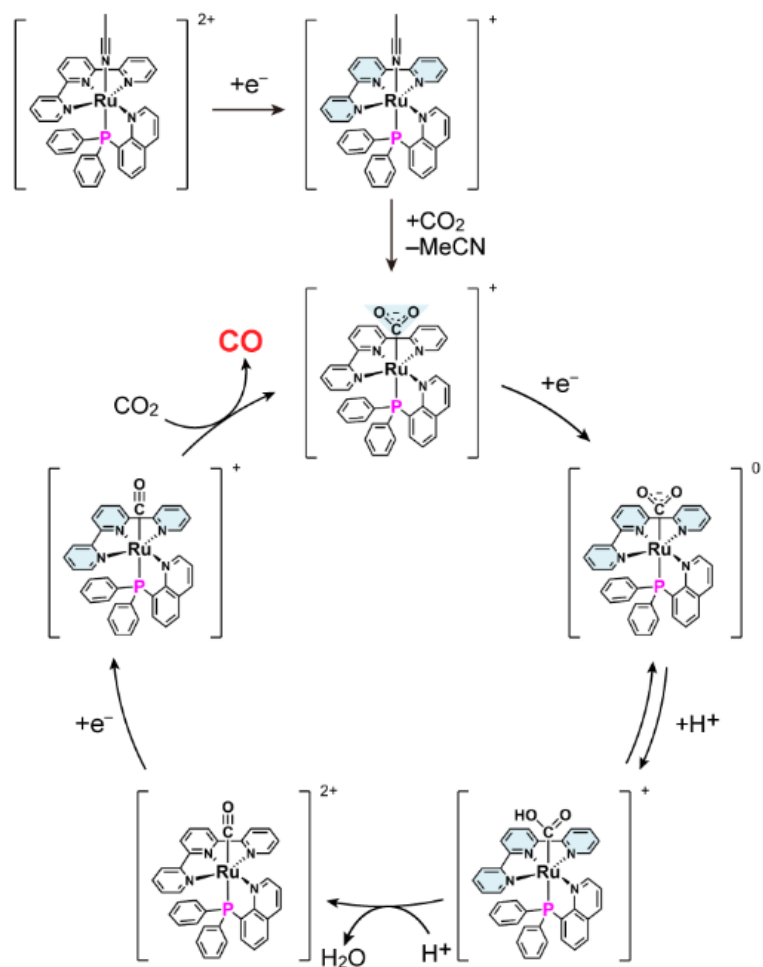
Scheme 2: Proposed reaction mechanism for the electrochemical CO_2 reduction by **RuP** in the presence of the weak Brønsted acid, H_2O. Reduced ligands are highlighted with pale blue.

Conclusion

In summary, I have shown that **RuP** can promote electrocatalytic CO_2 reduction to produce CO with a low-overpotential. The results of electrochemical and spectro-electrochemical measurements and quantum chemical calculations suggested that the phosphine donor destabilizes the bond between the Ru centre and the nitrogen atom of the MeCN ligand via σ-donation (*trans* influence) and stabilizes the bond between the Ru centre and the carbon atom of the coordinated CO_2 molecule via π-back donation. As a result, **RuP** can react with CO_2 upon one-electron reduction to form the key intermediate, $[Ru^{II}(tpy)(pqn)(CO_2^{\bullet-})]^+$ (**RuP**$_{CO_2}^-$), via an EC mechanism. Recently, Ott *et al.*, also reported that the catalyst that can undergo EC reaction can promote CO_2 reduction at a low overpotential.[25] In their study, the steric effect of the bulky substituents embedded in the ligand is the key to induce the EC reaction.[26] It is also reported that the introduction of cationic substituents,[48] and the addition of Lewis acid[47] can reduce the overpotentials. In the current study, a simple introduction of a phosphine moiety to the ligand largely affect the reactivity of the Ru centre, which collectively allow **RuP** to reduce CO_2 with low overpotentials. The present work provides a novel versatile strategy to reduce the overpotential of molecular catalysts for CO_2 reduction, which is possibly applicable to a wide variety of catalytic systems.

Experimental details

General procedures

All the solvents were purchased from Wako Pure Chemical Industries, while the chemicals were purchased from Sigma-Aldrich Co. All the reagents were of highest quality available and were used as received. ^{1}H-NMR, and ^{31}P-NMR spectra were collected at room temperature on a JEOL JNM-ECS400 spectrometer. UV-vis absorption spectra were measured on a Shimadzu UV-2450SIM spectrophotometer at room temperature. Elemental analyses were performed on a J-Science Lab Micro Corder JM10 elemental analyzer. ESI-TOF MS spectra were collected on a JEOL JMS-T100LC mass spectrometer.

Syntheses

8-(diphenylphosphanyl)quinoline (pqn) was synthesized according to literature procedures.[38] ^{1}H NMR (CDCl$_3$): δ 7.12 (m, 1 H), 7.30 (m, 10 H), 7.43 (m, 2 H), 7.81 (d, 1 H), 8.16 (d, 1 H), 8.87 (dd, 1 H). ^{31}P{^{1}H} NMR (CDCl$_3$): δ −14.32 (s). Anal. Found: C, 78.52; H, 5.36; N, 4.16. Calculated for C$_{21}$H$_{16}$NP·0.5H$_2$O (pqn·0.5 H$_2$O): C, 78.25; H, 5.32; N, 4.35.

trans(P,MeCN)-[Ru^{II}(tpy)(pqn)(MeCN)](PF$_6$)$_2$ (**RuP**) was synthesized according to literature procedures.[41] ESI-TOF MS (positive ion, acetonitrile): m/z 324.1 ([Ru(tpy)(pqn)]$^{2+}$), 344.6 ([Ru(tpy)(pqn)(MeCN)]$^{2+}$). ^{1}H NMR (CD$_3$CN): δ 6.56 (t, 4 H), 6.96 (t, 4 H), 7.12 (d, 2 H), 7.21 (t, 2 H), 7.55 (t, 2 H), 7.81 (t, 2 H), 7.93 (m, 3 H), 8.04 (d, 2 H), 8.21 (t, 1 H), 8.29 (d, 2 H), 8,50 (d, 1 H), 8,81 (d, 1 H), 9.83 (d, 1 H). ^{31}P{^{1}H} NMR (CD$_3$CN): δ 58.74 (s). Anal. Found: C, 46.02; H, 3.35; N, 7.18. Calculated for C$_{38}$H$_{30}$N$_5$P$_3$F$_{12}$Ru·0.5H$_2$O (**RuP**·0.5 H$_2$O): C, 46.21; H, 3.16; N, 7.09.

[Ru^{II}(tpy)(bpy)(MeCN)](PF$_6$)$_2$ (**RuN**) was synthesized according to literature procedures.[51] ESI-TOF MS (positive ion, acetonitrile): m/z 266.0 ([Ru(tpy)(bpy)(MeCN)]$^{2+}$), 676.9 ([Ru(tpy)(bpy)(MeCN)]$^+$PF$_6$). ^{1}H NMR (CD$_3$CN): δ 7.05 (m, 1 H), 7.26 (d, 1 H), 7.32 (m, 2 H), 7.66 (d, 2 H), 7.78 (t, 1 H), 7.98 (m, 3 H), 8.30 (m, 3 H), 8.40 (d, 2 H), 8,54 (d, 2 H), 8,60 (d, 1 H), 9.58 (d, 1 H). Anal. Found: C, 39.42; H, 2.75; N, 10.24. Calculated for C$_{37}$H$_{22}$N$_6$P$_2$F$_{12}$Ru (**RuN**): C, 39.48; H, 2.70; N, 10.23.

Electrochemistry

Electrochemical experiments were performed at room temperature on a BAS ALS Model 650DKMP electrochemical analyzer in acetonitrile or γ-butyrolactone ([cat.] = 0.5 mM; 0.1 M tetraethylammonium perchlorate (TEAP)). Cyclic voltammetry was performed by using a one-compartment cell with a three-electrode configuration, which consisted of a glassy carbon disk, platinum wire, and Ag/Ag$^+$ electrode (Ag/0.01 M AgNO$_3$) as the working, auxiliary, and reference electrodes, respectively. The glassy carbon disc working electrode was polished using alumina prior to each measurement. The concentration of CO_2 during the measurements was controlled using KOFLOC RK1200M and 8500MC-0-1-1 flowmeters.

UV-vis spectro-electrochemistry

A thin-layer quartz glass cell (light path length 1 mm) was used. A piece of 80 mesh platinum gauze, a platinum wire, and a Ag/Ag$^+$ electrode (Ag/0.01 M AgNO$_3$) were used as the working, auxiliary, and reference electrodes, respectively. All solutions were purged with Ar or saturated with CO_2 (0.28 M) before the measurements. Spectra were obtained after electrolysis at appropriate potentials for 8 mins. UV-vis spectra in the range from 250−800 nm were recorded. The temperature was controlled at 20 ˚C during the measurements, and a weak Ar/CO_2 flow was supplied throughout the experiments. The redox potentials of samples were calibrated against the redox signal for the ferrocene/ferrocenium (Fc/Fc$^+$) couple.

DFT calculations

Geometric optimization and electronic structures were obtained at the B3LYP or UB3LYP functional[52-53] and LanL2DZ basis set[54-55] with the Gaussian 09 program package.[56]

CV simulation

All simulated CVs were calculated using Elchsoft DigiElch 7.0. software. Full details of the parameters used in simulation are listed in Table 1. These parameters were optimized by CV simulation iteratively until the peak potential over the range of scan rates agreed with the experimental data, resulting in the fit displayed in Figure 3, 5 & 6 & Table 2.

Controlled-potential electrolysis

Controlled-potential electrolysis was performed in a gas-tight two-compartment electrochemical cell as in Figure 20. In the first compartment, the carbon rod working electrode (1.2 cm^2 surface area) and a leakless Ag/AgCl reference electrode (Innovative Instruments, Inc.) were immersed in 0.1 M TEAP/MeCN (5 ml) containing the catalyst (0.5 mM) and H$_2$O (2.65 M). In the second compartment, the Pt auxiliary electrode was immersed in 0.1 M TEAP/MeCN (5 ml) containing ferrocene (40 mM) as a sacrificial reductant. The two compartments were separated by an anion exchange membrane (Selemion DSV). The solution was purged vigorously with CO$_2$ for 30 min prior to electrolysis. The electrolysis was performed for 1 h with constant stirring. The amount of CO and H$_2$ produced at the headspace of the cell was quantified by a Shimadzu GC-8A with a TCD detector equipped with a packed column with Molecular Sieve 13X-S 60/80. Additionally, liquid product was quantified by using a Shimadzu LC-20AD with SPD-20A and RID-10A detectors equipped with a Shim-pack SCR102H column. Calibration curves were obtained by sampling known amounts of H$_2$, CO, and HCOOH.
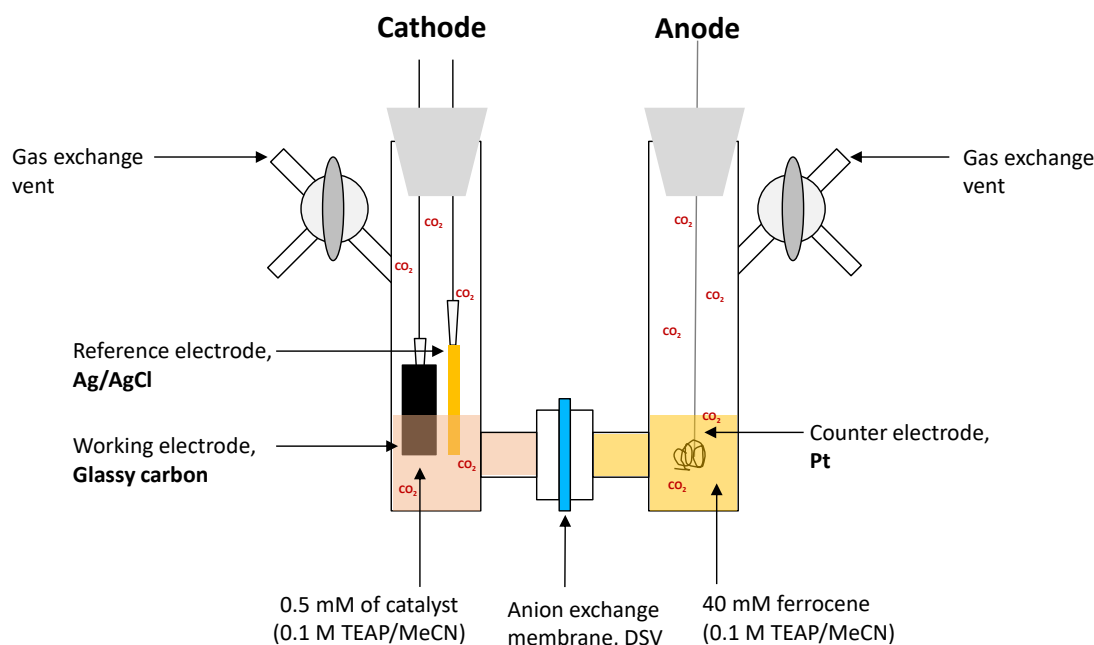
Figure 20: General setup for controlled-potential electrolysis performed in this work.

Estimation of TOF and TON for RuP from controlled-potential electrolysis

$$\frac{i}{FA} = \frac{\sqrt{k_{cat}D}[cat]}{1+\exp\left[\frac{F}{RT}\left(E_{applied}-E_{cat}^{\circ}\right)\right]} \qquad \text{(Eq. 2)}$$

$$\text{TOF} = \frac{k_{cat}}{\left(1+\exp\left[\frac{F}{RT}\left(E_{applied}-E_{cat}^{\circ}\right)\right]\right)} \qquad \text{(Eq. 3)}$$

$$\text{TON} = \frac{k_{cat}t}{\left(1+\exp\left[\frac{F}{RT}\left(E_{applied}-E_{cat}^{\circ}\right)\right]\right)} \qquad \text{(Eq. 4)}$$

The equations were previously adapted by Savéant *et al.* in electrocatalytic CO_2 reduction reaction.[43] By using these formula, the amount of active catalyst is the number of moles contained within the thin reaction-diffusion layer that develops adjacent to the electrode surface.[43] In these equations, i represents stable current transferred during controlled-potential electrolysis, F is Faraday constant (96485 C/mol), A is the surface area of working electrode (1.2 cm^2), k_{cat} is the overall rate constant of the catalytic CO_2 reduction reaction, D is the diffusion coefficient ($\sim 5 \times 10^{-6}$ cm^2/s), [cat] is the concentration of catalyst used (5×10^{-7} mol/cm^3), R is the universal gas constant (8.31 J K^{-1} mol^{-1}), T is temperature (298 K), $E_{applied}$ is the applied potential during electrolysis, E_{cat}° is the standard potential of the catalyst, t is the electrolysis duration, TOF is the turnover frequency, and TON is the turnover number.

The average current density of 0.42 mA/cm^2 (the faradaic efficiency for CO formation is 56 %, corresponds to $i/A = 0.24$ mA/cm^2) was obtained for 1 h electrolysis at −1.70 V vs. Fc/Fc$^+$. Since the electrolysis is performed on the plateau of the catalytic wave, $i/FA = (k_{cat}D)^{1/2}$[cat] (Eq. 2) leading to the TOF = 4.7 s^{-1} and TON = 1.7 x10^4. I also calculated the TON value based on the total cell volume and the value was estimated to be 2 for 1 h. The result indicate the CO_2 reduction reaction mediated by **RuP** is catalytic.

References:

1) A. Goeppert, M. Czaun, J.-P. Jones, G. K. Surya Prakash, G. A. Olah, *Chem. Soc. Rev.* 2014, **43**, 7995-8048.

2) M. Aresta, A. Dibenedetto, *Dalton Trans.* 2007, **28**, 2975-2992.

3) X. Yin, J. R. Moss, *Coord. Chem. Rev.* 1999, **181**, 27-59.

4) M. Rakowski DuBois, D. L. DuBois, *Acc. Chem. Res.* 2009, **42**, 1974-1982.

5) W. Leitner, *Angew. Chem. Int. Ed.* 1995, **34**, 2207-2221.

6) M. Mikkelsen, M. Jørgensen, F. C. Krebs, *Energy Environ. Sci.* 2010, **3**, 43-81.

7) S. Kusama, T. Saito, H. Hashiba, A. Sakai, S. Yotsuhashi, *ACS Catal.* 2017, **7**, 8382-8385.

8) Z. Weng, J. Jiang, Y. Wu, Z. Wu, X. Guo, K. L. Materna, W. Liu, V. S. Batista, G. W. Brudvig, H. Wang, *J. Am. Chem. Soc.* 2016, **138**, 8076-8079.

9) H. Rao, L. C. Schmidt, J. Bonin, M. Robert, *Nature*, 2017, **548**, 74-77.

10) J. Shen, R. Kortlever, R. Kas, Y. Y. Birdja, O. Diaz-Morales, Y. Kwon, I. Ledezma-Yanez, K. J. P. Schouten, G. Mul, M. T. M. Koper, *Nature Comm.* 2015, **6**, 8177.

11) A. M. Appel, J. E. Bercaw, A. B. Bocarsly, H. Dobbek, D. L. DuBois, M. Dupuis, J. G. Ferry, E. Fujita, R. Hille, P. J. A. Kenis, C. A. Kerfeld, R. H. Morris, C. H. F. Peden, A. R. Portis, S. W. Ragsdale, T. B. Rauchfuss, J. N. H. Reek, L. C. Seefeldt, R. K. Thauer, G. L. Waldrop, *Chem. Rev.* 2013, **113**, 6621-6658.

12) J. J. Concepcion, R. L. House, J. M. Papanikolas, T. J. Meyer, *Proc. Natl. Acad. Sci. U.S.A.* 2012, **109**, 15560-15564.

13) E. E. Benson, C. P. Kubiak, A. J. Sathrum, J. M. Smieja, *Chem. Soc. Rev.* 2009, **38**, 89-99.

14) J. Schneider, H. Jia, J. T. Muckerman, E. Fujita, *Chem. Soc. Rev.* 2012, **41**, 2036-2051.

15) P. Kang, Z. Chen, M. Brookhart, T. J. Meyer, *Top. Catal.* 2015, **58**, 30-45.

16) K. Kobayashi, K. Tanaka, *Phys. Chem. Chem. Phys.* 2014, **16**, 2240-2250.

17) C. Costentin, M. Robert, J. M. Savéant, *Chem. Soc. Rev.* 2013, **42**, 2423-2436.

18) Y. Yamazaki, H. Takeda, O. Ishitani, *J. Photochem. Photobiol. C* 2015, **25**, 106-137.

19) Y. Okabe, S. K. Lee, M. Kondo, S. Masaoka, *J. Biol. Inorg. Chem.* 2017, **22**, 713-725.

20) C. Cometto, L. Chen, P. Lo, Z. Guo, K. Lau, E. Anxolabéhère-Mallart, C. Fave, T. Lau, M. Robert, *ACS Catal.* 2018, **8**, 3411-3417.

21) Z. Chen, C. Chen, D. R. Weinberg, P. Kang, J. J. Concepcion, D. P. Harrison, M. S. Brookhart, T. J. Meyer, *Chem. Commun.* 2011, **47**, 12607-12609.

22) Z. Chen, P. Kang, M. T. Zhang, T. J. Meyer, *Chem. Commun.* 2014, **50**, 335-337.

23) H. Ishida, K. Tanaka, T. Tanaka, *Organometallics* 1987, **6**, 181-186.

24) C. W. Machan, M. D. Sampson, C. P. Kubiak, *J. Am. Chem. Soc.* 2015, **137**, 8564-8571.

25) B. A. Johnson, S. Maji, H. Agarwala, T. A. White, E. Mijangos, S. Ott, *Angew. Chem. Int. Ed.* 2016, **55**, 1825-1829.

26) B. A. Johnson, H. Agarwala, T. A. White, E. Mijangos, S. Maji, S. Ott, *Chem. Eur. J.* 2016, **22**, 14870-14880.

27) Z. Chen, J. J. Concepcion, M. K. Brennaman, P. Kang, M. R. Norris, P. G. Hoertz, T. J. Meyer, *Proc. Natl. Acad. Sci. U.S.A.* 2012, **109**, 15606-15611.

28) Y. Tamaki, T. Morimoto, K. Koike, O. Ishitani, *Proc. Natl. Acad. Sci. U.S.A.* 2012, **109**, 15673-15678.

29) Y. Kuramochi, J. Itabashi, K. Fukaya, A. Enomoto, M. Yoshida, H. Ishida, *Chem. Sci.* 2015, **6**, 3063-3074.

30) T. M. Trnka, R. H. Grubbs, *Acc. Chem. Res.* 2001, **34**, 18-29.

31) S. Wesselbaum, T. vom Stein, J. Klankermayer, W. Leitner, *Angew. Chem. Int. Ed.* 2012, **51**, 7499-7502.

32) R. Noyori, *Angew. Chem. Int. Ed.* 2001, **40**, 40-73.

33) P. G. Jessop, T. Ikariya, R. Noyori, *Nature* 1994, **368**, 231-233.

34) S. T. Nguyen, L. K. Johnson, R. H. Grubbs, J. W. Ziller, *J. Am. Chem. Soc.* 1992, **114**, 3974-3975.

35) D. L. DuBois, A. Miedaner, R. C. Haltiwanger, *J. Am. Chem. Soc.*, 1991, **113**, 8753-8764.

36) P. R. Bernatis, A. Miedaner, R. C. Haltiwanger, D. L. DuBois, *Organometallics*, 1994, **13**, 4835-4843.

37) B. D. Steffey, A. Miedaner, M. L. Maciejewski-Farmer, P. R. Bernatis, A. M. Herring, V. S. Allured, V. Carperos, D. L. DuBois, *Organometallics* 1994, **13**, 4844-4855.

38) T. Suzuki, T. Kuchiyama, S. Kishi, H. D. Takagi, M. Kato, *Inorg. Chem.* 2003, **42**, 785-795.

39) T. Suzuki, T. Kuchiyama, S. Kishi, S. Kaizaki, M. Kato, *Bull. Chem. Soc. Jpn.* 2002, **75**, 2433-2439.

40) G. Nakamura, M. Kondo, M. Crisalli, S. K. Lee, A. Shibata, P. C. Ford, S. Masaoka, *Dalton Trans.* 2015, **44**, 17189-17200.

41) G. Nakamura, M. Okamura, M. Yoshida, T. Suzuki, H. D. Takagi, M. Kondo, S. Masaoka, *Inorg. Chem.* 2014, **53**, 7214-7226.

42) A. M. Appel, M. L. Helm, *ACS Catal.* 2014, **4**, 630-633.

43) C. Costentin, S. Drouet, M. Robert, J. M. Savéant, *Science* 2012, **338**, 90-94.

44) H. Nagao, T. Mizukawa, K. Tanaka, *Inorg. Chem.* 1994, **33**, 3415-3420.

45) C. W. Machan, M. D. Sampson, C. P. Kubiak, *J. Am. Chem. Soc.* 2015, **137**, 8564-8571.

46) M. D. Sampson, A. D. Nguyen, K. A. Grice, C. E. Moore, A. L. Rheingold, C. P. Kubiak, *J. Am. Chem. Soc.* 2014, **136**, 5460-5471.

47) M. D. Sampson, C. P. Kubiak, *J. Am. Chem. Soc.* 2016, **138**, 1386-1393.

48) I. Azcarate, C. Costentin, M. Robert, J. M. Savéant, *J. Am. Chem. Soc.* 2016, **138**, 16639-16644.

49) R. M. Berger, D. R. McMillin, *Inorg. Chem.* 1988, **27**, 4245-4249.

50) S. C. Rasmussen, S. E. Ronco, D. A. Mlsna, M. A. Billadeau, W. T. Pennington, J. W. Kolis, J. D. Petersen, *Inorg. Chem.* 1995, **34**, 821-829.

51) K. J. Takeuchi, M. S. Thompson, D. W. Pipes, T. J. Meyer, *Inorg. Chem.* 1984, **23**, 1845-1851.

52) C. Lee, W. Yang, R. G. Parr, *Phys. Rev. B* 1988, **37**, 785-789.

53) A. D. Becke, *J. Chem. Phys.* 1993, **98**, 5648-5652.

54) P. J. Hay, W. R. Wadt, *J. Chem. Phys.* 1985, **82**, 299-310.

55) P. J. Hay, W. R. Wadt, *J. Chem. Phys.* 1985, **82**, 270-283.

56) M. J. Frisch *et al.*, *Gaussian 09 (Revision C.01)*, Gaussian, Inc., Wallingford, CT, 2010.

Chapter 2

Function-integrated Ru catalyst for photochemical CO_2 reduction

Introduction

The efficient conversion of solar energy into storable chemical fuels or useful chemicals is one of the major challenges in the 21st century.[1-4] In particular, visible-light driven photocatalytic reduction of CO_2 has attracted a considerable attention because the technology can not only produce fuels and chemicals but also counteract the emission of CO_2. The reaction is typically achieved by the system using the combination of two distinct metal-complex-based functional units (Two-unit system, Figure 1A); a visible-light absorbing chromophore (photosensitizer, PS) and a catalyst (Cat). So far, the separated[5-9] approach, which composed of PS and Cat molecules, or the connected approach, in which PS and Cat units are assembled into one molecule by the linker[10-14], has been applied to construct the Two-unit system. The system requires photoinduced electron transfer (ET) from PS to Cat to drive the reaction, and the catalysis is largely affected by the efficiency of the ET process.[11-12] Accordingly, the optimization of the ET process with a convergent modification of PS and Cat units is indispensable for the efficient catalytic reaction in the system.

A non-sensitized catalyst, which can act both as PS and Cat, (Integrated system, Figure 1B), is a valuable alternative for photocatalytic CO_2 reduction. This mononuclear metal complex-based system undergoes simultaneous light absorption followed by CO_2 reduction without the ET process. Therefore, the reaction with less component and the ET events than former system can be achieved. After the pioneering discovery of a non-sensitized photocatalyst based on a mononuclear rhenium complex, $Re(I)(bpy)(CO)_3Br$ (bpy = 2,2'-bipyridine), which could reduce CO_2 to CO,[15-18] various approaches have been taken to improve the catalytic activity and extend the absorption of catalysts to visible-light region.[19-20] However, the development of non-sensitized catalysts which have (i) strong absorption in the visible-light region, (ii) high reaction rate, and (iii) high stability is still challenging.
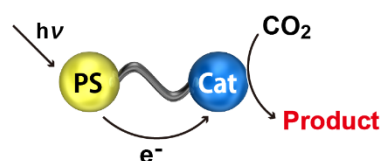
Here, I report an efficient visible-light driven CO_2 reduction catalyzed by a non-sensitized photocatalyst. The key to our success is the employment of a phosphine-substituted Ru(II) polypyridyl complex, *trans(P,MeCN)*-[Ru^{II}(tpy)(pqn)(MeCN)]$^{2+}$ (**RuP**, tpy = 2,2':6',2''-terpyridine; pqn = 8-(diphenylphosphanyl)quinoline,[21-24] Figure 2). **RuP** exhibits an intense MLCT band in the region of 440–475 nm, which was assigned to MLCT transitions,[24] (Figure 3) that is suitable for light harvesting. Additionally, our recent study revealed that the complex catalyzes electrochemical CO_2 reduction at one of the lowest overpotentials among reported homogeneous catalysts.[25] By carefully optimizing the reaction conditions, **RuP** exhibited catalytic performance superior to those of current best-in-class counterparts.
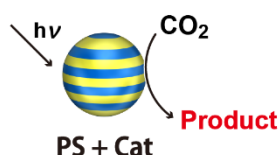
Figure 1: Schematic illustration of three distinct systems for photocatalytic CO_2 reduction; A: Two-unit and B: Integrated systems

RuP
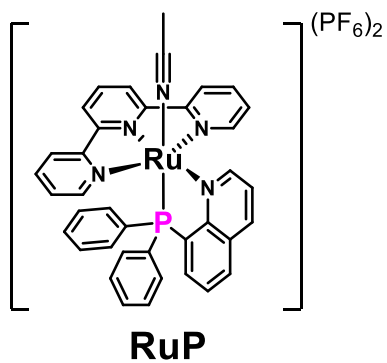
Figure 2: Chemical structure of **RuP**.
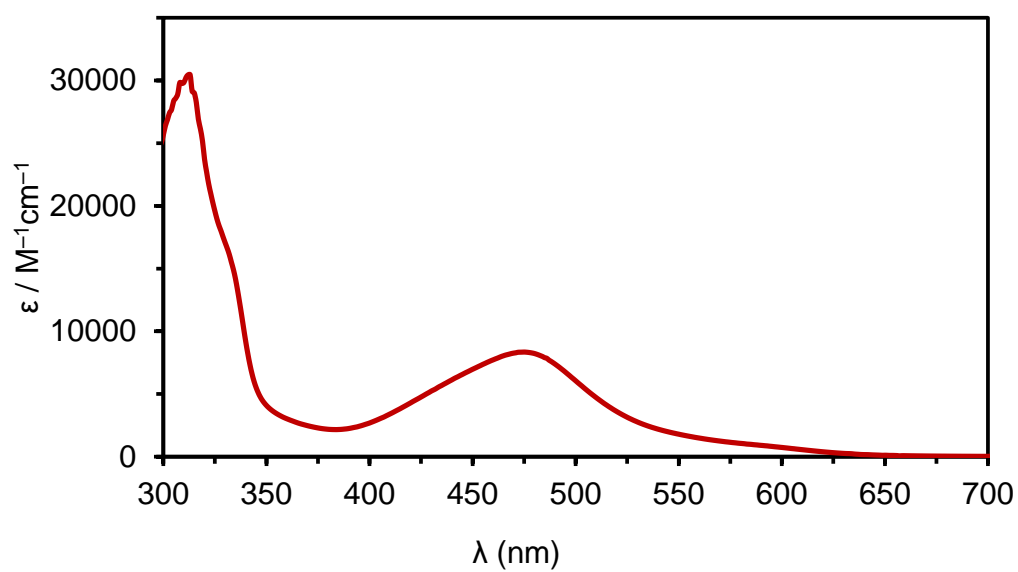
Figure 3: A UV-Vis absorption spectrum of **RuP** in *N*,*N*-dimethylacetamide (DMA).

Results and discussions

Photocatalytic CO$_2$ reduction

Photocatalytic CO$_2$ reduction was conducted under visible-light irradiation (420 $\leq \lambda \leq$ 750 nm) in a CO$_2$-saturated N,N-dimethylacetamide (DMA)/H$_2$O (39:1, v/v) solution containing **RuP** (40 μM) as photocatalyst and 1,3-dimethyl-2-phenyl-2,3-dihydro-1H-benzo[d]imidazole (BIH, 0.1 M) as a sacrificial electron donor.[11] As shown in Figure 4, evolution of CO was observed over 24 h and negligible amounts of H$_2$ and HCOOH were detected. There was no induction period for photocatalytic CO evolution, indicating the instant formation of catalytically active species upon photoirradiation. The TON and TOF of **RuP** for CO production after 4 h of the reaction were 58 (Table 1, entry 1, 94 % selectivity) and 14.5 h^{-1}, respectively. Note that benchmark photocatalyst, Re(I)(bpy)(CO)$_3$Br (bpy = 2,2'-bipyridine),[15-18] exhibited lower TON for CO production (~2) and stability than **RuP** under identical experimental condition (Figure 5). The quantum yield of the reaction was determined to be ϕ_{CO} = 1.7–2.6 % based on the photocatalytic investigation conducted under photoirradiation at 450 nm (Figure 6 & 7).
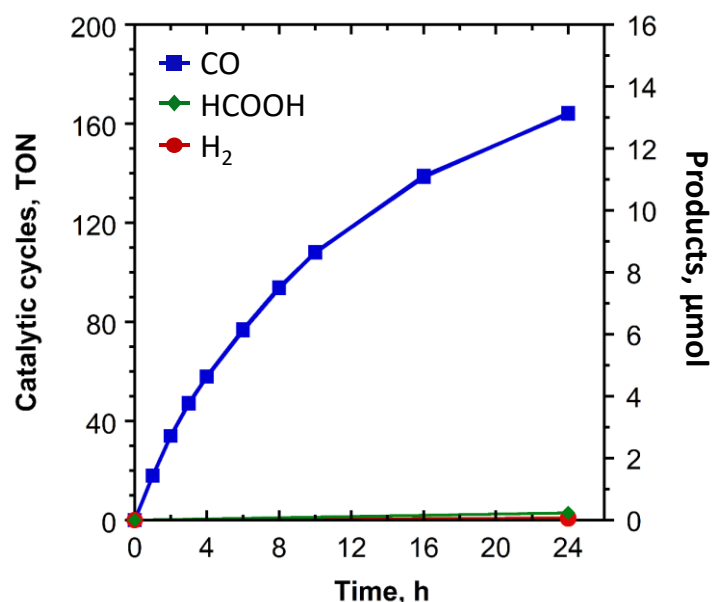
Figure 4: Turnover number of products formed as a function of irradiation time. A CO$_2$-saturated DMA/H$_2$O (39:1, v/v) solution containing 40 μM **RuP** and 0.1 M BIH was irradiated using a Xe lamp equipped with 420 nm long pass filter, producing light in the range of (420 $\leq \lambda \leq$ 750 nm) for 24 h.

Table 1: Control experiments for the photocatalytic CO_2 reduction by **RuP** for 4 h.

No.	[RuP] (μM)	Solvent	Electron donor	λ (nm)	Gas	Turnover numbers (selectivity %)		
						CO	HCOOH	H₂
1	40	DMA/H₂O (39:1, v/v)	BIH	420 ≤ λ ≤ 750 nm	CO₂	58 (94)	3 (5)	1 (1)
2	40	DMA/H₂O (39:1, v/v)	BIH	420 ≤ λ ≤ 750 nm	Ar	-	-	-
3	-	DMA/H₂O (39:1, v/v)	BIH	420 ≤ λ ≤ 750 nm	CO₂	-	-	-
4	40	DMA/H₂O (39:1, v/v)	-	420 ≤ λ ≤ 750 nm	CO₂	-	-	-
5	40	DMA/H₂O (39:1, v/v)	BIH	Dark	CO₂	-	-	-
6	40	DMA/TEOA (4:1, v/v)	TEOA	420 ≤ λ ≤ 750 nm	CO₂	-	14 (> 99)	-
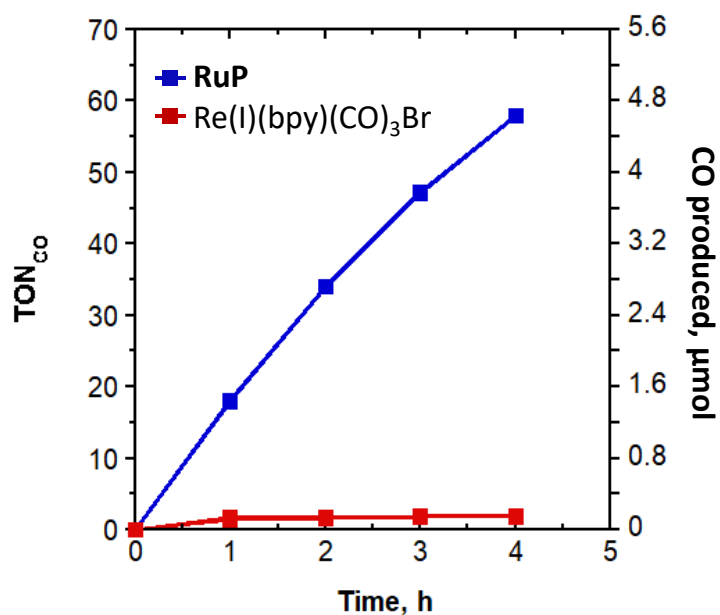
Figure 5: Turnover number and amounts of CO produced as a function of irradiation time between **RuP** and Re(I)(bpy)(CO)$_3$Br. Condition: 40 μM of catalyst, 0.1 M BIH, in CO_2-saturated DMA/H₂O (39:1, v/v), Xe lamp (420 ≤ λ ≤ 750 nm), 4 h.
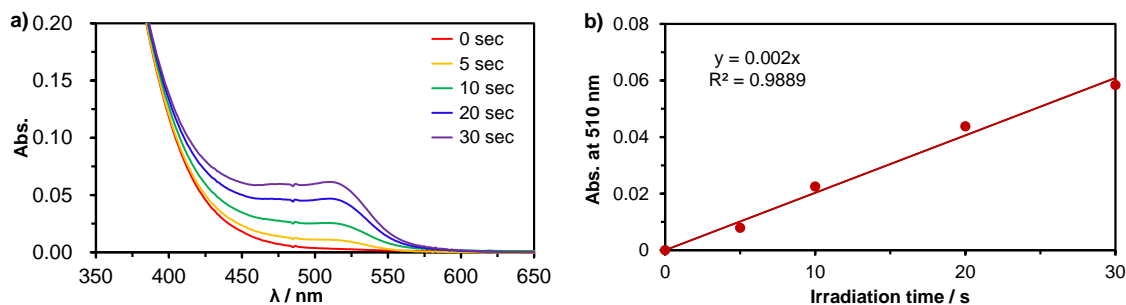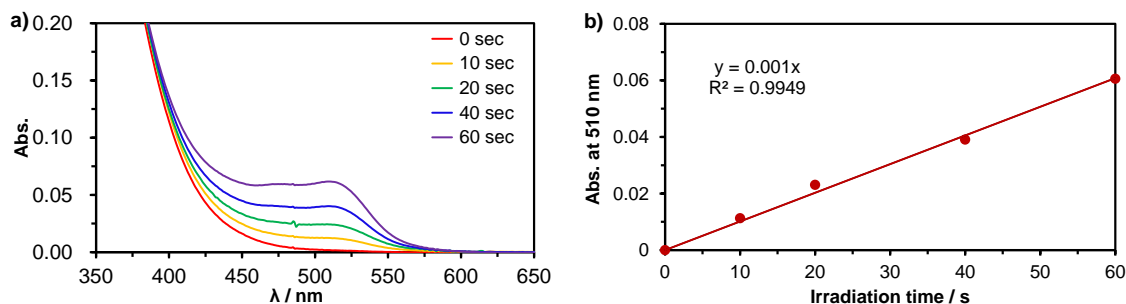
Figure 6: (a) Absorbance changes of $K_3[Fe^{III}(C_2O_4)_3]$ and 1,10-phenanthroline mixture solution after photo-irradiation at 450 nm. (b) Time course of absorbance at 510 nm measured from the solution.

Based on the slope of the plot 6 (b), the rate of photon flux of incident light intensity (I) is determined as 6.16×10^{-9} einstein s^{-1}. After 20 h of irradiation, 3.81 µmol of CO was produced. The quantum yield obtained under this condition is $\phi_{CO} = 1.7$ %. The details of calculation is shown in Experimental Section.

Figure 7: (a) Absorbance changes of $K_3[Fe^{III}(C_2O_4)_3]$ and 1,10-phenanthroline mixture solution after photo-irradiation at 450 nm equipped with neutral density 0.3 (ND 0.3) glass filter to reduce 50 % of the light intensity. (b) Time course of absorbance at 510 nm measured from the solution.

Based on the slope of the plot 7 (b), the rate of photon flux of incident light intensity (I) is determined as 3.08×10^{-9} einstein s^{-1}. After 20 h of irradiation, 2.87 µmol of CO was produced. The quantum yield obtained under this condition is $\phi_{CO} = 2.6$ %. The details of calculation is shown in Experimental Section.

Control experiments

To verify the role of each component in the photoreaction, a series of control experiments were carried out. No CO_2 reduction product was observed when performing the reaction either under argon, in the dark, without **RuP**, or without BIH (Table 1, entries 2–5), showing that CO_2 is the substrate, **RuP** is the photocatalyst, and BIH is needed as a sacrificial electron donor for the photocatalysis. The isotopic labelling experiments performed under $^{13}CO_2$ atmosphere also confirm that CO was originating from CO_2 reduction (Figure 8). In the absence of H_2O, approximately 4-fold lower amount of CO was produced (Figure 9), indicating the role of H_2O as proton source in the catalytic CO production.[25-27] Furthermore, the addition of excess Hg(0) did not significantly affect the photocatalytic activity (Figure 10), which confirms that a homogeneous molecular-based species is catalytically active.[28-29] These evidences clearly support that **RuP** can function as both the sensitizer (harvest visible-light) and catalyst (active site) to promote photocatalytic CO_2 reduction.
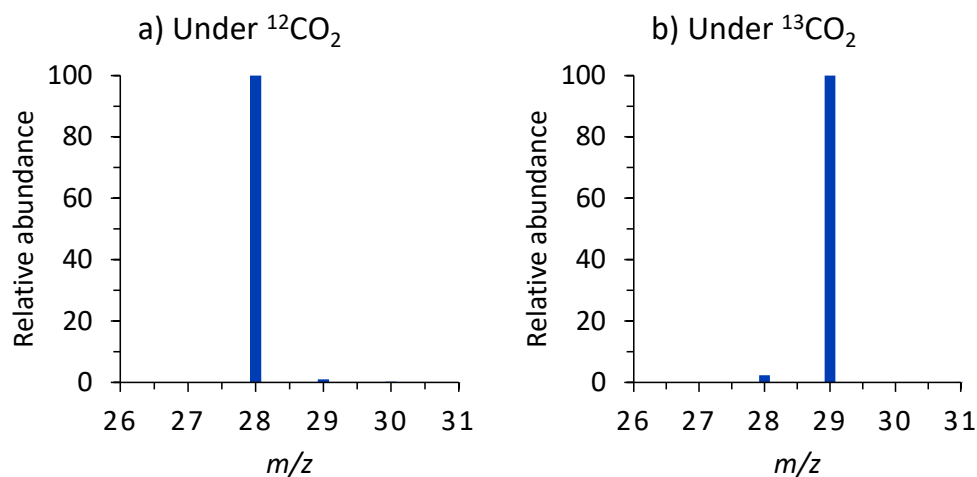
Figure 8: Mass spectra of CO generated under (a) $^{12}CO_2$ or (b) $^{13}CO_2$ atmosphere using DMA/H_2O (39:1, v/v) solution containing 40 μM **RuP** and 0.1 M BIH at 20 ℃ upon irradiated with Xe lamp (420 ≤ λ ≤ 750 nm) for 4 h. Under $^{13}CO_2$, >97 % of ^{13}CO was produced, supporting that the CO was originating from CO_2 reduction.
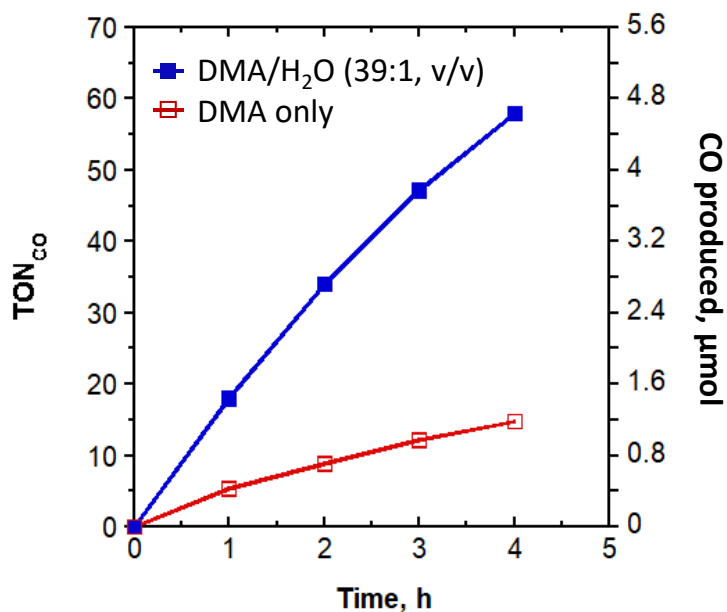
Figure 9: Turnover number for CO evolution over 4 h of irradiation ($420 \leq \lambda \leq 750$ nm) in CO_2-saturated DMA solution containing 40 μM **RuP**, 0.1 M BIH in the absence or presence of H_2O (DMA/H_2O (39:1, v/v)).
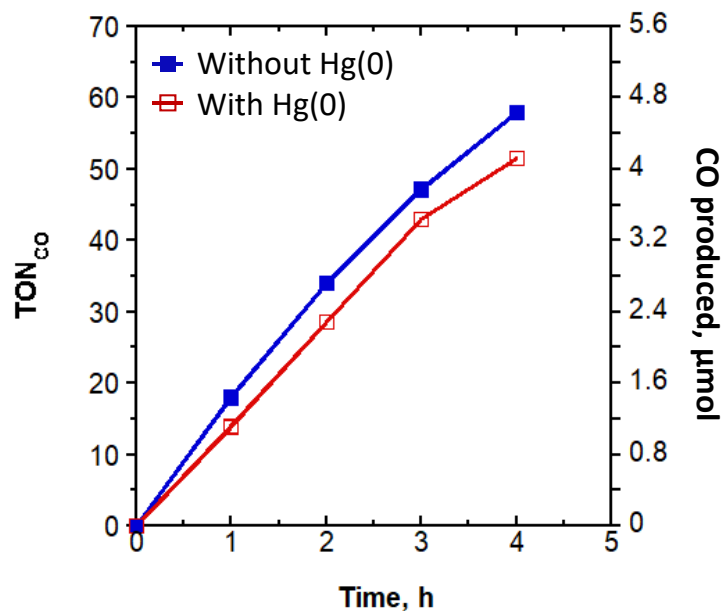

Figure 10: The effect of Hg(0) for CO evolution over 4 h of irradiation ($420 \leq \lambda \leq 750$ nm) in CO_2-saturated DMA/H_2O (39:1, v/v) solution containing 40 μM **RuP** and 0.1 M BIH.

Factors affecting the photocatalytic activity

The photocatalytic activity of **RuP** can be affected by several factors. The TON for CO production was increased as the concentration of **RuP** decreased (Table 2, entries 1–3), probably due to the decreased competitive photon absorption by the catalyst. The TON for CO evolution was also affected by solvents; the reaction in DMA resulted in higher CO evolution as compared that in MeCN (Table 2, entries 2 & 4). In addition, the concentration of H_2O can influence the catalytic activity. Highest CO selectivity was obtained in DMA/H_2O (39:1, v/v, Table 2, entry 2), whereas the amount of the evolved CO reached to the maxima at a higher concentration of H_2O (DMA/H_2O (19:1, v/v), Table 2, entry 5). More increase in the concentration of H_2O ((DMA/H_2O (9:1, v/v)) resulted in the lower catalytic performance of **RuP** (Table 2, entry 6) maybe due to the low stability of the complex in this experimental condition.

Table 2: Photocatalytic CO_2 reduction by **RuP** irradiated at $420 \leq \lambda \leq 750$ nm for 4 h under different conditions.

No.	[**RuP**]	Solvent	Electron	Turnover numbers (selectivity %)		
	(μM)		donor	CO	HCOOH	H_2
1	20	DMA/H_2O (39:1, v/v)	BIH	73 (89)	8 (10)	1 (1)
2	40	DMA/H_2O (39:1, v/v)	BIH	58 (94)	3 (5)	1 (1)
3	80	DMA/H_2O (39:1, v/v)	BIH	29 (94)	2 (6)	0 (0)
4	40	MeCN/H_2O (39:1, v/v)	BIH	42 (88)	5 (10)	1 (2)
5	40	DMA/H_2O (19:1, v/v)	BIH	67 (87)	9 (12)	1 (1)
6	40	DMA/H_2O (9:1, v/v)	BIH	20 (74)	6 (22)	1 (4)

Product selectivity for photochemical CO_2 reduction

The product of photocatalytic reaction drastically changed when a DMA/triethanol amine (TEOA) mixture (4:1, v/v) was used as reaction media. In this condition, **RuP** selectively produced HCOOH (>99 %) with the TON of 14, and negligible CO and H_2 evolution was observed (Table 1, entry 6). This change in product selectivity can be explained by considering the reactivity of the intermediate forms during the reaction.[30-31] In CO_2 reduction catalyzed by Ru-based complexes, the reduction of the catalyst induces the formation of the species with CO_2 molecule bound to the Ru center in η^1 fashion (η^1-CO_2). Subsequent protonation to the oxygen of η^1-CO_2 produces the corresponding C(O)OH bound species.[32-33] If the reaction media is acidic, further protonation and dehydrogenation generates the CO adduct. On the contrary, under basic condition, $HCOO^-$ is released from the complex via the ligand exchange reaction with the solvent.[30] These consideration also explains the product selectivity of **RuP** that the use of basic TEOA enhance the production of HCOOH. Therefore, the change in the product selectivity observed in **RuP** is arose from the nature of the Ru center. Note that such unique selectivity has not been reported for other non-sensitized photocatalysts, which do not contain Ru as metal centers, for CO_2 reduction.

Proposed catalytic mechanism

Scheme 1 illustrates a possible catalytic cycle for the photocatalytic reduction of CO_2 mediated by **RuP**. First, **RuP** is excited by photo-irradiation, and the resulting lowest excited state ^{3}MLCT of **RuP** could be reductively quenched by BIH (Step I in Scheme 1). This process was monitored using to a solution containing **RuP** (40 μM) and BIH (10 mM) by spectroscopic measurements. Upon irradiation of the visible light ($420 \leq \lambda \leq 750$ nm) to the solution under Ar, the spectra gradually changed with isosbestic points at 455 nm (Figure 11), suggesting the photo-induced one electron reduction at tpy moiety of **RuP** to afford $[Ru^{II}(tpy^-)(pqn)(MeCN)]^+$ (**RuP⁻**). Subsequently, the ligand exchange reaction between the monodentate labile ligand and CO_2 proceeds, generating the CO_2 adduct, **RuP**$_{CO_2}$$^{•-}$ (Step II).[25] As I previously reported,[25] the phosphine donor destabilizes the bond between the Ru centre and the nitrogen atom of the MeCN ligand via σ-donation (*trans* influence) and stabilizes the bond between the Ru centre and the carbon atom of the coordinated CO_2 molecule via π-back donation, which enables the catalyst to react with CO_2 at its one-electron reduced state. **RuP**$_{CO_2}$$^{•-}$ can easily undergo further one-electron reduction (Step III), and the subsequent protonation reaction (Step IV) forms the key intermediate, $[Ru^{II}(tpy^-)(pqn)(CO_2H)]^+$. As discussed in the previous section, the reactivity of this intermediate changes depending on the basicity of the reaction media. Under basic condition, the liberation of CO_2H from the intermediate gives HCOOH as a product (Step V), whereas the protonation and dehydration reactions generates the carbonyl complex, $[Ru^{II}(tpy)(pqn)(CO)]^{2+}$ (**RuP**$_{CO}$), under acidic condition (Step VI). Single crystal X-ray structure of **RuP**$_{CO}$, which was separately prepared by the reaction of **RuP** with CO in non-coordinating solvent, revealed the *trans* influence of the phosphine ligand weakens the Ru–C bond of **RuP**$_{CO}$ (Figure 12, Table 3). As a result, **RuP**$_{CO}$ can easily undergo the rapid ligand exchange reaction with coordinating solvent (Figure 13–14), which regenerates **RuP** and produce CO as a major product (Step VII). It should also be noted that once **RuP⁻** is generated by photochemical reaction, later processes to obtain CO proceeds without further photoirradiation. Actually, bubbling of CO_2 to the solution of **RuP⁻** under dark condition generates **RuP** (Figure 15), which indicates the regeneration of **RuP** after the catalytic cycle.
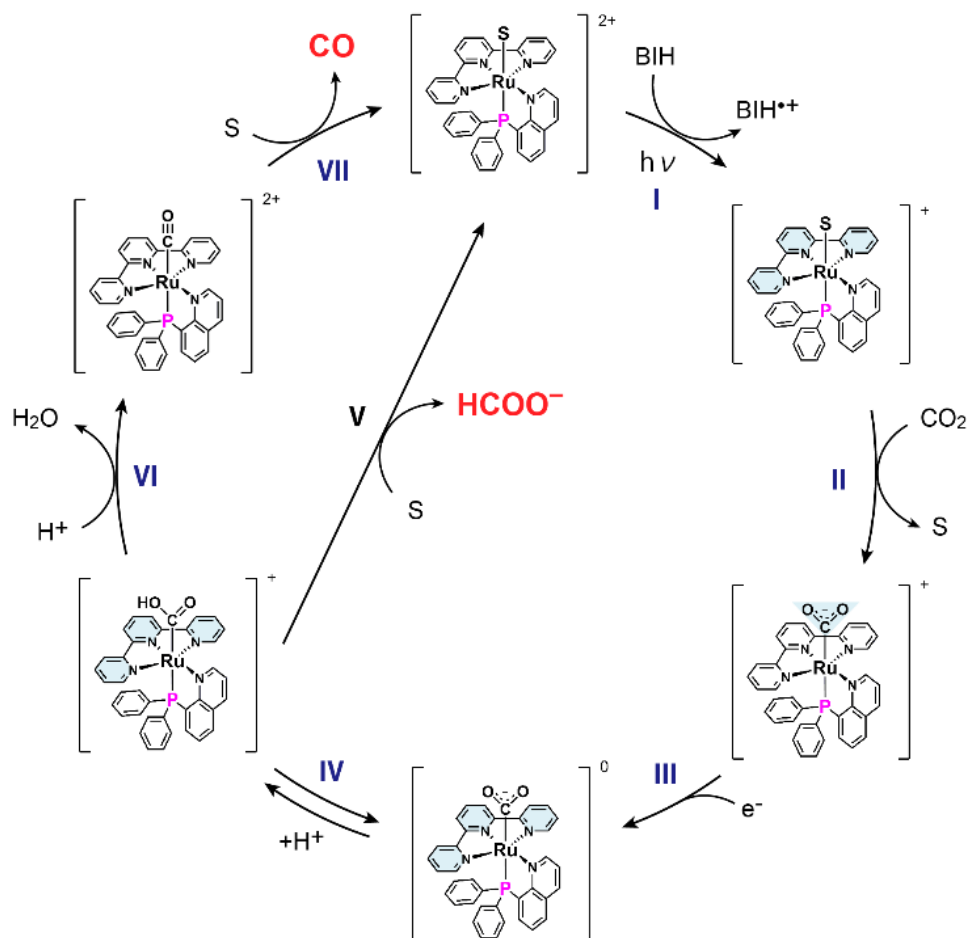
Scheme 1: Proposed catalytic mechanism for photocatalytic CO_2 reduction by **RuP** under visible-light irradiation. S indicates solvent molecule. Reduced ligands are highlighted with pale blue.
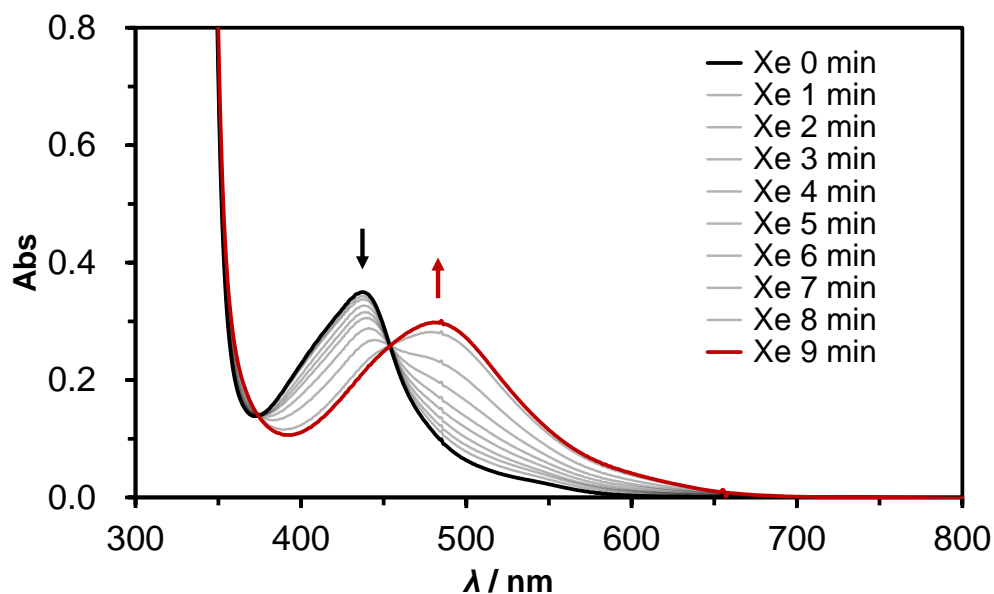
Figure 11: UV-vis spectral changes of an Ar-saturated MeCN solution containing 40 μM of **RuP** and 10 mM of BIH upon photo-irradiation. The growth of new absorption band at 480 nm originates from the formation of the one-electron reduced species (**RuP⁻**, red line), indicating that the lowest excited state ³MLCT of **RuP** could be reductively quenched by BIH.
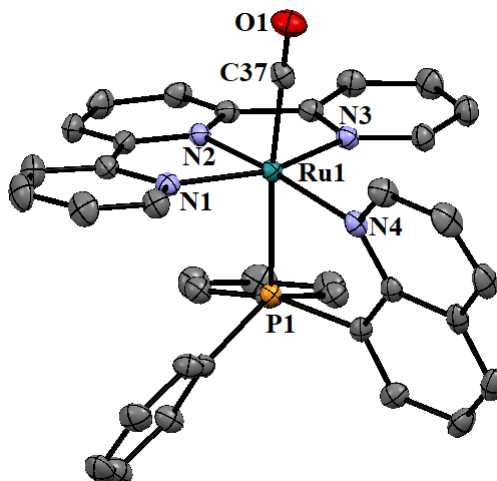
Figure 12: An ORTEP drawing (50 % probability thermal ellipsoids) of **RuP$_{CO}$**. Counter anions and hydrogen atoms were omitted for clarity. The bond distances between the Ru and N atoms for **RuP$_{CO}$** (Ru1–N1 = 2.099 Å, Ru1–N2 = 1.988 Å, Ru1–N3 = 2.104 Å, Ru1–N4 = 2.148 Å) are similar to those for the relevant compound, [Ru(tpy)(bpy)(CO)]$^{2+}$ (Ru–N = 1.988–2.114 Å).[33] However, **RuP$_{CO}$** exhibits a significantly longer Ru–C(CO) bond (1.938 Å) than [Ru(tpy)(bpy)(CO)]$^{2+}$ (Ru–C(CO) = 1.844 Å),[33] which is attributed to the *trans* influence exerted by the phosphine ligand at the position *trans* to CO ligand. This indicates that the Ru–C bond of **RuP$_{CO}$** should be more labile compared to that of [Ru(tpy)(bpy)(CO)]$^{2+}$.

Table 3: Summary of crystallographic data for **RuP$_{CO}$**

	[Ru(tpy)(pqn)(CO)](PF$_6$)$_2$ (**RuP$_{CO}$**)
Formula	C$_{37}$H$_{27}$N$_4$OP$_3$F$_{12}$Ru
Formula weight	956
Crystal system	Monoclinic
Space group	$P2_1/c$
a (Å)	12.0274 (2)
b (Å)	14.8900 (3)
c (Å)	20.8508 (4)
α (°)	90.00
β (°)	94.768 (7)
γ (°)	90.00
V (Å^3)	3721.21 (12)
Z	4
R_1 (%)	6.19
GOF	1.034
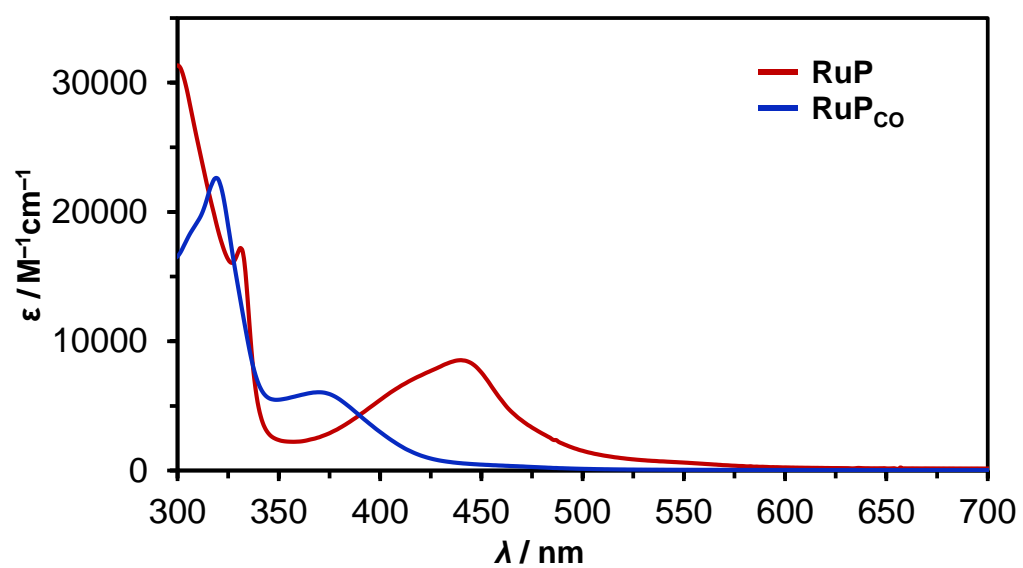
Figure 13: UV-Vis absorption spectra of **RuP** and [Ru(tpy)(bpy)(CO)]$^{2+}$ (**RuP$_{CO}$**) in DCM.
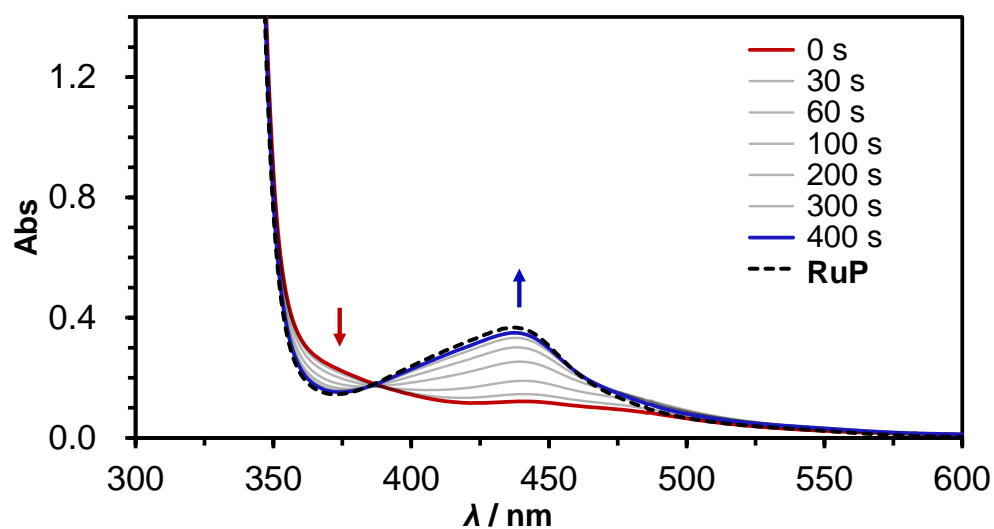
Figure 14: UV-Vis absorption spectral changes of 40 µM **RuP$_{CO}$** in an Ar-saturated MeCN/H$_2$O (39:1, v/v) mixed solution containing 10 mM BIH at 20 ºC and an UV-Vis absorption spectrum of **RuP** under Ar. **RuP$_{CO}$** undergoes ligand exchange reaction and **RuP** generates after the reaction. Note that the reaction was rapid and **RuP** formed soon after **RuP$_{CO}$** was dissolved into the solvent. Therefore, the band at 436 nm, which is assigned to the MLCT band of **RuP**, was observed even at 0 s.
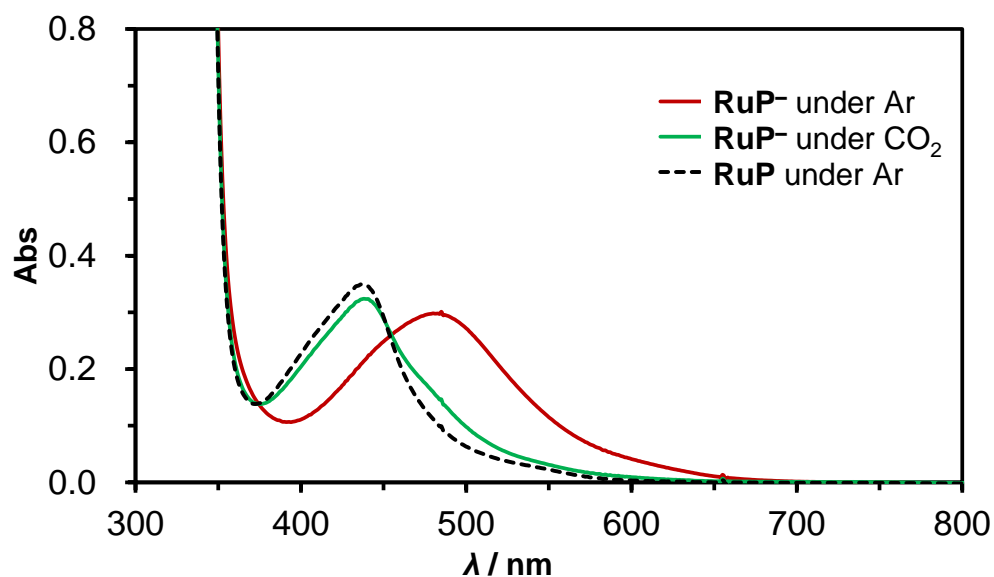
Figure 15: UV-Vis absorption spectral changes upon bubbling of CO_2 into an Ar-saturated MeCN/H_2O (39:1, v/v) mixed solution containing 40 µM of **RuP** and 10 mM of BIH after photoirradiation and an UV-Vis absorption spectrum of **RuP** under Ar. CO_2 introduced into the cell under dark condition. The growth of the band at 437 nm was observed and the spectrum obtained after bubbling of CO_2 was almost identical to that of **RuP**. The result indicates the regeneration of **RuP** after the reduction of CO_2.

Optimization of reaction conditions

After condition optimization, a TON_{CO} of 353 (24 h) that corresponding to a $TOF = 14.7 \; h^{-1}$ was achieved using 5 µM **RuP** under visible-light irradiation (Figure 16). This performance of **RuP** is superior to those of current best-in-class photocatalysts (Table 4).[15,19,20,34,35,36,37,38] It should be also noted initial rates of CO evolution exhibit a linear relationship with the concentration of **RuP**, [**RuP**], when [**RuP**] is in the range of 2.5–10 µM (Figures 17 & 18), suggesting that the diffusion and collision of the catalyst is not involved in the rate determining step. Based on Figure 18 (b), the initial rate for CO evolution is approximately 25,173 µmol h^{-1} g^{-1}. These numbers represent greatest TON and CO evolution rate values that have been reported for visible-light driven homogeneous non-sensitized photocatalysts to date.
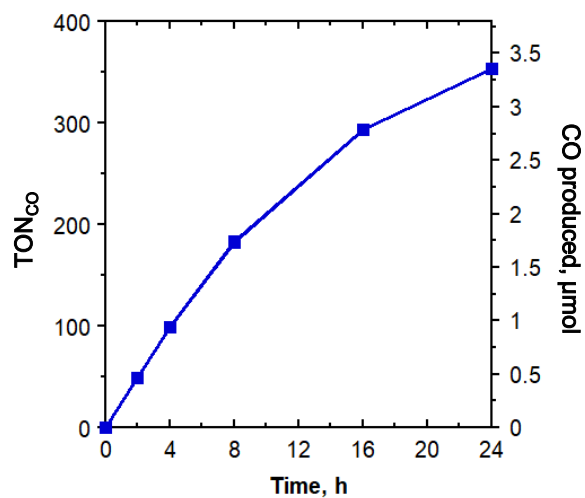
Figure 16: Turnover number of CO formed as a function of irradiation time. A CO_2-saturated DMA/H_2O (39:1, v/v) solution containing 5.0 μM **RuP** and 0.20 M BIH was irradiated using a Xe lamp equipped with 420 nm long pass filter, producing light in the range of ($420 \leq \lambda \leq 750$ nm) for 24 h.
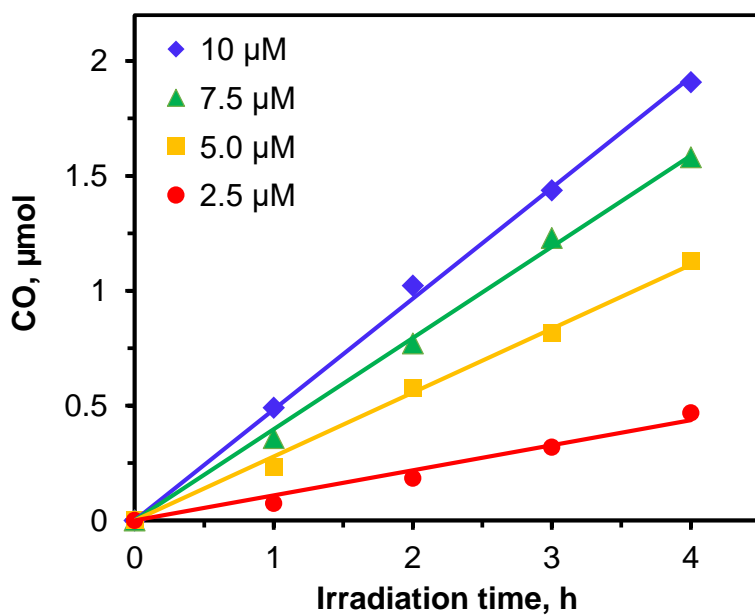
Figure 17: Time course of CO production in the photocatalytic reaction by irradiation ($420 \leq \lambda \leq 750$ nm) of a DMA/H$_2$O (39:1, v/v) solution containing **RuP** (red circles: 2.5 µM, yellow squares: 5.0 µM, green triangles: 7.5 µM, blue diamonds: 10 µM).
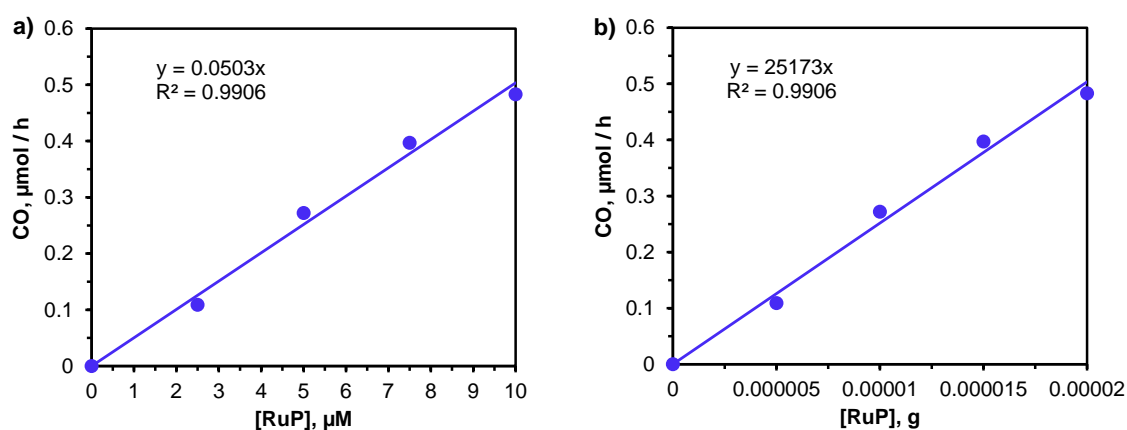
Figure 18: Concentration dependence of **RuP** on CO evolution rate.

RuP   **Re(I)(bpy)(CO)₃Br**   **Re(N,S-NHC)**   **Re(Py-NHC-PhCF₃)**   **Ir-Meppy**   **Ir(9-anthryl-tpy)**

FeTPP   **CAT**   **FCAT**   **Fe-p-TMA**   **CoTPP**
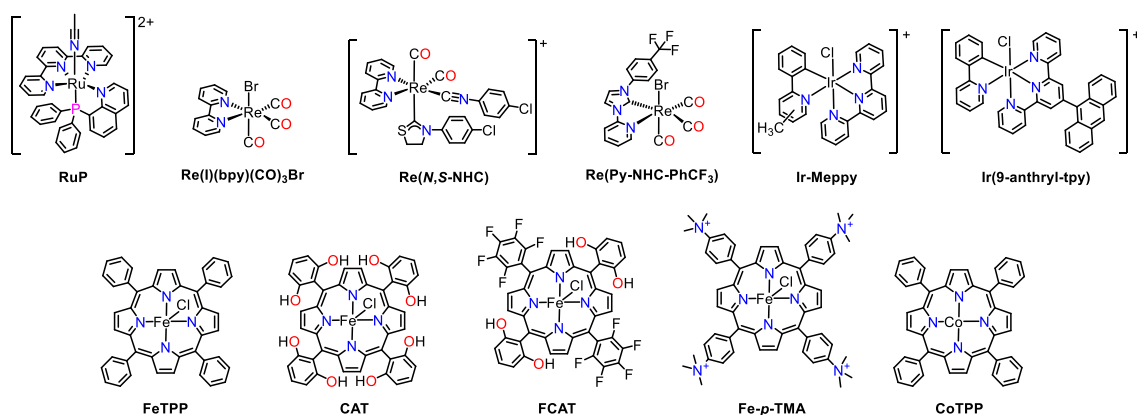
Table 4: A comparison of the state-of-the-art non-sensitized molecular photocatalysts for CO_2 reduction. Their chemical structures are shown above.

Photocatalyst	Incident light	SD	Reaction solution	Product	TON	TOF[a]	Ref.
RuP	$420 \leq \lambda \leq 750$ nm	BIH	DMA/H₂O (39:1, v/v)	CO	353 (24 h)	14.7	This
		TEOA	DMA/TEOA (4:1, v/v)	HCOOH	14 (4 h)	3.5	work
Re(I)(bpy)(CO)₃Br	$420 \leq \lambda \leq 750$ nm	BIH	DMA/H₂O (39:1, v/v)	CO	2 (4 h)	0.5	This
		TEOA	DMA/TEOA (4:1, v/v)	CO	8 (4 h)	2.0	work
Re(I)(bpy)(CO)₃Br	$\lambda > 400$ nm	TEOA	DMF/TEOA (5:1, v/v)	CO	20 (4 h)	5.0	[15]
Re(N,S-NHC)	$\lambda \geq 400$ nm	BIH	DMF/TEOA (5:1, v/v)	CO	102 (15 h)[b]	6.8	[19]
	$\lambda > 480$ nm	BIH	DMF/TEOA (5:1, v/v)	CO	153 (15 h)[c]	10.2	
Re(Py-NHC-PhCF₃)	$\lambda > 300$ nm	BIH	5 % TEA/MeCN	CO	32 (4 h)	8.0	[20]
FeTPP	$\lambda > 280$ nm	TEA	0.36 M TEA, MeCN	CO	17 (10 h)	1.7	[34]
				H₂	37 (10 h)	3.7	
CAT	$\lambda > 280$ nm	TEA	0.36 M TEA, MeCN	CO	28 (10 h)	2.8	[34]
				H₂	10 (10 h)	1.0	
FCAT	$\lambda > 280$ nm	TEA	0.36 M TEA, MeCN	CO	23 (10 h)	2.3	[34]
				H₂	15 (10 h)	1.5	
Fe-p-TMA	$\lambda > 420$ nm	TEA	50 mM TEA, MeCN	CO	33 (47 h)	0.7	[35]
		BIH	0.1 M TFE, MeCN	CO	78 (47h)	1.7	
CoTPP	$\lambda > 320$ nm	TEA	5% TEA/MeCN	CO	80 (200 h)	0.4	[36]
Ir-Meppy	$410 \leq \lambda \leq 750$ nm	TEOA	DMF/TEOA (5:1, v/v)	CO	50 (5 h)	10	[37]
Ir(9-anthryl-tpy)	450 nm	TEOA	MeCN/TEOA (5:1, v/v)	CO	265 (300 h)	0.9	[38]

[a]Turnover frequency (TOF) was calculated by dividing the turnover number (TON) by duration of photoreaction.

[b]The CO evolution reached plateau around 3 h of photoirradiation.

[c]The CO evolution slowly reached plateau after 15 h due to the low-energy visible light source.

Conclusion

In summary, I report the first example of non-sensitized mononuclear Ru(II) photocatalyst, **RuP**, for CO_2 reduction. The catalyst exhibited highest TOF and TON values for CO production among the reported non-sensitized photocatalysts. Although there had been no precedent report of a non-sensitized Ru-based photocatalyst for CO_2 reduction, two fascinating features of the Ru-based complexes, strong absorption properties in the visible-light region[12,39-40] and catalytic activity for CO_2 reduction[11-12,30-33], implies their potential application as non-sensitized photocatalysts for CO_2 reduction. This study clearly demonstrates that the appropriate design of the complex can afford an excellent non-sensitized catalyst. The superior photochemical CO_2 reduction activity of **RuP** is owing to several reasons. Firstly, Ru polypyridyl scaffold can strongly absorb the visible light which triggers the formation of photo-induced one-electron reduced Ru species. Second, **RuP** contains a monodentate labile site for substrate association (CO_2) and products dissociation (CO or HCOOH) during the photo-induced reduction reaction. Thirdly, the σ-donating ability of the phosphine enables the CO_2 binding at the one-electron reduced state of the Ru complex (EC mechanism), and the labilization of CO ligand from **RuP**co. It should be also noted that the nature of Ru center enables the control of the product selectivity by simply changing the basicity of the reaction media. Current work provides a novel strategy to design a new generation of non-sensitized photocatalyst, not limited for CO_2 reduction, but possibly applicable for other photoredox catalytic reaction.

Experimental Details

General procedures

8-(Diphenylphosphanyl)quinoline (pqn),[21-22] and *trans*(*P,MeCN*)-[Ru^{II}(tpy)(pqn)(MeCN)](PF$_6$)$_2$ (**RuP**),[23-25] were synthesized according to literature procedures. All the solvents were purchased from Wako Pure Chemical Industries, while the chemicals were purchased from Sigma-Aldrich Co. All the reagents were of highest quality available and were used as received. ^{1}H-NMR, ^{13}C-NMR, and ^{31}P-NMR spectra were collected at room temperature on a JEOL JNM-ECS400 spectrometer. UV-vis absorption spectra were measured on a Shimadzu UV-2450SIM spectrophotometer at room temperature. Elemental analyses were performed on a J-Science Lab Micro Corder JM10 elemental analyzer. ESI-TOF-MS spectra were collected on a JEOL JMS-T100LC mass spectrometer.

Syntheses

trans(*P,CO*)-[Ru^{II}(tpy)(pqn)(CO)](PF$_6$)$_2$ (**RuPco**) was synthesized by stirring **RuP** in CO-saturated DCM solution at room temperature for 3 h. The orange solution turned into light yellow. Then, Et$_2$O was added into the solution to precipitate the desired compound **RuPco** as yellow powder (yield = ~95 %). Purification was achieved by recrystallization with DCM/Et$_2$O at 4 ℃. ESI-TOF MS (positive ion, DCM): m/z 324.1 ([Ru(tpy)(pqn)]$^{2+}$), 338.1 ([Ru(tpy)(pqn)(CO)]$^{2+}$), 821.1 ([Ru(tpy)(pqn)(CO)]$^+$PF$_6$). Anal. Found: C, 45.88; H, 3.09; N, 5.81. Calculated for C$_{37}$H$_{27}$N$_4$OP$_3$F$_{12}$Ru (**RuPco**): C, 46.02; H, 2.82; N, 5.80.

1,3-dimethyl-2-phenyl-2,3-dihydro-1*H*-benzo[d]imidazole (BIH) was synthesized according to literature.[41-42] *N,N'*-dimethyl-1,2-phenylenediamine (1 ml, 9.3 mmol) was added with slight excess of benzaldehyde (1 ml, 10 mmol) in 8 ml of MeOH. 8 drops of glacial acetic acid was added and the solution was sonicated for 30 minutes at room temperature until precipitation was observed. The pinkish white precipitate was collected by vacuum filtration and washed with cold MeOH/H$_2$O solution. The crude product was further recrystallized from MeOH/H$_2$O to give the pure white crystalline powder (yield = ~ 54 %). ^{1}H NMR (CD$_3$CN): δ 7.53–7.42 (m, 5H), 6.63 (dd, 2H), 6.42 (dd, 2H), 4.82 (s, 1H), 2.48 (s, 6H). Anal. Found: C, 80.43; H, 7.21; N, 12.44. Calculated for C$_{15}$H$_{16}$N$_2$ (BIH): C, 80.32; H, 7.19; N, 12.49.

Photocatalytic reaction

For typical run, a mixed solution of DMA/H_2O (39:1, v/v) (2.0 ml) containing 40 μM **RuP** and 0.10 M BIH was purged with CO_2 for 20 minutes unless otherwise stated. The solution was then irradiated with a 150 W Xe lamp equipped with 420 nm long pass filter (Edmund Industrial Optics) to produce the light in the range of $420 \leq \lambda \leq 750$ nm at 20 ºC in a custom made aluminium box with cooling system as shown below (Figure 19). The amount of CO and H_2 produced at the headspace of the cell was quantified by a Shimadzu GC-8A with a TCD detector equipped with a packed column with Molecular Sieve 13X-S 60/80. Additionally, liquid product was quantified by using a Shimadzu LC-20AD with SPD-20A and RID-10A detectors equipped with a Shim-pack SCR102H column. Calibration curves were obtained by sampling known amounts of H_2, CO, and HCOOH.
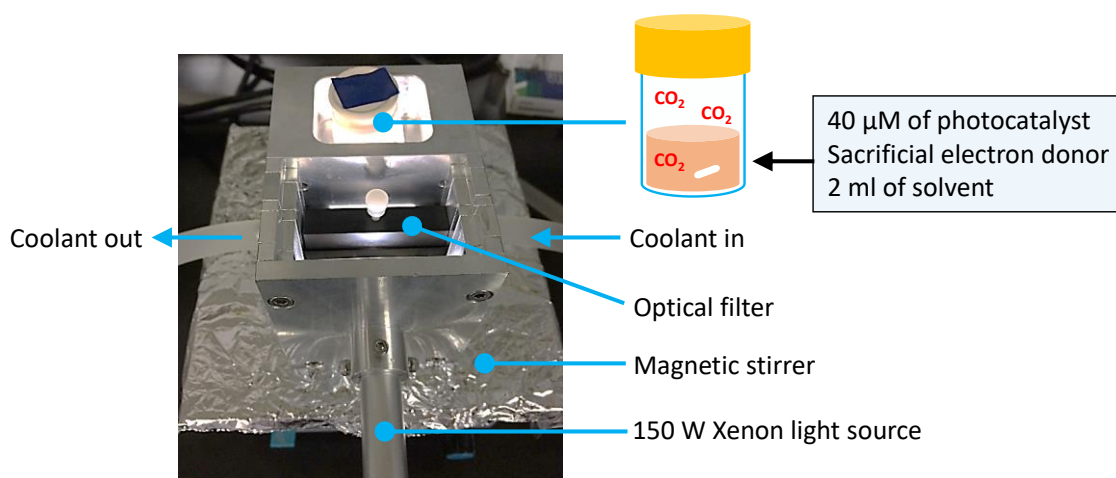
Figure 19: General setup for photochemical CO_2 reduction carried out in this work.

Quantum yield determination

The incident light intensity was estimated using a potassium ferrioxalate ($K_3[Fe^{III}(C_2O_4)_3]$) actinometer.[43-44] 2 ml (V_1) of 10 mM $K_3[Fe^{III}(C_2O_4)_3]$ in buffered solution was irradiated with Xe lamp combined with 450 nm band pass filter (fwhm = 10 nm, Edmund Industrial Optics) under efficient stirring. Note that neutral density (ND) glass filters were used in order to reduce the light intensity.

Next, 0.5 ml (V_2) of the irradiated solution was transferred into 10 ml (V_3) buffer solution containing phen (1,10-phenanthroline), and incubated in the dark for 1 h. The ferrous ion formed then reacts with phen to develop the red $[Fe^{II}(phen)_3]^{2+}$ complex with intense absorbance at 510 nm. The absorbance of the solution was recorded (Figure 6a & 7a) and the linear relationship between the absorption intensity at 510 nm and irradiation time was observed (Figure 6b & 7b).

The rate of photon flux of the incident light intensity (I) was calculated using the following equation: I (einstein s^{-1})= ($\Delta A\ V_1\ V_3$) / ($\phi_\lambda\ \varepsilon_{510}V_2\ l\ t$), where ΔA = absorbance at 510 nm, $V_1 = 0.002$ L, $V_2 = 0.0005$ L, $V_3 = 0.01$ L, ϕ_λ = quantum yield for $[Fe^{II}(phen)_3]^{2+}$ formation (1.12),[43-44] ε_{510} = molar absorption coefficient of $[Fe^{II}(phen)_3]^{2+}$ (11590 Lmol^{-1}cm^{-1}), l = length of cuvette (1 cm), t = photo-irradiation time (s). The incident light intensity were determined to be 6.16 x 10^{-9} einstein s^{-1} without ND filter, and 3.08 x 10^{-8} einstein s^{-1} with ND 0.3 filter under the aforementioned experimental condition.

Then, a mixed solution of DMA/H_2O (39:1, v/v) (2.0 ml) containing 40 μM **RuP** and 0.10 M BIH was irradiated with Xe lamp equipped with a 450 nm band pass filter in the presence or absence of ND filter, and the amount of the generated CO during catalysis was determined by GC. The amount of the generated CO after 20 h of photo-irradiation were 3.81 μmol and 2.87 μmol in absence and presence of ND 0.3 filter respectively.

Quantum yield of the reaction was calculated by following equation: QY (%) = (2 x R/I) x 100%,[45] where R (mol s^{-1}) is the CO evolution rate and I (einstein s^{-1}) is the rate of photon flux of incident light.

$^{13}CO_2$ labeling experiment

A mixed solution of DMA/H_2O (39:1, v/v) (2.0 ml) containing 40 μM **RuP** and 0.10 M BIH was purged with Ar for 15 min, followed by $^{13}CO_2$ bubbling for 15 min (Figure 20). The $^{13}CO_2$ gas was produced by adding 2.0 M HCl to solid $Ba^{13}CO_3$ (98 atom % ^{13}C, Sigma Aldrich). After photoreaction, the evolved CO was detected by a GCMS-QP2020 (Rt®-Msieve 5A (30 m, 0.53 mm ID, 50 μm d_f) He carrier gas, 40 °C).
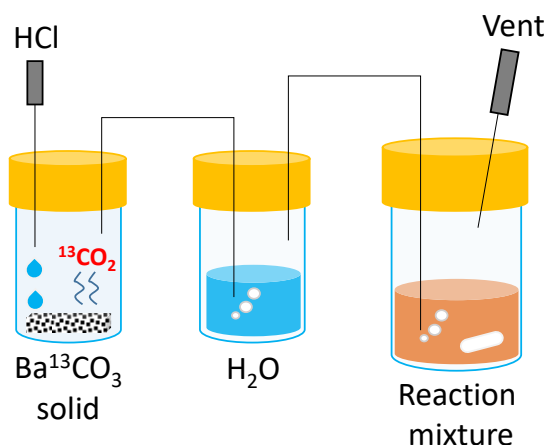

Figure 20: General setup for $^{13}CO_2$ labeling experiment.

Crystallography

The diffraction data of a crystal of **RuPCO** at 123 K were measured on a Rigaku R-AXIS RAPID imaging plate diffractometer equipped with confocal monochromated MoKα radiation, and the data were processed using RAPID AUTO (Rigaku). The structure was solved by the direct method using *SIR-92*[46] and refined by the full-matrix least squares techniques on F^2 (*SHELXL-2014/7*).[47] All non-hydrogen atoms were refined anisotropically and refined with a riding model with U_{iso} constrained to be 1.2 times U_{eq} of the carrier atom. The diffused electron densities resulting from residual solvent molecules were removed from the dataset using the *SQUEEZE* routine of *PLATON*[48] and refined further using the generated data. CCDC 1834671 for **RuPCO** contains the supplementary crystallographic data for this paper. These data can be obtained free of charge from The Cambridge Crystallographic Data Centre.

References:

1) A. Magnuson, M. Anderlund, O. Johansson, P. Lindblad, R. Lomoth, T. Polivka, S. Ott, K. Stensjö, S. Styring, V. Sundström, L. Hammarström, *Acc. Chem. Res.* 2009, **42**, 1899-1909.

2) M. Mikkelsen, M. Jørgensen, F. C. Krebs, *Energy Environ. Sci.* 2010, **3**, 43-81.

3) T. J. Meyer, *Acc. Chem. Res*. 1989, **22**, 163-170.

4) N. S. Lewis, D. G. Nocera, *Proc. Natl. Acad. Sci. U. S. A*. 2006, **103**, 15729-15735.

5) H. Rao, L. C. Schmidt, J. Bonin, M. Robert, *Nature* 2017, **548**, 74-77.

6) K. Kobayashi, T. Kikuchi, S. Kitagawa, K. Tanaka, *Angew. Chem. Int. Ed.* 2014, **53**, 11813-11817.

7) V. S. Thoi, N. Kornienko, C. G. Margarit, P. Yang, C. J. Chang, *J. Am. Chem. Soc.* 2013, **135**, 14413-14424.

8) T. Ogata, S. Yanagida, B. S. Brunschwig, E. Fujita, *J. Am. Chem. Soc*. 1995, **117**, 6708-6716.

9) Y. Kuramochi, J. Itabashi, K. Fukaya, A. Enomoto, M. Yoshida, H. Ishida, *Chem. Sci*. 2015, **6**, 3063-3074.

10) T. Nakajima, Y. Tamaki, K. Ueno, E. Kato, T. Nishikawa, K. Ohkubo, Y. Yamazaki, T. Morimoto, O. Ishitani, *J. Am. Chem. Soc*. 2016, **138**, 13818-13821.

11) Y. Tamaki, O. Ishitani, *ACS Catal*. 2017, **7**, 3394-3409.

12) H. Takeda, O. Ishitani, *Coord. Chem. Rev*. 2010, **254**, 346-354.

13) B. Gholamkhass, H. Mametsuka, K. Koike, T. Tanabe, M. Furue, O. Ishitani, *Inorg. Chem.* 2005, **44**, 2326-2336.

14) Y. Tamaki, T. Morimoto, K. Koike, O. Ishitani, *Proc. Natl. Acad. Sci. U.S.A.* 2012, **109**, 15673-15678.

15) J. Hawecker, J. M. Lehn, R. J. Ziessel, *Chem. Soc. Chem. Commun*. 1983, 536-538.

16) J. Hawecker, J. M. Lehn, R. Ziessel, *Helv. Chim. Acta* 1986, **69**, 1990-2012.

17) R. A. Kirgan, B. P. Sullivan, D. P. Rillema, *Top. Curr. Chem*. 2007, **281**, 45-100.

18) C. Kutal, M. A. Weber, G. Ferraudi, D. Geiger, *Organometallics* 1985, **4**, 2161-2166.

19) A. Maurin, C.-O. Ng, L. Chen, T.-C. Lau, M. Robert, C.-C. Ko, *Dalton Trans*. 2016, **45**, 14524-14529.

20) A. J. Huckaba, E. A. Sharpe, J. H. Delcamp, *Inorg. Chem*. 2016, **55**, 682-690.

21) T. Suzuki, T. Kuchiyama, S. Kishi, H. D. Takagi, M. Kato, *Inorg. Chem.* 2003, **42**, 785-795.

22) T. Suzuki, T. Kuchiyama, S. Kishi, S. Kaizaki, M. Kato, *Bull. Chem. Soc. Jpn.* 2002, **75**, 2433-2439.

23) G. Nakamura, M. Kondo, M. Crisalli, S. K. Lee, A. Shibata, P. C. Ford, S. Masaoka, *Dalton Trans.* 2015, **44**, 17189-17200.

24) G. Nakamura, M. Okamura, M. Yoshida, T. Suzuki, H. D. Takagi, M. Kondo, S. Masaoka, *Inorg. Chem.* 2014, **53**, 7214-7226.

25) S. K. Lee, M. Kondo, G. Nakamura, M. Okamura, S. Masaoka, *Chem. Commun.* 2018, **54**, 6915-6918.

26) Y. Kuramochi, M. Kamiya, H. Ishida, *Inorg. Chem.* 2014, **53**, 3326-3332.

27) C. Constentin, M. Robert, J. M. Savéant, *Acc. Chem. Res*. 2015, **48**, 2996-3006.

28) G. M. Whitesides, M. Hackett, R. L. Brainard, J.-P. P. M. Lavalleye, A. F. Sowinski, A. N. Izumi, S. S. Moore, D. W. Brown, E. M. Staudt, *Organometallics* 1985, **4**, 1819-1830.

29) M. Zahmakiran, M. Tristany, K. Philippot, K. Fajerwerg, S. Özkar, B. Chaudret, *Chem. Commun.* 2010, **46**, 2938-2940.

30) H. Ishida, K. Tanaka, T. Tanaka, *Organometallics* 1987, **6**, 181–186.

31) K. Kobayashi, K. Tanaka, *Phys. Chem. Chem. Phys*. 2014, **16**, 2240-2250.

32) P. Kang, Z. Chen, M. Brookhart, T. J. Meyer, *Top. Catal.* 2015, **58**, 30-45.

33) H. Nagao, T. Mizukawa, K. Tanaka, *Inorg. Chem.* 1994, **33**, 3415-3420.

34) J. Bonin, M. Chaussemier, M. Robert, M. Routier, *ChemCatChem*. 2014, **6**, 3200-3207.

35) H. Rao, J. Bonin, M. Robert, *Chem. Commun*. 2017, **53**, 2830-2833.

36) D. Behar, T. Dhanasekaran, P. Neta, C. M. Hosten, D. Ejeh, P. Hambright, E. Fujita, *J. Phys. Chem. A* 1998, **102**, 2870-2877.

37) S. Sato, T. Morikawa, T. Kajino, O. Ishitani, *Angew. Chem. Int. Ed*. 2013, **52**, 988-992.

38) A. Genoni, D. N. Chirdon, M. Boniolo, A. Sartorel, S. Bernhard, M. Bonchio, *ACS Catal*. 2017, **7**, 154-160.

39) D. M. Arias-Rotondo, J. K. McCusker, *Chem. Soc. Rev*. 2016, **45**, 5803-5820.

40) C. K. Prier, D. A. Rankic, D. W. C. MacMillan, *Chem. Rev*. 2013, **113**, 5322-5363.

41) X. Zhu, M. Zhang, A. Yu, C. Wang, J. Cheng, *J. Am. Chem. Soc*. 2008, **130**, 2501-2516.

42) D. Hong, Y. Tsukakoshi, H. Kotani, T. Ishizuka, T. Kojima, *J. Am. Chem. Soc.* 2017, **139**, 6538-6541.

43) H. J. Kuhn, S. E. Braslavsky, R. Schmidt, *Pure Appl. Chem.* 2004, **76**, 2105-2146.

44) S. Lee, Y. You, K. Ohkubo, S. Fukuzumi, W. Nam, *Chem. Sci*. 2014, **5**, 1463-1474.

45) R. Kuriki, K. Sekizawa, O. Ishitani, K. Maeda, *Angew. Chem. Int. Ed.* 2015, **54**, 2406-2409.

46) A. Altomare, G. Cascarano, C. Glacovazzo, A. Guagliardi, *J. Appl. Crystallogr.* 1993, **26**, 343-350.

47) G. M. Sheldrick, SHELXL 2014/7, University of Göttingen, Göttingen (Germany), 2014.

48) A. L. Spek, *Acta Crystallogr. Sect. D* 2009, **65**, 148-155.

Chapter 3

Ni complexes containing redox-active ligand for photocatalytic CO_2 reduction

Introduction

The development of a visible-light driven catalytic system for CO_2 conversion into carbon-based fuels and commodity chemicals is of utmost importance to overcome the world's energy and environmental crisis.[1-5] Numerous studies have shown that noble metal-based complexes such as Re, Ru, Rh, and Ir could efficiently promote photochemical CO_2 reduction to produce CO and HCOOH.[6-13] Recently, there has been considerable effort to replace the noble metal catalysts with earth-abundant first-row analogs.[12-23]

First-row transition metal complexes containing redox-active ligands have raised increasing attention for catalytic redox reaction because these complexes usually show multiple accessible redox states. Redox-active ligands with extensive conjugated systems can store reducing electrons in their π-network, which suppress the purely metal-centered reduction that is usually energetically more demanding.[24-25] Metal complexes containing redox-active ligands (e.g., polypyridyl-based and pyridine diimine-based) were shown to be active for CO_2 reduction.[12-15] Late first-row transition metals such as Fe, Co, and Ni tend to form octahedral polypyridyl complexes with saturated coordination sphere, such as $[M^{II}(tpy)_2]^{2+}$ and $[M^{II}(bpy)_3]^{2+}$ (tpy = 2,2′:6′,2″-terpyridine; bpy = 2,2′-bipyridine; M = Fe, Co, or Ni).[26-27] Mechanistic studies proposed that these metal complexes often dissociate one of the polypyridyl ligands to provide vacant site(s) for CO_2 binding and conversion. On the other hand, pyridine diimine complexes of Fe and Co have been shown to promote the electrochemical and photochemical CO_2 reduction,[28-29] but Ni analogs was rarely reported. In nature, Ni-containing carbon monoxide dehydrogenase cluster C (CODH) can carry out selective CO_2 reduction to CO, which is facilitated by precisely positioned redox-active ferredoxin unit.[30-31] Therefore, Ni-based complexes with a redox-active ligand and a coordination labile site is very promising candidate as a catalyst for CO_2 reduction reaction.

With this in mind, I designed a groups of redox-active pentadentate N5 ligands, **L1** and **L2**, as illustrated in Figure 1. By using these ligands, I have successfully obtained two Ni complexes containing redox-active α-iminopyridine moieties and a coordination labile site (**Ni1** and **Ni2**, Figure 2). In this study, I report the syntheses, characterization, redox behavior, and photochemical CO_2 reduction activity of these Ni complexes.
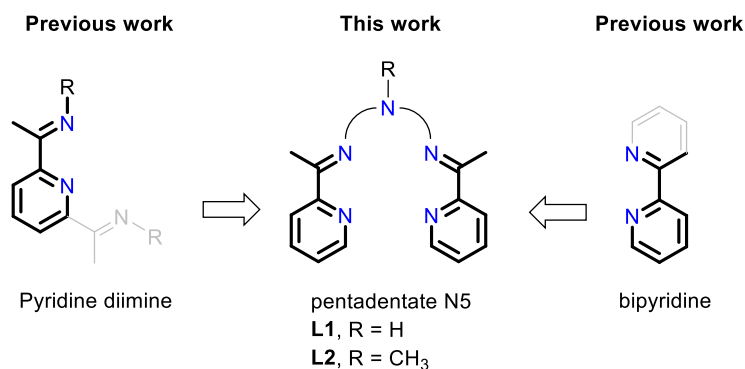
Figure 1: Design of ligands studied in this study.
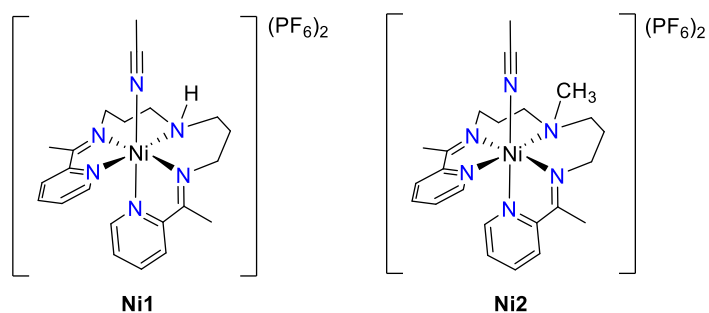
Figure 2: Chemical structures of **Ni1** and **Ni2**.

Results and discussions

Syntheses and characterization

Two novel Ni complexes, **Ni1** and **Ni2**, were prepared by one-pot templated synthesis as shown in Scheme 1. The condensation of 2-acetylpyridine with stoichiometric amount of diamine precursors in MeOH, followed by the addition of Ni salts and anion exchange with $NaPF_6$, afforded **Ni1** and **Ni2** in high yield. They were characterized by electrospray ionization mass spectrometry (ESI-MS) (Figure 3), elemental analysis, UV-Vis absorption spectroscopy (Figure 4 & 5), and X-ray crystallography (Figure 6 & 7).

The solid states structures of **Ni1** and **Ni2** determined by single-crystal X-ray crystallography are shown in Figure 6 & 7. Crystals were obtained by slow vapor diffusion of diethyl ether into acetonitrile (MeCN) solution of Ni complexes. **Ni1** and **Ni2** are crystallized in monoclinic $P2_1$ space group. The Ni atom is coordinated by five nitrogen atoms of the pentadentate N5 ligand and a nitrogen atom from MeCN molecule, forming the high spin octahedral geometry. Crystal structures analysis revealed that the MeCN ligands are bent with Ni–N–C angles of 203º for **Ni1** and 193º for **Ni2**, probably due to the steric effect of the propyl linker of the pentadentate ligand. In addition, The Ni–N(MeCN) bonds of **Ni1** (2.151 Å) and **Ni2** (2.133 Å) are relatively longer compared to other Ni^{II} complexes in literature (Ni–N(MeCN) = 2.025–2.095 Å).[32-33] These results indicates that the MeCN ligand should be more labile towards substitution than previously reported complexes.

The imine bond (C=N) distances of these Ni complexes are in the range of 1.262–1.287 Å, which is in good agreement with the bond distances found in other similar metal complexes bearing neutral α-iminopyridine ligands.[34-35]. Thus, **Ni1** and **Ni2** may be best described as neutral-ligand complexes of Ni^{II}. These neutral α-iminopyridine moieties are expected to provide an additional site for electron storage during the reduction reaction. Furthermore, **Ni1** has been designed to contain a pendant amine group (NH) near the CO_2 binding site. Previous studies showed that the introduction of pendant NH group can help in stabilizing CO_2 adduct through H-bonding and enhance the catalytic activity.[36-39] On the other hand, a methyl substituent has been incorporated on the amine group for **Ni2**. The bulky methyl substituent on the amine group did not cause obvious structural change between **Ni2** and **Ni1**, which make their comparison possible.
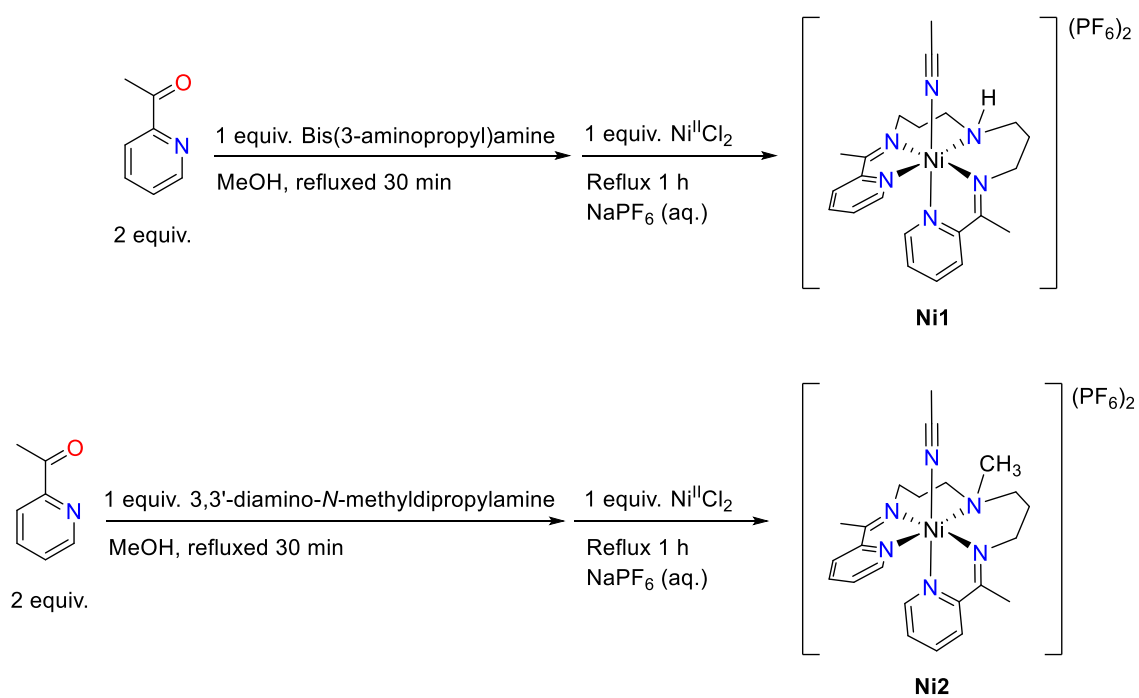
Scheme 1: Synthetic scheme for **Ni1** and **Ni2**.
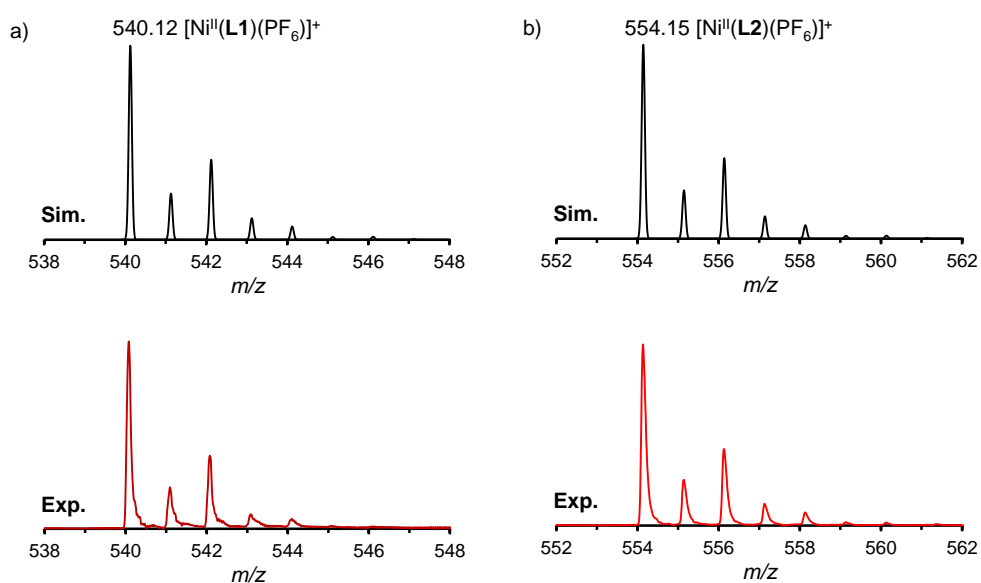
Figure 3: ESI-MS spectra of **Ni1** (a) and **Ni2** (b) in MeCN solution.
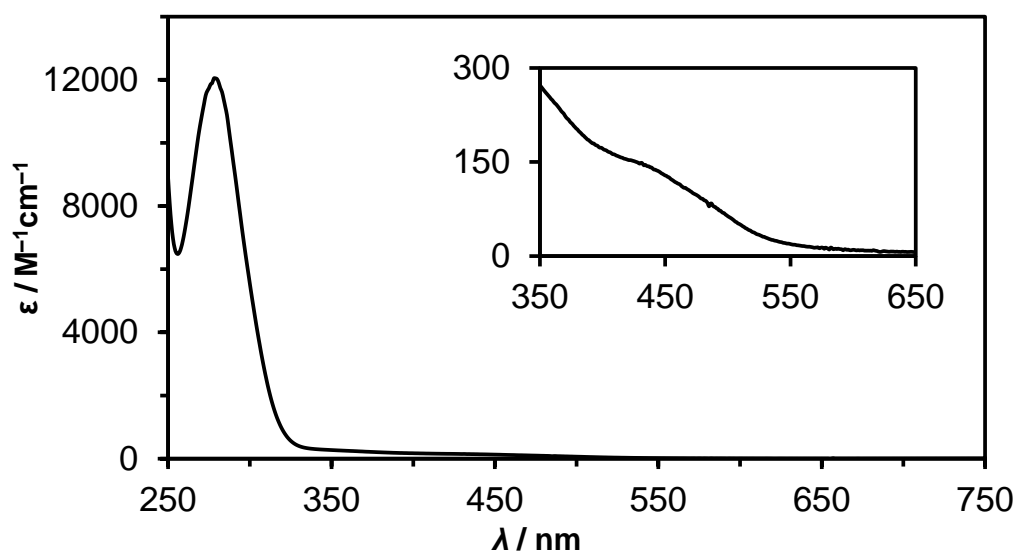
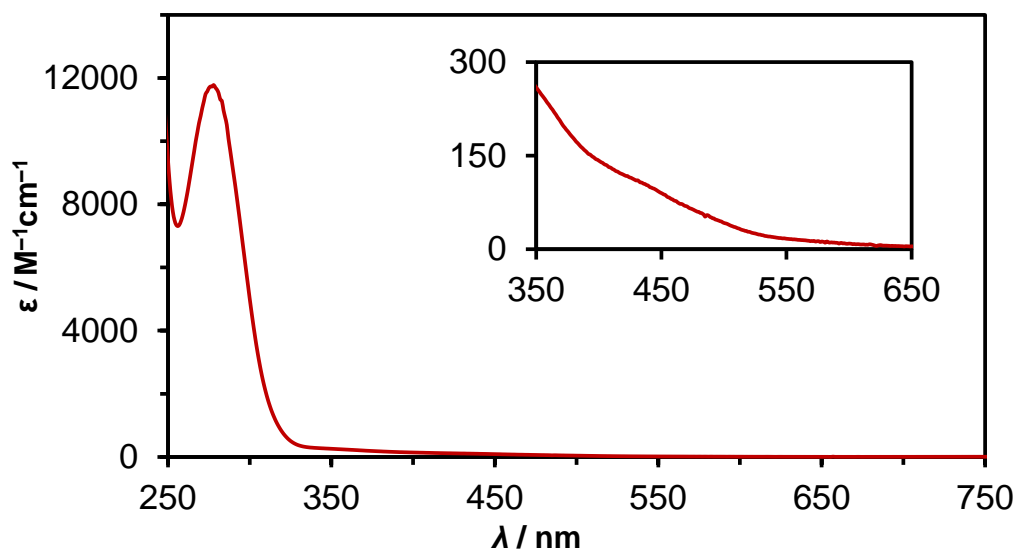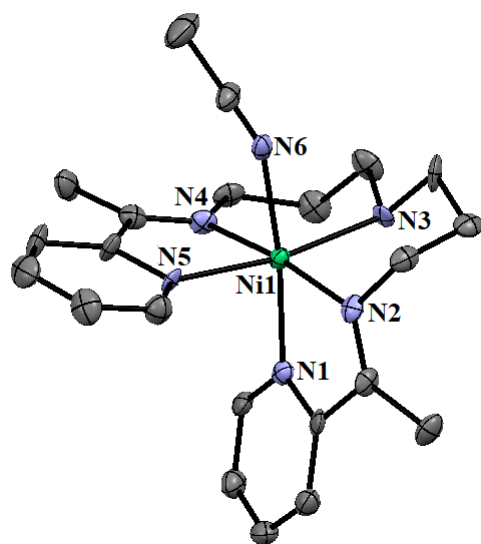Figure 4: UV-Vis absorption spectrum of **Ni1** in MeCN solution.

Figure 5: UV-Vis absorption spectrum of **Ni2** in MeCN solution.

	[Ni^{II}(**L1**)(MeCN)](PF$_6$)$_2$ (**Ni1**)
Formula	C$_{22}$H$_{30}$N$_6$P$_2$F$_{12}$Ni
Formula weight	727.17
Space group	P2$_1$
a (Å)	8.1744(5)
b (Å)	10.1023(5)
c (Å)	17.4254(9)
α (°)	90
β (°)	93.045 (7)
γ (°)	90
V (Å^3)	1436.96 (14)
Z	2
R_1	0.0988
GOF	1.072

Figure 6: An ORTEP drawing (50 % probability thermal ellipsoids) and selected crystallographic parameters of **Ni1**. Hydrogen and counter anions are omitted for clarity.
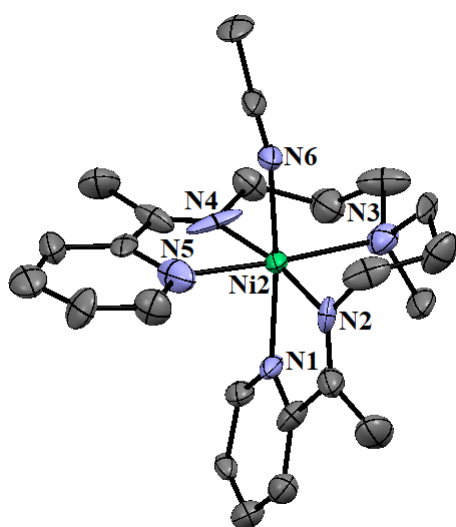
	[Ni^{II}(**L2**)(MeCN)](PF$_6$)$_2$ (**Ni2**)
Formula	C$_{23}$H$_{32}$N$_6$P$_2$F$_{12}$Ni
Formula weight	741.17
Space group	P2$_1$
a (Å)	8.524(5)
b (Å)	9.465(5)
c (Å)	18.423(5)
α (°)	90 (5)
β (°)	91.659 (5)
γ (°)	90 (5)
V (Å^3)	1485.7 (12)
Z	2
R_1	0.131
GOF	1.334

Figure 7: An ORTEP drawing (50 % probability thermal ellipsoids) and selected crystallographic parameters of **Ni2**. Hydrogen and counter anions are omitted for clarity.

Electrochemistry under Ar

Electrochemical experiments were performed to determine how the redox-active pentadentate N5 ligands affected the redox properties of **Ni1** and **Ni2**. In the cyclic voltammogram (CV) under Ar atmosphere, **Ni1** and **Ni2** displayed two reversible reduction waves in the negative potential region. The first half-wave potentials ($E_{1/2}$) for **Ni1** and **Ni2** were -1.40 V and -1.36 V, while the $E_{1/2}$ for second redox waves of **Ni1** and **Ni2** were -1.86 V and -1.79 V, respectively (Figure 8). Although the bulky methyl substituent on the amine group did not cause obvious structural change, it induced an unexpected positive shift in the reduction potential for **Ni2** as compared to **Ni1**.

To confirm whether these reduction peaks correspond to Ni or to a ligand-based reduction, the Zn analogue (**Zn1**) was synthesized (experimental section), and its electrochemical property was studied. Two reduction peaks were observed in the CV of **Zn1** at $E_{pc} = -1.67$ V and -1.91 V (Figure 9), which are attributed to the two discrete one-electron reduction of the ligand, **L1$^{0/-1}$** and **L1$^{-1/-2}$** (Figure 10).[24-25,34-35] Based on these results, the first reduction event of **Ni1** and **Ni2** can be assigned as the Ni$^{II/I}$ couples, while the second reduction event was due to ligand-based reduction, **L$^{0/-1}$**.
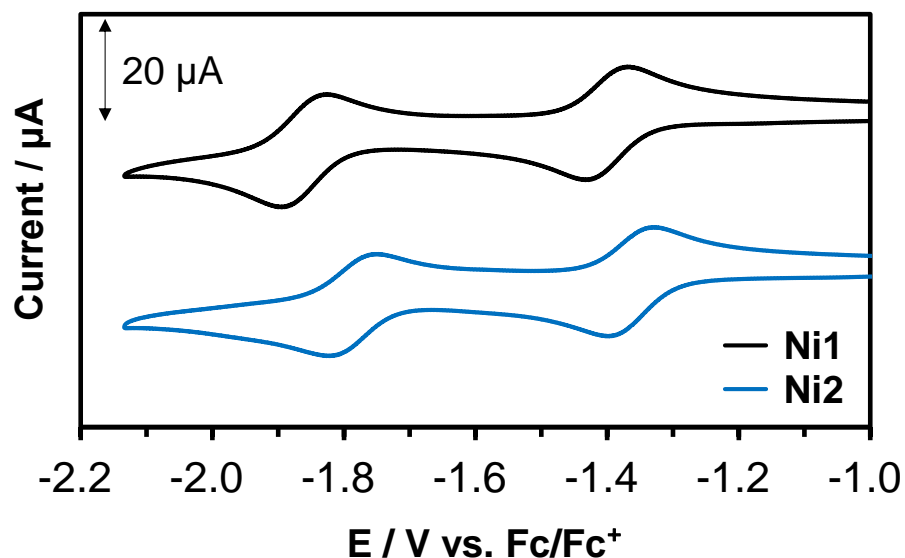
Figure 8: CVs of **Ni1** (0.5 mM) and **Ni2** (0.5 mM) in 0.1 M TBAP/MeCN under Ar. Working electrode, glassy carbon; counter electrode, Pt wire; reference electrode, Ag/Ag$^+$; scan rate, 0.1 V/s. Potential sweeps were started from the open circuit potential (-0.52 V and -0.49 V vs. Fc/Fc$^+$ for **Ni1** and **Ni2**, respectively) for all measurements.
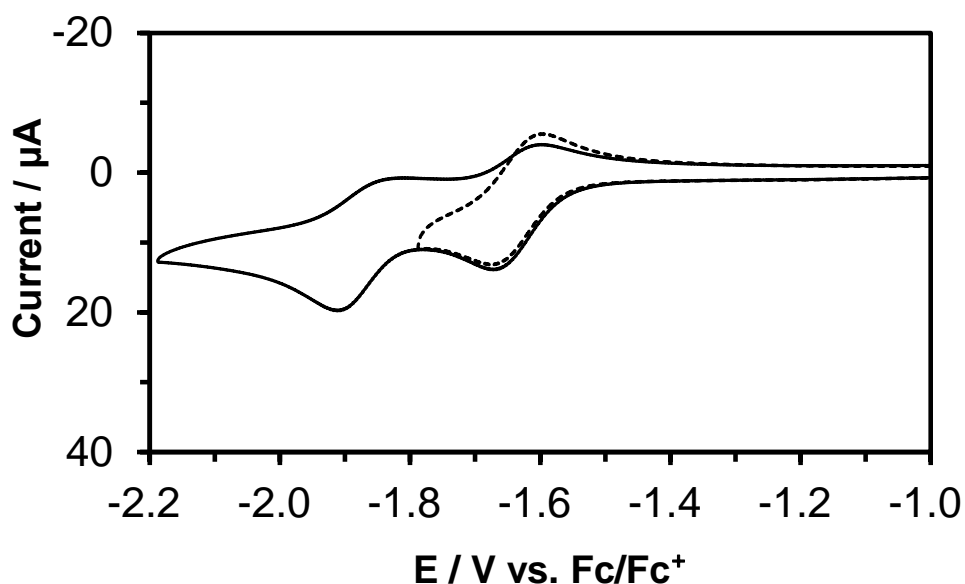
Figure 9: CVs of **Zn1** (0.5 mM) in 0.1 M TBAP/MeCN under Ar at different potential scan range. Working electrode, glassy carbon; counter electrode, Pt wire; reference electrode, Ag/Ag$^+$; scan rate, 0.1 V/s. Potential sweeps were started from the open circuit potential (-0.47 V vs. Fc/Fc$^+$).
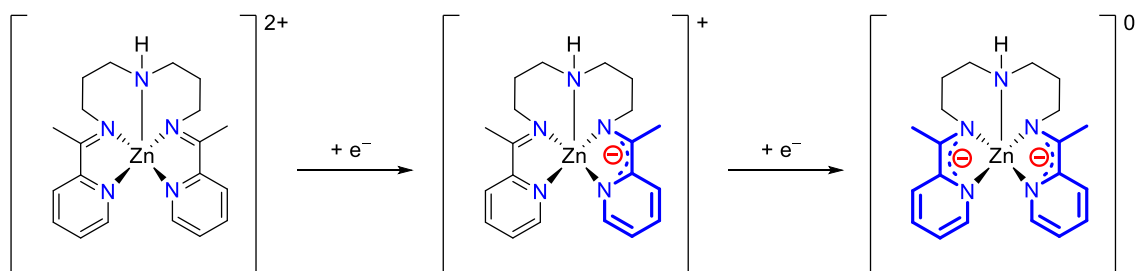
Figure 10: Proposed scheme for **Zn1** upon reduction. Since Zn^{II} is redox inert, the two discrete one-electron reduction were assigned to be ligand-centered.

Electrochemistry under CO_2

To investigate the reactivity of the complexes with CO_2, electrochemical measurements under CO_2 were conducted. Upon introduction of CO_2, second reduction waves of **Ni1** and **Ni2** became irreversible (Figure 11, red line), indicating that CO_2 interacts with the two-electron reduced state of **Ni1** and **Ni2**.[40] Addition of a weak Brønsted acid, trifluoroethanol (TFE) resulted in the increases in current and a shift of the second reduction waves to more positive potentials (Figure 11 & 12, blue line). The onset potential of the catalytic current for **Ni1** and **Ni2** were observed at approximately -1.65 V, respectively (Figure 11 & 12, blue line), which is more positive than the one-electron reduced species of the commonly used Ru photosensitizers (PS), $[Ru(bpy)_3]^{2+}$ and $[Ru(dmb)_3]^{2+}$ (-1.76 V and -1.87 V vs. Fc/Fc^+, respectively) (Figure 13). Thus, **Ni1** and **Ni2** can be used a catalyst for the photochemical CO_2 reduction assisted by $[Ru(bpy)_3]^{2+}$ and $[Ru(dmb)_3]^{2+}$ as PS.
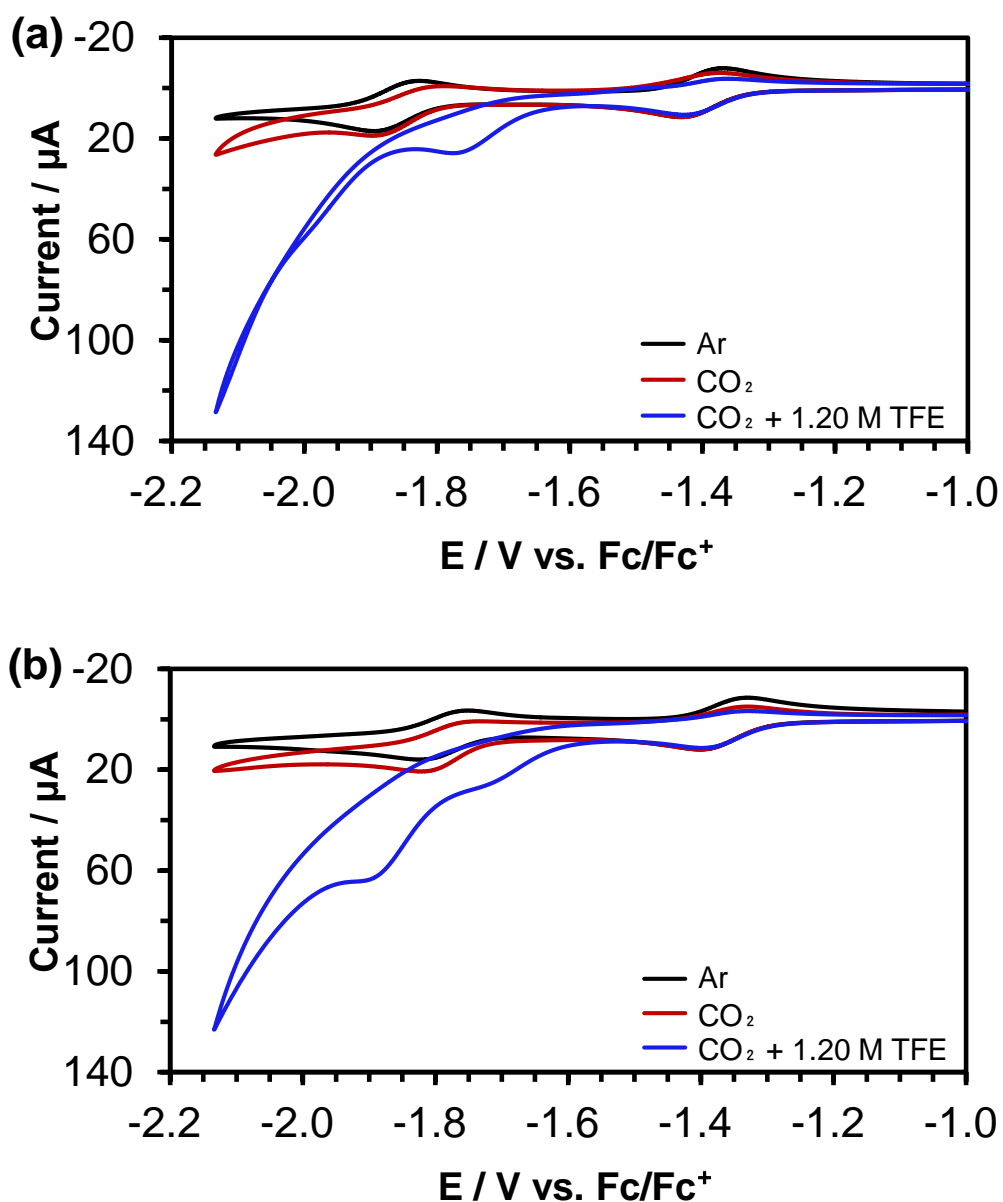
Figure 11: CVs of (a) **Ni1** (0.5 mM) and (b) **Ni2** (0.5 mM) in 0.1 M TBAP/MeCN under Ar (black line), CO_2 (0.28 M, red line), and CO_2 in the presence of 1.20 M TFE (blue line). Working electrode, glassy carbon; counter electrode, Pt wire; reference electrode, Ag/Ag$^+$; scan rate, 0.1 V/s.
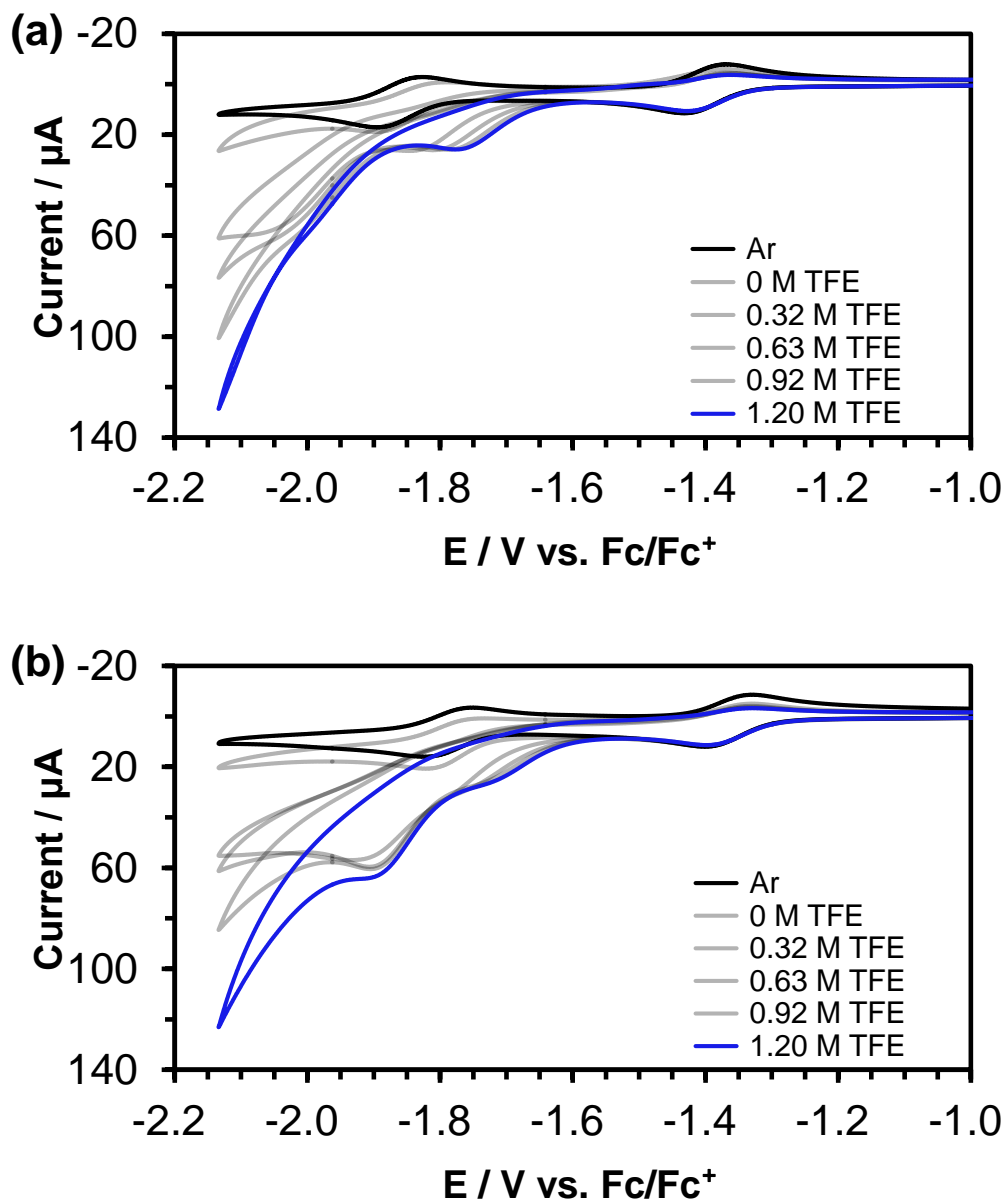
Figure 12: CVs of (a) **Ni1** (0.5 mM) and (b) **Ni2** (0.5 mM) in 0.1 M TBAP/MeCN at various concentrations of TFE under CO_2. Working electrode, glassy carbon; counter electrode, Pt wire; reference electrode, Ag/Ag^+; scan rate, 0.1 V/s.
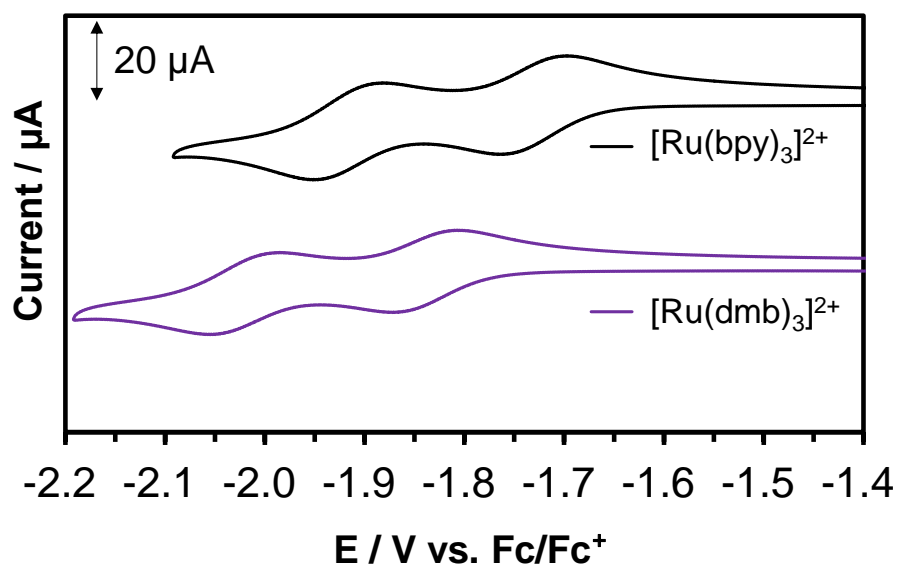
Figure 13: CVs of [Ru(bpy)₃]²⁺ (0.5 mM) (a) and [Ru(dmb)₃]²⁺ (0.5 mM) (b) in 0.1 M TBAP/MeCN under Ar. Working electrode, glassy carbon; counter electrode, Pt wire; reference electrode, Ag/Ag⁺; scan rate, 0.1 V/s.

Photochemical CO₂ reduction

Photochemical CO_2 reduction was initially conducted under visible-light irradiation (450 nm) in a CO_2-saturated triethanolamine (TEOA)/MeCN (15 % v/v) solution containing $[Ru(bpy)_3]^{2+}$ as PS, 1,3-dimethyl-2-phenyl-2,3-dihydro-1*H*-benzo[d]imidazole (BIH) as sacrificial electron donor (SD), and **Ni1** or **Ni2** as catalysts. Upon photo-irradiation, **Ni1** and **Ni2** could produce CO with the initial reaction rate of 565 µmolg^{-1}h^{-1} (TON = 1.4) and 1095 µmolg^{-1}h^{-1} (TON = 1.7) respectively (Table 1, Entry1–2). In the absence of catalysts, H_2 was the only detected product (Table 1, Entry 3). These results suggested that the photochemical CO_2 reduction to CO was catalyzed by Ni complexes. The H_2 evolution might be accounted to the decomposed PS. The use of PS with stronger reducing power ($[Ru(dmb)_3]^{2+}$) and proton source with higher acidity (TFE) did not enhance the turnover for CO production, and showed significant blank activity (Table 1, Entry 4–6). Further work is underway to improve the catalytic turnover.

During the photochemical reaction, photo-excited PS should be smoothly quenched by BIH, forming the one-electron reduced PS$^-$ species (Figure 14).[15,41] As evidence from the electrochemical studies (Figure 11-13), PS$^-$ has sufficient reducing power to doubly reduce the **Ni1** and **Ni2** to yield $[Ni1]^{2-}$ and $[Ni2]^{2-}$. Subsequently, $[Ni1]^{2-}$ and $[Ni2]^{2-}$ interact with CO_2 and proton source (TEOAH$^+$, Figure 14) to promote C–O bond cleavage and CO evolution (Figure 15). **Ni1** showed similar catalytic activity as **Ni2**, suggesting the effect of pendant NH for providing H-bonding was not significant under these conditions. More mechanistic study is necessary to shed light on the reaction mechanism of **Ni1** and **Ni2**.
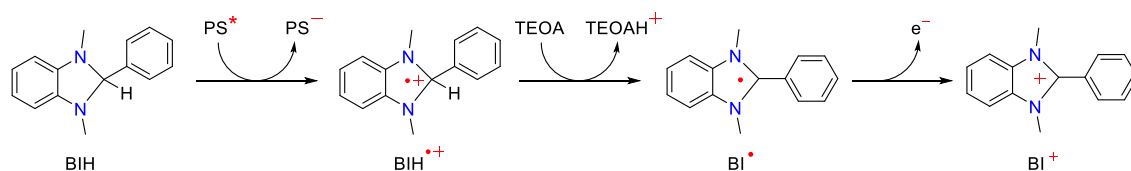
Figure 14: Reductive quenching of excited PS by BIH and role of protonated TEOA as a proton source during the photochemical reaction.[41]

Table 1: Summary of experimental conditions and results for the photocatalytic CO_2 reduction in CO_2-saturated solution containing 30 µM of catalyst (CAT), 150 µM of photosensitizer (PS), and 0.1 M sacrificial electron donor (SD) under irradiation ($\lambda = 450$ nm for $[Ru(bpy)_3]^{2+}$; $\lambda = 470$ nm for $[Ru(dmb)_3]^{2+}$) for 2 h.

No.	CAT	PS	Solvent	SD	TON		
					CO	HCOOH	H₂
1	Ni1	$[Ru(bpy)_3]^{2+}$	TEOA/MeCN (15 %, v/v)	BIH	1.4	0	0.7
2	Ni2	$[Ru(bpy)_3]^{2+}$	TEOA/MeCN (15 %, v/v)	BIH	1.7	0	1.3
3	-	$[Ru(bpy)_3]^{2+}$	TEOA/MeCN (15 %, v/v)	BIH	0	0	1.7
4	Ni1	$[Ru(dmb)_3]^{2+}$	TFE/DMA (15%, v/v)	BIH	55	0.6	0.1
5	Ni2	$[Ru(dmb)_3]^{2+}$	TFE/DMA (15%, v/v)	BIH	67	0.4	0.1
6	-	$[Ru(dmb)_3]^{2+}$	TFE/DMA (15%, v/v)	BIH	69	0.3	0.1
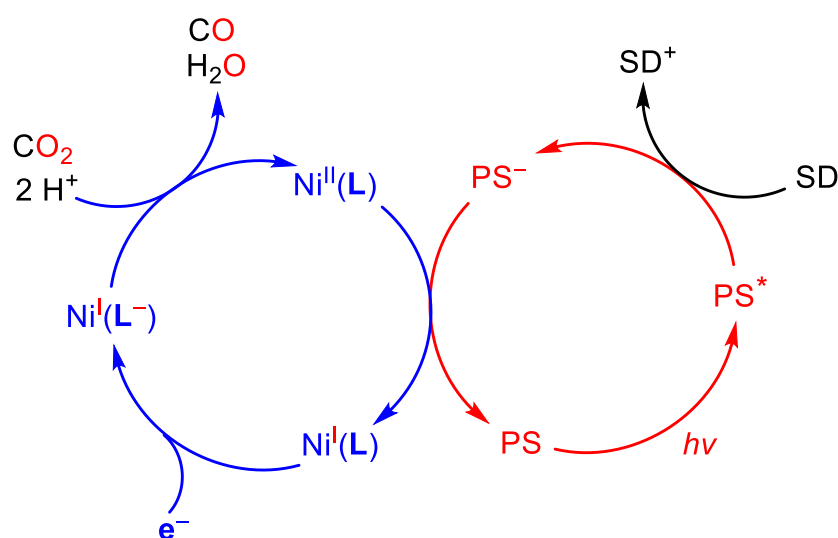
Figure 15: Proposed mechanism for the photochemical CO_2 reduction by **Ni1** and **Ni2** (PS = photosensitizer; SD = sacrificial electron donor).

Conclusion

As a summary, I have successfully synthesized two Ni complexes containing redox-active pentadentate N5 ligand. These Ni complexes can accumulate two reducing equivalents in relatively mild potential range (within -2.0 V vs. Fc/Fc^+), which is due to the metal and ligand-centered reduction. Under visible-light irradiation, these Ni complexes can promote CO_2 reduction to produce CO as major product. Further work is underway to improve the catalytic turnover and understand the reaction mechanism. Current work can provide inspiration for future development of Ni complexes for CO_2 reduction.

Experimental Details

General procedures

1,3-dimethyl-2-phenyl-2,3-dihydro-1*H*-benzo[d]imidazole (BIH) was synthesized according to literature procedures.[42] All the solvents were purchased from Wako Pure Chemical Industries, while the chemicals were purchased from Sigma-Aldrich Co. All the reagents were of highest quality available and were used as received. ^{1}H-NMR, ^{13}C-NMR were collected at room temperature on a JEOL JNM-ECS400 spectrometer. UV-vis absorption spectra were measured on a Shimadzu UV-2450SIM spectrophotometer at room temperature. Elemental analyses were performed on a J-Science Lab Micro Corder JM10 elemental analyzer. ESI-TOF-MS spectra were collected on a JEOL JMS-T100LC mass spectrometer.

Syntheses

[Ru(bpy)$_3$](PF$_6$)$_2$ was synthesized according to literature.[43] This complex was prepared by mixing RuCl$_3$ (530 mg, 2.6 mmol) with 2,2′-bipyridine (2.5 g, 16 mmol) in 100 ml of EtOH and refluxed for 12 h under Ar atmosphere. After cooling down, saturated NaPF$_6$ (aq) (1.68 g, 10 mmol) was added and the solid was collected by vacuum filtration. The solid was washed with water and acetone to remove excess unreacted Ru salts. Excess Et$_2$O was added into the acetone eluent to precipitate the desired Ru complex. The resulting bright red solid was further purified by recrystallized from MeCN/Et$_2$O solution (yield = 81 %). ESI-TOF MS (positive ion, MeCN): m/z 285.05 ([Ru(bpy)$_3$]$^{2+}$). ^{1}H NMR (CD$_3$CN): δ 8.47 (d, 6 H), 8.02 (td, 6 H), 7.70 (d, 6 H), 7.36 (m, 6 H). Anal. Found: C, 41.81; H, 2.90; N, 9.76. Calculated for C$_{30}$H$_{24}$N$_6$P$_2$F$_{12}$Ru: C, 41.92; H, 2.81, N, 9.78.

[Ru(dmb)$_3$](PF$_6$)$_2$ was synthesized followed similar method as [Ru(bpy)$_3$](PF$_6$)$_2$. The crude red solid was further purified by recrystallized from MeCN/Et$_2$O solution (yield = 79 %). ESI-TOF MS (positive ion, MeCN): m/z 327.1 ([Ru(dmb)$_3$]$^{2+}$), 799.1 ([Ru(dmb)$_3$(PF$_6$)]$^+$). ^{1}H NMR (CD$_3$CN): δ 8.29 (s, 6 H), 7.49 (d, 6 H), 7.18 (dd, 6 H), 2.49 (s, 18 H). Anal. Found: C, 44.89; H, 4.01; N, 8.86. Calculated for C$_{36}$H$_{26}$N$_6$P$_2$F$_{12}$Ru: C, 45.82; H, 3.85; N, 8.91.

[Ni(**L1**)(MeCN)](PF$_6$)$_2$ (**Ni1**) was synthesized by mixing 2-acetylpyridine (0.45 ml, 4 mmol) and bis(3-aminopropyl)amine (0.28 ml, 2 mmol) in 20 ml dehydrated MeOH and refluxed for 30 mins. Then, Ni^{II}Cl$_2$ (0.47 g, 2 mmol) was added into the reaction mixture and further refluxed for 1 h. After cooling down, the solution was evaporated into dryness, and washed with acetone and Et$_2$O. The crude solid was dissolved in tiny amount of MeCN and saturated NaPF$_6$ (aq) (1.68 g, 10 mmol). The solution was evaporated into dryness, and the solid was washed with water. Yellow crystal was obtained by recrystallization from MeCN/Et$_2$O (yield = 75 %). ESI-TOF MS (positive ion, MeCN): m/z 540.12 ([Ni(**L1**)(PF$_6$)]$^+$). Anal. Found: C, 35.05; H, 4.31; N, 10.70. Calculated for C$_{22}$H$_{30}$N$_6$P$_2$F$_{12}$Ni•1.5H$_2$O: C, 35.04; H, 4.41; N, 11.14.

[Ni(**L2**)(MeCN)](PF$_6$)$_2$ (**Ni2**) was synthesized followed similar method as **Ni1**. Yellow-orange crystal was obtained by recrystallization from MeCN/Et$_2$O (yield = 83 %). ESI-TOF MS (positive ion, MeCN): m/z 554.15 ([Ni(**L2**)(PF$_6$)]$^+$). Anal. Found: C, 35.89; H, 4.41; N, 10.70. Calculated for C$_{23}$H$_{32}$N$_6$P$_2$F$_{12}$Ni•2H$_2$O: C, 35.54; H, 4.67; N, 10.81.

[Zn(**L1**)](PF$_6$)$_2$ (**Zn1**) was synthesized followed similar method as **Ni1**. Colorless crystal was obtained by recrystallization from MeCN/Et$_2$O (yield = 80 %). ESI-TOF MS (positive ion, MeCN): m/z 546.12 ([Zn(**L1**)(PF$_6$)]$^+$). Anal. Found: C, 34.50; H, 3.86; N, 10.09. Calculated for C$_{20}$H$_{27}$N$_5$P$_2$F$_{12}$Zn: C, 34.67; H, 3.93; N, 10.11.

Electrochemistry

Electrochemical experiments were performed at room temperature on a BAS ALS Model 650DKMP electrochemical analyzer in acetonitrile ([cat.] = 0.5 mM; 0.1 M tetraethylammonium perchlorate (TEAP)). Cyclic voltammetry was performed by using a one-compartment cell with a three-electrode configuration, which consisted of a glassy carbon disk, platinum wire, and Ag/Ag$^+$ electrode (Ag/0.01 M AgNO$_3$) as the working, auxiliary, and reference electrodes, respectively. The glassy carbon disc working electrode was polished using alumina prior to each measurement.

Photocatalytic reaction

For typical run, a mixed solution of TEOA/MeCN (15 %, v/v) (2.0 ml) containing 30 µM Ni catalyst, 150 µM Ru photosensitizer, and 0.10 M BIH was purged with CO_2 for 20 minutes unless otherwise stated. The solution was then irradiated with a 450 nm (for $[Ru(bpy)_3]^{2+}$) or 470 nm (for $[Ru(dmb)_3]^{2+}$) LED lamp at 20 ℃ in a custom made aluminium box with cooling system. The amount of CO and H_2 produced at the headspace of the cell was quantified by a Shimadzu GC-8A with a TCD detector equipped with a packed column with Molecular Sieve 13X-S 60/80. Additionally, liquid product was quantified by using a Shimadzu LC-20AD with SPD-20A and RID-10A detectors equipped with a Shim-pack SCR102H column. Calibration curves were obtained by sampling known amounts of H_2, CO, and HCOOH.

Crystallography

The diffraction data of a crystal of **Ni1** and **Ni2** at 123 K were measured on a Rigaku R-AXIS RAPID imaging plate diffractometer equipped with confocal monochromated MoKα radiation, and the data were processed using RAPID AUTO (Rigaku). The structure was solved by the direct method using SIR-92[44] and refined by using SHELXL-2014/7.[45]

References:

1) A. Magnuson, M. Anderlund, O. Johansson, P. Lindblad, R. Lomoth, T. Polivka, S. Ott, K. Stensjö, S. Styring, V. Sundström, L. Hammarström, *Acc. Chem. Res.* 2009, **42**, 1899-1909.

2) M. Mikkelsen, M. Jørgensen, F. C. Krebs, *Energy Environ. Sci.* 2010, **3**, 43-81.

3) T. J. Meyer, *Acc. Chem. Res.* 1989, **22**, 163-170.

4) N. S. Lewis, D. G. Nocera, *Proc. Natl. Acad. Sci. U. S. A.* 2006, **103**, 15729-15735.

5) A. Goeppert, M. Czaun, J.-P. Jones, G. K. Surya Prakash, G. A. Olah, *Chem. Soc. Rev.* 2014, **43**, 7995-8048.

6) J. Hawecker, J. M. Lehn, R. J. Ziessel, *Chem. Soc. Chem. Commun.* 1983, 536-538.

7) H. Ishida, T. Terada, K. Tanaka, T. Tanaka, *Inorg, Chem.* 1990, **29**, 905-911.

8) T. Nakajima, Y. Tamaki, K. Ueno, E. Kato, T. Nishikawa, K. Ohkubo, Y. Yamazaki, T. Morimoto, O. Ishitani, *J. Am. Chem. Soc.* 2016, **138**, 13818-13821.

9) Y. Kuramochi, J. Itabashi, K. Fukaya, A. Enomoto, M. Yoshida, H. Ishida, *Chem. Sci.* 2015, **6**, 3063-3074.

10) M. B. Chambers, X. Wang, N. Elgrishi, C. H. Hendon, A. Walsh, J. Bonnefoy, J. Canivet, E. A. Quadrelli, D. Farrusseng, C. Mellot-Draznieks, M. Fontecave, *ChemSusChem.* 2015, **8**, 603-608.

11) S. Sato, T. Morikawa, T. Kajino, O. Ishitani, *Angew. Chem. Int. Ed.* 2013, **52**, 988-992.

12) Y. Yamazaki, H. Takeda, O. Ishitani, *J. Photochem. Photobiol. C* 2015, **25**, 106-137.

13) N. Elgrishi, M. B. Chambers, X. Wang, M. Fontecave, *Chem. Soc. Rev.* 2017, **46**, 761-796.

14) J. Bonin, A. Maurin, M. Robert, *Coord. Chem. Rev.* 2017, **334**, 184-198.

15) H. Takeda, C. Cometto, O. Ishitani, M. Robert, *ACS Catal.* 2017, **7**, 70-88.

16) B. J. Fisher, R. Eisenberg, *J. Am. Chem. Soc.* 1980, **102**, 7361-7363.

17) J. L. Grant, K. Goswami, L. O. Spreer, J. W. Otvos, M. Calvin, *J. Chem. Soc. Dalton Trans.* 1987, 2105-2109.

18) H. Rao, L. C. Schmidt, J. Bonin, M. Robert, *Nature*, 2017, **548**, 74-77.

19) Z. Guo, S. Cheng, C. Cometto, E. Anxolabéhère-Mallart, S. Ng, C. Ko, G. Liu, L. Chen, M. Robert, T. Lau, *J. Am. Chem. Soc.* 2016, **138**, 9413-9416.

20) Z. Guo, F. Yu, Y. Yang, C. Leung, S. Ng, C. Ko, C. Cometto, T. Lau, M. Robert, *ChemSusChem*, 2017, **10**, 4009-4013.

21) P. L. Cheung, C. W. Machan, A. Y. S. Malkhasian, J. Agarwal, C. P. Kubiak, *Inorg. Chem.* 2016, **55**, 3192-3198.

22) V. S. Thoi, N. Kornienko, C. G. Margarit, P. Yang, C. J. Chang, *J. Am. Chem. Soc.* 2013, **135**, 14413-14424.

23) D. Hong, Y. Tsukakoshi, H. Kotani, T. Ishizuka, T. Kojima, *J. Am. Chem. Soc.* 2017, **139**, 6538-6541.

24) C. C. Lu, E. Bill, T. Weyhermüller, E. Bothe, K. Wieghardt, *J. Am. Chem. Soc.* 2008, **130**, 3181-3197.

25) P. J. Chirik, K. Wieghardt, *Science* 2010, **327**, 794-795.

26) S. Daniele, P. Ugo, G. Bontempelli and M. Fiorani, *J. Electroanal. Chem.* 1987, **219**, 259–271.

27) N. Elgrishi, M. B. Chambers, V. Artero, M. Fontecave, *Phys. Chem. Chem. Phys.* 2014, **16**, 13635-13644.

28) L. Chen, Z. Guo, X. Wei, C. Gallenkamp, J. Bonin, E. Anxolabéhère-Mallart, K. Lau, T. Lau, M. Robert, *J. Am. Chem. Soc.* 2015, **137**, 10918-10921.

29) D. C. Lacy, C. C. L. McCrory, J. C. Peters, *Inorg. Chem.* 2014, **53**, 4980-4988.

30) H. Dobbek, V. Svetlitchnyl, L. Gremer, R. Huber, O. Meyer, *Science* 2001, **293**, 1281-1285.

31) J. Jeoung, H. Dobbek, *Science*, 2007, **318**, 1461-1464.

32) P. H. A. Kankanamalage, S. Mazumder, V. Tiwari, K. K. Kpogo, H. B. Schlegel, C. N. Verani, *Chem. Commun.* 2016, **52**, 13357-13360.

33) E. C. Constable, S. M. Elder, J. Healy, D. A. Tocher, *J. Chem. Soc. Dalton Trans.* 1990, 1669-1674.

34) C. C. Lu, T. Weyhermüller, E. Bill, K. Wieghardt, *Inorg. Chem.* 2009, **48**, 6055-6064.

35) S. C. Bart, K. Chlopek, E. Bill, M. W. Bouwkamp, E. Lobkovsky, F. Neese, K. Wieghardt, P. J. Chirik, *J. Am. Chem. Soc.* 2006, **128**, 13901-13912.

36) M. Beley, J. P. Collin, R. Ruppert, J. P. Sauvage, *J. Am. Chem. Soc.* 1986, **108**, 7461-7467.

37) E. Fujita, D. J. Szalda, C. Creutz, N. Sutin, *J. Am. Chem. Soc.* 1988, **110**, 4870-4871.

38) D. C. Lacy, C. C. L. McCrory, J. C. Peter, *Inorg. Chem.* 2014, **53**, 4980-4988.

39) A. Chapovetsky, T. H. Do, R. Haiges, M. K. Takase, S. C. Marinescu, *J. Am. Chem. Soc.* 2016, **138**, 5765-5768.

40) J. Schneider, H. Jia, J. T. Muckerman, E. Fujita, *Chem. Soc. Rev.* 2012, **41**, 2036-2051.

41) Y. Yamazaki, H. Takeda, O. Ishitani, *J. Photochem. Photobiol. C* 2015, **25**, 106-137.

42) X. Zhu, M. Zhang, A. Yu, C. Wang, J. Cheng, *J. Am. Chem. Soc*. 2008, **130**, 2501-2516.

43) M. A. Ischay, Z. Lu, T. P. Yoon, *J. Am. Chem. Soc*. 2010, **132**, 8572-8574.

44) A. Altomare, G. Cascarano, C. Glacovazzo, A. Guagliardi, *J. Appl. Crystallogr*. 1993, **26**, 343-350.

45) G. M. Sheldrick, SHELXL 2014/7, University of Göttingen, Göttingen (Germany), 2014.

Concluding remarks

The research reported in this thesis has investigated the activity of several metal-complex based catalysts for electro- and photo-chemical CO_2 reduction. Chapter 1 demonstrates a new strategy to reduce the overpotential of a Ru-based electrocatalyst by the introduction of a phosphine ligand at the *trans* position of a labile ligand. Due to the *trans*-influence of the phosphine ligand, this Ru complex can activate CO_2 at the one-electron reduced state and promotes electrochemical CO_2 reduction at a low-overpotential. Current approach might be applicable on other metal-based catalysts. The discovery of such catalyst is also particularly important from the viewpoint of photocatalysis.

Chapter 2 shows the first example of non-sensitized Ru-based photocatalyst for CO_2 reduction. Such function-integrated photocatalyst can harvest visible-light and catalyze CO_2 conversion within one molecular unit by taking advantage of the Ru polypyridyl scaffold, *trans*-influence of the phosphine ligand, and the nature of Ru center. This Ru photocatalyst can convert CO_2 to CO with a highest TON and TOF among the reported non-sensitized photocatalysts, and can also exhibit tunable product selectivity (CO / HCOOH). Current strategy will allow the design of an efficient and simplified artificial photosynthetic device.

Chapter 3 demonstrates the potential of Ni complexes for photochemical CO_2 reduction. In this study, pentadentate redox-active ligand(s) are used to facilitate the Ni complexes to promote multi-electron CO_2 reduction, while Ni center functions as the active site for CO_2 conversion. The development of earth-abundant and low cost metal-based catalysts are particularly attractive for industrial use.

Collectively, these results showed that metal-complex based catalysts are very promising candidates for CO_2 reduction reaction. The cooperation between the metal ions and appropriate ligand can produce synergistic effects for CO_2 reduction. Variation of metal ions offers different reactivity towards CO_2 binding and conversion. At the same time, the structure of ligand can be modified to tune the electronic properties of metal centres as well as provide an additional electron storage site to mediate the reduction reaction. The research in this thesis may provide some useful guidelines for future catalyst optimization.

Acknowledgements

List of Publications

Chapter 1

"Low-overpotential CO_2 reduction by phosphine-substituted Ru(II) polypyridyl complex"

Sze Koon Lee, Mio Kondo, Go Nakamura, Masaya Okamura, Shigeyuki Masaoka

Chemical Communications, **2018**, 54, 6915-6918.

Chapter 2

"Function-integrated Ru catalyst for photochemical CO_2 reduction"

Sze Koon Lee, Mio Kondo, Masaya Okamura, Go Nakamura, Shigeyuki Masaoka

Submitted.

Chapter 3

"Ni complexes containing redox-active ligand for photocatalytic CO_2 reduction"

Sze Koon Lee, Mio Kondo, Unruangsri Junjuda, Masaya Okamura, Shigeyuki Masaoka

Manuscript in preparation.

Other publications

1) "Syntheses and CO_2 reduction activities of π-expanded/extended iron porphyrin complexes"
   Yuki Okabe, **Sze Koon Lee**, Mio Kondo, Shigeyuki Masaoka
   J. Biol. Inorg. Chem. **2017**, 22, 713-725.

2) "Topoisomerase I inhibition and DNA cleavage by zinc, copper, and nickel derivatives of 2-[2-bromoethyliminoethyl]-4-[ethoxymethyl]phenol complexes exhibiting anti-proliferation and anti-metastasis activity"
   Sze Koon Lee, Kong Wai Tan, Seik Weng Ng
   J. Inorg. Biochem. **2016**, 159, 14-21.

3) "Syntheses and properties of phosphine-substituted ruthenium(II) polypyridine complexes with nitrogen oxides"
   Go Nakamura, Mio Kondo, Meredith Crisalli, **Sze Koon Lee**, Akane Shibata, Peter C. Ford, Shigeyuki Masaoka
   Dalton Trans. **2015**, 44, 17189-17200.

4) "Zinc, copper and nickel derivatives of 2-[2-bromoethyliminomethyl]phenol as topoisomerase inhibitors exhibiting anti-proliferative and anti-metastatic properties"
   Sze Koon Lee, Kong Wai Tan, Seik Weng Ng
   RSC Adv. **2014**, 60280-60292.

5) "Copper complexes with phosphonium containing hydrazone ligand: Topoisomerase inhibition and cytotoxicity study"
   Shin Thung Chew, Kong Mun Lo, **Sze Koon Lee**, Mok Piew Heng, Wuen Yew Teoh, Kae Shin Sim, Kong Wai Tan
   Eur. J. Med. Chem. **2014**, 76, 397-407.

6) "Zinc(II) complex with a cationic Schiff base ligand: Synthesis, characterization, and biological studies"
   Sze Koon Lee, Kong Wai Tan, Seik Weng Ng, Kah Kooi Ooi, Kok Pian Ang, Md Akim Abdah
   Spectrochim. Acta A **2014**, 121, 101-108.